Monitoring Sensors with Nanoparticle-Dispersed Structural Color Polymer for Water-Prohibited Systems

September 2025

Satoshi Nishita

Thesis for the Degree of Ph.D. in Engineering

Monitoring Sensors with Nanoparticle-Dispersed Structural Color Polymer for Water-Prohibited Systems

September 2025

Graduate School of Science and Technology
Keio University

Satoshi Nishita

Thesis Abstract

Structural color materials reflect a specific wavelength of color due to a periodic change in refractive index. Among those materials, structural color polymers contain nanoparticles dispersed in the polymer. Those polymers enable conversion from deformation into color changes. Thus, the structural color polymers have been widely researched for applications, such as displacement, temperature, and chemical sensors. These sensors were mostly based on soft hydrogel due to holding water inside, realizing wide-range color changes. However, the availability of structural color polymers as sensors in water-prohibited environments, such as electric circuits and reactive chemicals with water, has been rarely considered.

Herein, two monitoring sensors using a non-hydrogel structural color polymer for water-prohibited environments are proposed. The availability of the non-hydrogel structural color polymer as a deformation-to-optical transducer near electric circuits or water-reactive lithium was shown.

Chapter 1 described the background, the purpose, and the concept of this dissertation.

Chapter 2 detailed the principles of structural color polymers. The mechanical theory and ideal/amorphous structures of the microsphere-dispersed structural color polymer were described.

Chapter 3 explained the fabrication methods and structure analysis of the fabricated structural color polymers. The analysis using the SEM (scanning electron microscope) images revealed that the fabricated polymer had an amorphous structure of silica nanoparticles.

Chapter 4 examined color detection with the in-line microliter liquid color monitoring sensor as the first suggestion. The polymer is non-hydrogel, achieving water protection for the electronic circuit. The wavelength of the reflective light on the polymer was changed by external compression. With this mechanism, the sensor achieved color detection between green and yellow. The sensor also detected the difference in pH by using a BTB (bromothymol blue) solution.

Chapter 5 focused on observation with the stress monitoring sensor between electrodes in a lithium battery as the second suggestion. A lithium-based electrolyte was permeated into the separator sensor, enabling mechanical stress monitoring while maintaining the battery's performance. The stress sensor revealed when and where microbubbles or dendrites occurred in the battery. The stress sensor also achieved long-term observation during the charging/discharging cyclic test 100 times.

Chapter 6 concluded this dissertation with a discussion of prospects for the sensor of the non-hydrogel structural color polymer.

Table of Contents

CHAPTER 1.
GENERAL INTRODUCTION

1.1 Objective of This Dissertation

The objective of this dissertation is to extend the functional concept of non-hydrogel structural color polymers as transducers between the light and mechanical deformation (optical and mechanical information) through the extension of sensing methodology.

Objects with structural colors have been widely reported to display colors without dyes. Photonic crystals with specific nanometer-sized structures, including structural color polymers, have been studied for the development of novel sensors. Among photonic crystals, structural color polymers are more flexible than others, due to the material properties. In particular, structural color hydrogels have been utilized for sensors to measure various parameters, such as mechanical forces, temperatures, and chemical reactions. However, those sensors lack stability in the air and near electric circuits. As a result, sensors made of the structural color hydrogels tend to be for single use or disposable, not for long-term monitoring. However, this dissertation focuses on non-hydrogel structural color polymers. The non-hydrogel polymers have a stable shape in the air because the polymers do not contain water. Moreover, the non-hydrogel polymers are applicable near the electric current. By forming the non-hydrogel structural color polymer into a thin sheet, this dissertation shows the advantages as a transducer between optical and mechanical information, such as

continuous deformation-to-wavelength conversion and spatial stress sensing with distribution of structural color.

In this dissertation, two monitoring sensors with a non-hydrogel structural color polymer were presented and evaluated to confirm the extension of the methodology for "optical sensing" and "deformation sensing". The first is related to optical sensing: an in-line spectrometer with an optical filter made of a non-hydrogel structural color polymer. The optical filter was repeatedly compressed with external force to change the reflective wavelength of the filter. The light with tunable reflective wavelength was irradiated to liquid samples in a glass capillary, resulting in the accurate determination of sample color using an electric measurement system. The optical filter was deformed continuously rather than discretely, reducing the loss of wavelength information in the liquid sample. The second is related to deformation sensing: a stress sensor sheet made of a non-hydrogel structural color polymer for sensing of lithium battery separators. The sheet displayed the local stress caused by bubbles and crystals in the battery separator by changes in structural color distribution. The sensor sheet did not cause an electric short and maintained the conductivity, suggesting that the non-hydrogel structural color polymer had a stable stress-sensing capability for long-term battery operation.

1.2 Overview of Structural Color Materials

Structural color is defined as the visible light derived from nanostructures in materials [1–5]. The structural color is often shown in animals, first reported by Hooke in 1665 [6]. For example, the feathers of peacocks [6–8], *Morpho* butterflies [9], or chameleons [10] have structural colors. The structural colors are also seen in natural ores such as opals [11].

Artificial structural color was widely studied after the electron microscope was developed (Figure 1.1). The principles of multilayers and Fabry-Perot resonance were confirmed with many experiments, enabling the development of new devices with structural colors [12–16]. In 1987, three-dimensional (3D) photonic crystals (PCs) were theoretically

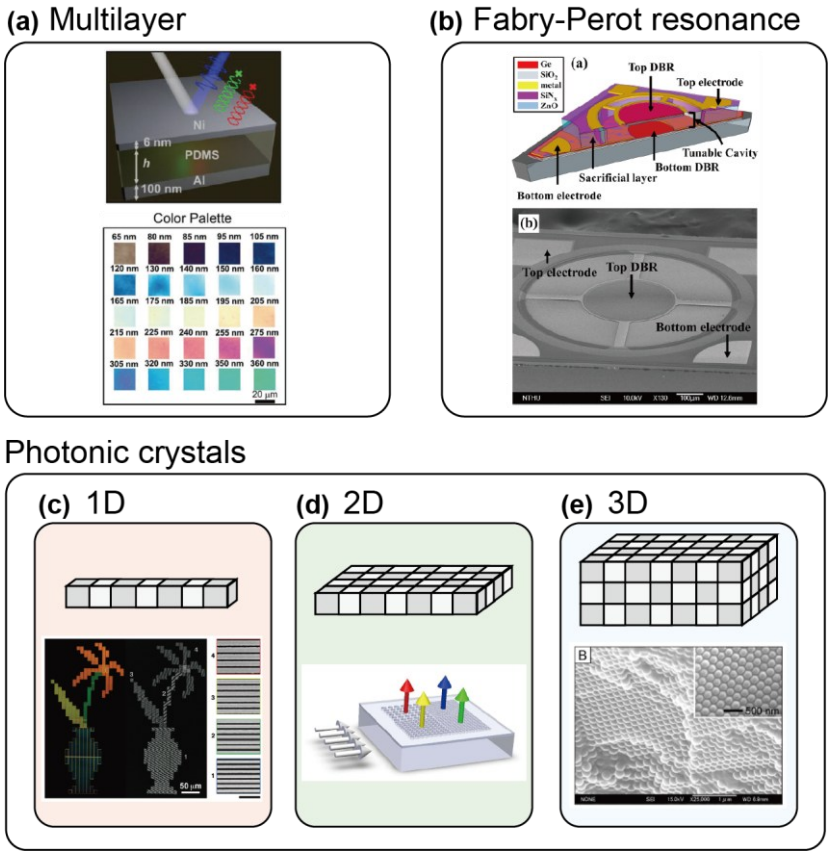

Figure 1.1 Variation of artificial structural color elements. (a) A multilayered optical filter with structural colors. [13] (b) A device using Fabry-Perot resonance. [16] (c) A 1D photonic crystal consisting of multiple lines. [19] (d) A 2D photonic crystal with multiple holes. [20] (e) A 3D photonic crystal with self-assembled nanoparticles. [26]

considered by Yablonovitch [17] at first. PCs have a periodic refractive index variance causing a photonic band gap (PBG). The periodic structure inhibits the transmission of light with wavelengths in the PBG through the PCs. When the PCs have the PBG in visible light wavelengths, the PCs show a structural color.

One-dimensional (1D) or Two-dimensional (2D) PCs were often made of metals or Si for easy fabrication. For example, Kaplan *et al*. fabricated 1D PC by nanoimprint lithography of Ag on a glass plate [18]. They patterned grating to the Ag layer with 280 nm and 420 nm periods, displaying blue and red reflected light. Cao et al. also showed the 1D

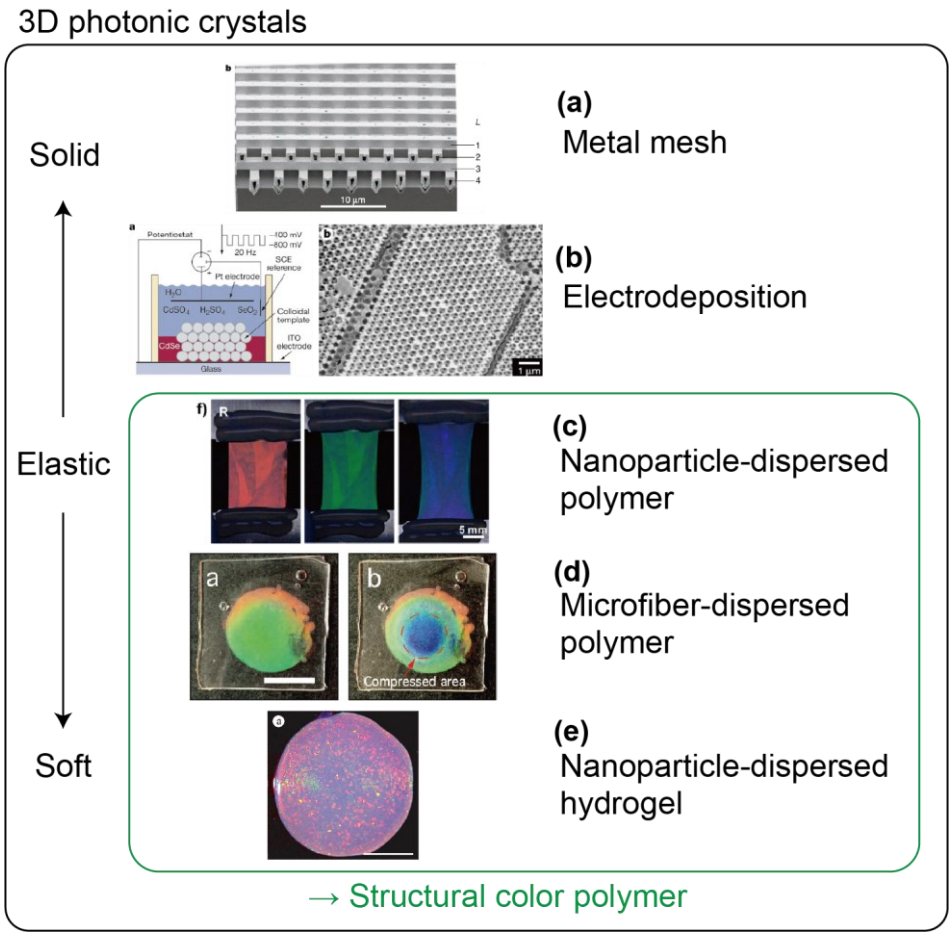

Figure 1.2 Definition of terms related to 3D photonic crystals in this dissertation. (a) Tungsten mesh. [21] (b) Electrodeposited particles. [22] (c) Nanoparticles were dispersed in an elastic polymer. [30] (d) Microfibers were dispersed in an elastic polymer. [35] (e) Nanoparticles were dispersed in a hydrogel. [28]

PC with silicon nanowires [19]. Pervez *et al.* showed a 2D photonic crystal made of PMMA (poly methyl methacrylate) with ordered holes [20]. The holes were fabricated with electron beam lithography (EBL). Those 1D and 2D PCs have optical applications, such as color filters, data storage, and encryption.

In contrast, 3D PCs were fabricated with various methods (Figure 1.2). Fleming *et al.* fabricated a 3D tungsten crystal by silicon etching and tungsten CVD (chemical vapor deposition) [21]. Braun *et al.* also suggested an electrodeposition method with cadmium-

selenium (CdSe) and cadmium-sulfide (CdS) [22]. To use these two methods for the fabrication of structural colors, metals are appropriate as raw materials, resulting in hard 3D PCs. Another fabrication method of 3D PCs was the self-assembly of nanoparticles in polymer [23–34]. At first, nanoparticles were dispersed in the medium and polymer precursors. After casting and drying, a polymer sheet with ordered nanoparticles was obtained. This 3D PC product is sometimes called colloidal photonic crystals. This method uses polymers, achieving soft and elastic 3D PCs with easier fabrication than the etching method. The other approach for 3D PCs is short fibers instead of nanoparticles. Kamita *et al.* showed an HPC (hydroxypropyl cellulose) PC in polydimethylsiloxane (PDMS) polymer [35]. Kim *et al.* fabricated a 3D PC with thermochromic liquid crystal [36]. Lee *et al.* fabricated a PC with a natural material, M13 bacteriophage [37]. As shown above, a variety of materials were used for 3D PC fabrication.

1.3 Structural Color Polymers – Colloidal Photonic Crystals with Large Strain

In this section, colloidal photonic crystals are focused on. The major materials of the nanoparticles are silica [23,28,30,31] or polystyrene (PS) [25–27]. To ensure PC structure, medium evaporation and electrostatic force were used. Other particles include chemically modified silica [24,29] and CaF_2 [32]. On the other hand, major polymer materials are PDMS[23,25–27,32] and hydrogels [28,29,33]. PDMS is elastic and has a low contact angle, resulting in elastic PCs with an easy fabrication method, precursor casting. PDMS is not polar and is inappropriate for the electrostatic force method. Hydrogels such as polyacrylamide are softer than PDMS because hydrogels contain a lot of water inside the polymer networks. Moreover, water is a polar medium, enabling the self-assembly of particles with electrostatic force. Hydrogels are also cured instantly by UV (ultraviolet) light with a photoinitiator. In 2017, Lee *et al.* reported PEGPEA (poly (ethylene glycol) phenyl ether acrylate) acrylic polymer as a material of colloidal photonic crystals [30,31]. This

material does not contain water, but the polymer precursor has a polarity. Therefore, the electrostatic force method is applicable. Other polymer materials include metallosupramolecular materials made of cerium trichloride ($CeCl_3$) and amino-terminated PDMS reported in 2018 [34].

The reported polymers are soft, causing color changes in the colloidal photonic crystals by deformation. A PDMS-based colloidal photonic crystal showed 32% strain (elongation)[26], a polyacrylamide-based showed 45% strain (compression)[28], a PEGPEA-based showed 69% strain (elongation)[30], and a metallosupramolecular-based showed 120% (elongation)[34]. From those situations, it seemed not appropriate to call the self-assembled 3D PC "colloidal photonic crystals," because the nanoparticles do not have strong bonding forces like normal crystals. Therefore, the term "structural color polymers" is used instead of "colloidal photonic crystals" in this dissertation. Note that "structural color polymers" also conceptually include microfiber-dispersed polymers introduced in Section 1.2. However, unless emphasized, the "structural color polymer" refers to microparticle-dispersed polymers in this dissertation.

1.4 Sensors with Structural Color Polymers

The feature of structural color polymers, that deformation causes their color changes, is attractive for the deformation sensors (Figure 1.3). A simple example is pressure/force sensors. A thin sheet of the structural color polymer was attachable to human skin, enabling the detection of joint bending [38]. The maximum strain was 68% with the sheet. A structural color polymer was also used to measure mechanical force induced by an electric field under 1-3 kV AC [24]. A magnetic nanoparticle-dispersed structural color polymer showed 0 T to 0.25 T magnetic field measurement with 750 nm to 520 nm wavelength change [39].

The second example is temperature sensors. The temperature was detected by thermo-responsive hydrogel-based structural color polymers, such as pNIPAAm (poly(*N*-isopropylacrylamide)) [40] or HEMA (hydroxyethyl methacrylate) [41]. The ranges of

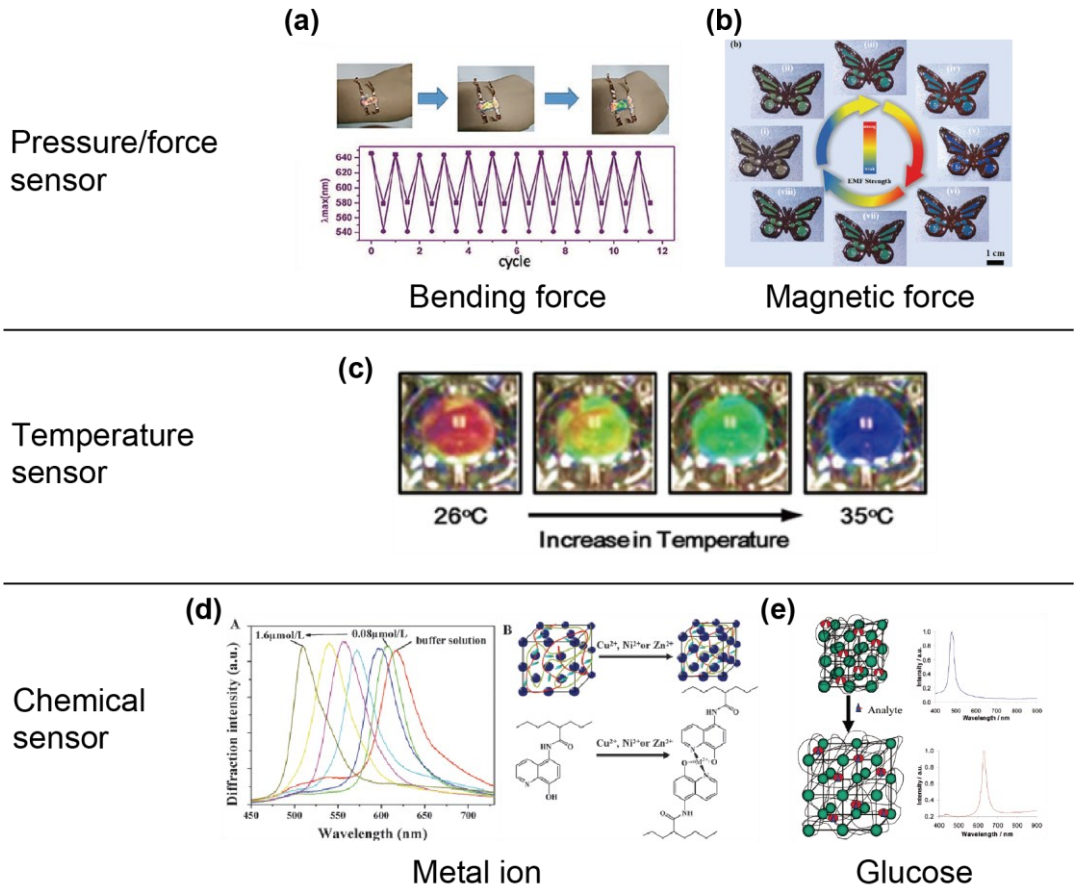

Figure 1.3 The sensors with structural color polymers. (a) Bending force sensor. [38] (b) Magnetic force sensor. [39] (c) Temperature sensor using pNIPAM hydrogel. [40] (d) Metal ion sensor. [43] (e) Glucose sensor. [45]

detectable temperature were 26-35°C with pNIPAAm and 25-50°C with HEMA, respectively. The temperature sensing range was relatively narrow because thermo-responsive hydrogels have an LCST (lower critical solution temperature), causing a structural change in the hydrogels [40,42].

The third is chemical component sensors. It was reported that pNIPAAm was also detectable for ethanol [40]. Moreover, metal ions [43], ammonia [44], glucose [45], protein [46], and many other materials [47] were detected with the structural color polymer sensors. These sensors were made of hydrogels, such as PVA (poly(vinyl alcohol)) [43], a co-polymer of poly-HEA (hydroxyethyl acrylate) + PEGDMA (poly(ethylene glycol) dimethacrylate)

[44], and poly-AAm (acrylamide)[45,46].

As shown, many sensors have been developed with structural color polymers. However, most of the polymers were hydrogels, containing water. Water causes some troublesome phenomena, such as evaporation and freezing. Water is also avoided in electric circuits due to insulation and rust prevention. Thus, sensors made of structural color polymer without water are required for stable measurements in electric devices. The deformation sensors were often made of non-hydrogel polymer, although temperature and chemical sensors with non-hydrogel polymer are rarely seen. The only example currently available is that Hu *et al.* showed an organic solvent sensor made of PS nanoparticles and P(MMA-BA) (poly(methylmethacrylate-butylacrylate)) polymer [48]. Swelling of the polymer enabled the detection of ethanol, methanol, cyclohexane, and *N,N*-dimethylformamide. Therefore, more applications with structural color polymers without water should be suggested.

1.5 This Work: Monitoring Sensors Based on Structural Color Polymers

Here, this dissertation provides the extended sensing methodology of the structural color polymer without water as a transducer between the light and the deformation (Figure 1.4). Such transducers also include multilayers or Fabry-Perot resonators. Unlike the two components, the structural color polymer has small elasticity, advantageous in small deformation sensing. Both the hydrogel and non-hydrogel structural color polymer are applicable to two major sensing targets: “optical sensing” and “deformation sensing” as the transducer between the light and deformation. The applications of the hydrogel and the non-hydrogel polymer are not the same because the hydrogel contains water. The hydrogel is softer than the non-hydrogel polymer, while the non-hydrogel polymer is stable against evaporation. Thus, the non-hydrogel polymer is available as a thin sheet due to the ease of fabrication. Moreover, the non-hydrogel polymer is also stable under electric currents. Therefore, this dissertation focuses on the methodology of the non-hydrogel structural color polymer to be utilized in the presence of an electric current.

The optical sensing with the hydrogel-based structural color polymers has been avoided due to the fragility and instability. In addition, precise optical resolution has typically been pursued with multilayers or Fabry-Perot resonators. On the other hand, this dissertation focuses on other advantages of the non-hydrogel structural color polymers, such as the thinness, flexibility, and ease of fabrication. Accordingly, this dissertation pioneers a novel application method with the non-hydrogel structural color polymers as optical components based on the above approach.

The deformation sensing with the structural color polymers has mainly been performed by converting external forces or temperature changes around the sensors into optical information via uniform deformation of the polymers. In contrast, this dissertation focuses on the utilization of the local deformation in the sensor as optical information derived from the structural color of the sensor. From this perspective, this dissertation proposes a method to obtain the spatial distribution of internal stress associated with chemical reactions, based on the optical distribution of the structural color polymer.

As described above, this study illuminates two unexplored functional concepts of non-hydrogel structural color polymers and proposes the following specific engineering applications: (1) an optical filter in an in-line spectrometer for “optical sensing” and (2) a stress sensor in a battery for “deformation sensing”. The aim is to conceptually expand the range of applications of structural color polymers. The materials of the non-hydrogel structural color polymer were silica nanoparticles and PEGPEA in both applications. The specifications of the fabricated sensors made of the silica-PEGPEA polymer were evaluated to clarify the functional concepts of the structural color polymers.

This dissertation demonstrates the two approaches – “optical sensing” and “deformation sensing” – to broaden the concept of the non-hydrogel structural color polymer methodology. The summary of sensors and sensing principles is as follows: (1) An in-line microliter liquid spectrum monitoring sensor. The non-hydrogel structural color polymer provided continuous deformation-to-wavelength conversion by linear compression of the polymer to change reflective wavelength instead of prisms or gratings in spectrometers. (2) A mechanical stress monitoring sensor between the electrodes of the lithium battery. The non-

hydrogel structural color polymer provided spatial stress sensing in the lithium battery separator by structural color visualization of stress by microbubbles or dendrites. More detailed information is presented in the next sections. Note that, in the following sections, the non-hydrogel structural color polymer is simply referred to as “the structural color polymer” in the narrow sense, unless otherwise specified.

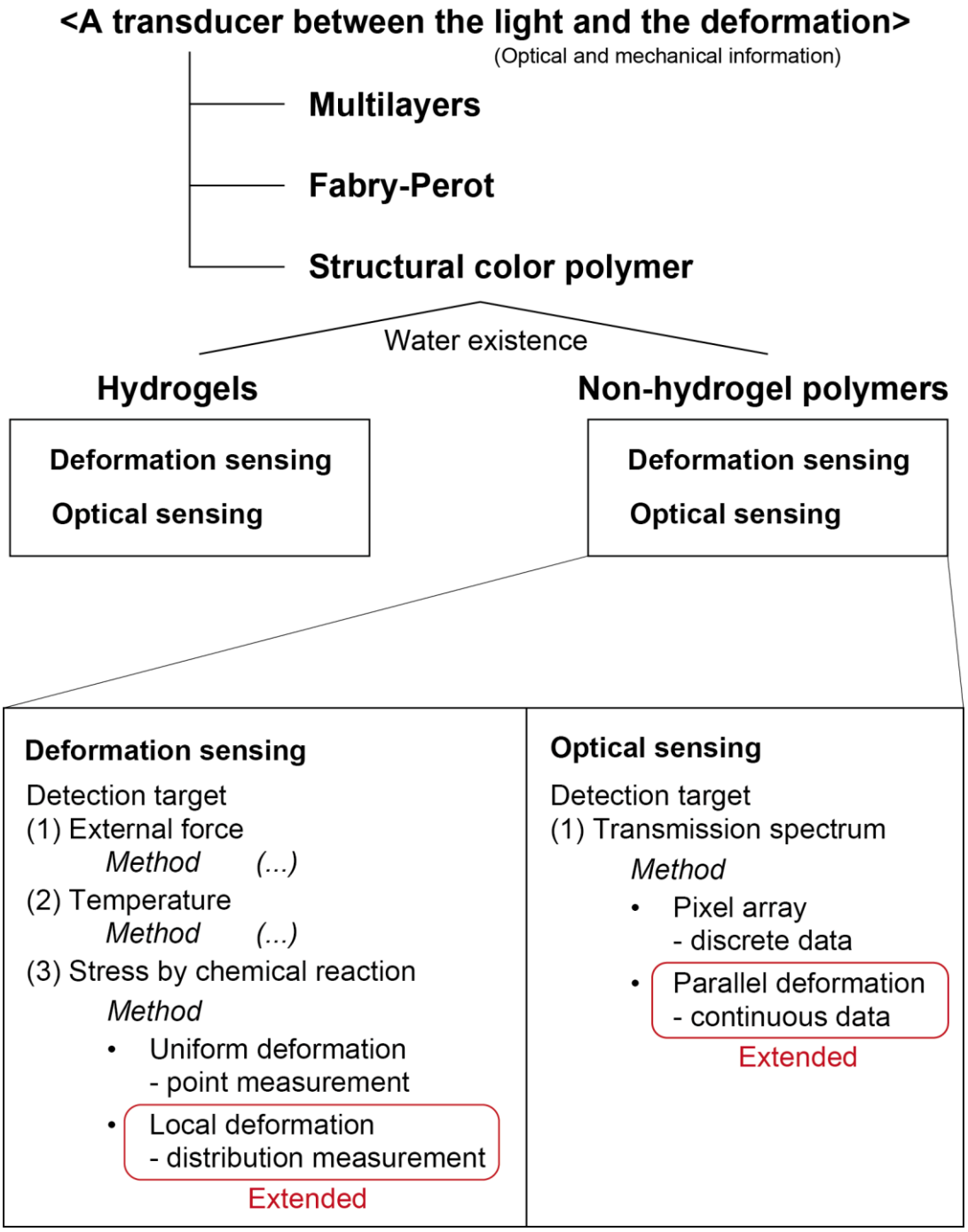

Figure 1.4 Significance of this dissertation. As a transducer between the light and deformation, the structural color polymer has an important role because of the small elasticity (soft). This dissertation provides functional extensions of the sensing methodology in deformation and optical sensing.

1.5.1 In-Line Microliter Liquid Spectrum Monitoring Sensor

The presented in-line microliter liquid spectrum monitoring sensor consisted of the structural color polymer, a white LED, a photodiode, a glass capillary, and a compression mechanism. The minimum structure contained electric wires without causing an electrical short due to water, owing to the non-hydrogel polymer. The LED light was reflected on the structural color polymer with a specific wavelength adjusted by the compression mechanism. After that, the light passed through the liquid in the glass capillary and reached the photodiode. The output voltage from the photodiode was analyzed after all data with every wavelength were obtained. This device had a novelty in that the external compression of the structural color polymer was applied to the long-term monitoring sensor without water leaking from the polymer.

1.5.2 Lithium Battery Stress Monitoring Sensor

The presented stress monitoring sensor displayed the deformation status between the electrodes in the lithium battery with the reflective light on the sensor, also working as a separator. The structural color polymer of silica and PEGPEA did not interrupt the ion exchange in the polymer. During the cyclic test of charging and discharging 100 times, the sensor showed mechanical stress by color changes due to microbubbles and dendrite growth. The sensor had a novelty in that the structural color polymer enabled long-term direct observation of mechanical stress in the separator without losing the separator function.

1.6 Dissertation Outline

This dissertation is composed of 5 chapters as below:

Chapter 1 describes the background, the purpose, and the concept of this dissertation.

Chapter 2 details the principles of structural color polymers. The ideal structure of the microsphere-dispersed structural color polymer is first described, while the amorphous

structure is described second.

Chapter 3 explains the fabrication methods and structure analysis of the fabricated structural color polymers. The analysis with the SEM (scanning electron microscope) images revealed that the fabricated structural color polymer had an amorphous structure of silica nanoparticles.

Chapter 4 examines color detection with the in-line microliter liquid color monitoring sensor. The sensor achieved color detection between green and yellow by changing the wavelength of the reflective light on the structural color polymer. The sensor also detected the difference in pH by using a BTB (bromothymol blue) solution. The durability of the sensor is also discussed.

Chapter 5 focuses on observation with the stress monitoring sensor in a lithium battery. The stress sensor revealed when and where microbubbles or dendrites occurred in the battery. The stress sensor also achieved long-term observation during the charging/discharging cyclic test 100 times.

Chapter 6 concludes this dissertation with a discussion of prospects for the sensor of the non-hydrogel structural color polymer.

CHAPTER 2.
PRINCIPLES OF STRUCTURAL COLOR POLYMERS

2.1 Introduction

In this chapter, the principles of structural color in the structural color polymers with nanoparticles are discussed. The ideally ordered structure with the nanoparticles is the first description. To decrease the angle dependence of reflective light, the amorphous structure is also important. Thus, the theoretical principles of the amorphous structure are introduced secondly.

2.2 Definition of Symbols

The symbols used in this chapter are as follows.

d	distance between particles [nm]
λ	reflective wavelength [nm]
n_{eff}	efficient refractive index [-]
θ	irradiation angle [°]
n_{particle}	refractive index of particles [-]
n_{polymer}	refractive index of polymer [-]

ϕ	volume fraction [-]
V_{particle}	volume of particles [μL]
V_{polymer}	volume of polymer [μL]
α	scale parameter [-]
r	particle radius [nm]
σ	mechanical stress [Pa]
E	Young's modulus [Pa]
ε	strain [-]
l	height of polymer [m]
Δl	deformation of polymer [m]
Δd	difference of particle distance [nm]
$\Delta\lambda$	difference of reflective wavelength [nm]

2.3 Ideal Structure of Nanoparticles in Structural Color Polymer

The ideal structure of the structural color polymer consists of ordered and perfect nanospheres in a polymer (Fig. 2.1). In this structure, the wavelength of the reflective light λ is determined by Bragg-Snell law,

$$\lambda = 2d\sqrt{n_{\text{eff}}^2 - \sin^2\theta}, \tag{2. 1}$$

where n_{eff} is written as

$$n_{\text{eff}} = \sqrt{n_{\text{particle}}^2\phi + n_{\text{polymer}}^2(1-\phi)}. \tag{2. 2}$$

The ϕ is expressed as

$$\phi = \frac{V_{\text{particle}}}{V_{\text{particle}}+V_{\text{polymer}}}. \tag{2. 3}$$

The equation (2.1) shows the reflective wavelength is proportional to the distance between particles. Based on this equation, deformation of the polymer is converted to color change. However, θ is also a variable in equation (2.1), while n_{eff} is constant after materials are mixed. Thus, the reflected color is changed depending on the irradiation angle. This is called "angle

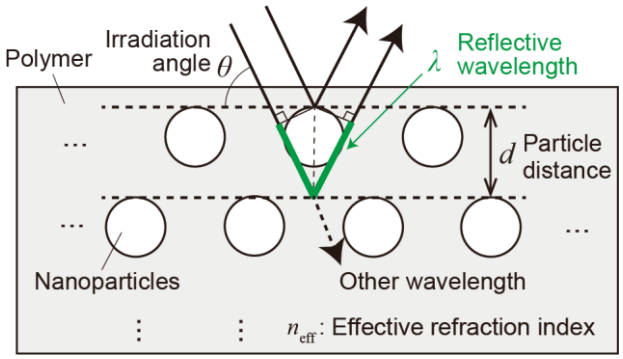

Figure 2.1 Explanation of Bragg-Snell law. Nanoparticles are aligned periodically in a polymer with particle distance d. The light with irradiation angle θ is reflected. In this time, the light with a specific wavelength λ is reflected strongly. The effective refraction index n_{eff} is calculated from the refraction index of particles and polymer.

dependence", which is often seen as a problem in some applications such as displays or color indicators.

The relationship between strain and stress is expressed as

$$\sigma = E\epsilon \tag{2. 4}$$

where strain ε is written as

$$\epsilon = \frac{\Delta l}{l} \tag{2. 5}$$

(Figure 2.2). When the difference in the particle distance is considered, this strain is also written as

$$\epsilon = \frac{\Delta d}{d}. \tag{2. 6}$$

Moreover, λ is proportional to d from Equation (2.1). Thus, Equation (2.6) is rewritten as

$$\epsilon = \frac{\Delta \lambda}{\lambda}. \tag{2. 7}$$

From Equations (2.4) and (2.7), mechanical stress is calculated as

$$\sigma = \frac{E\Delta \lambda}{\lambda}. \tag{2. 8}$$

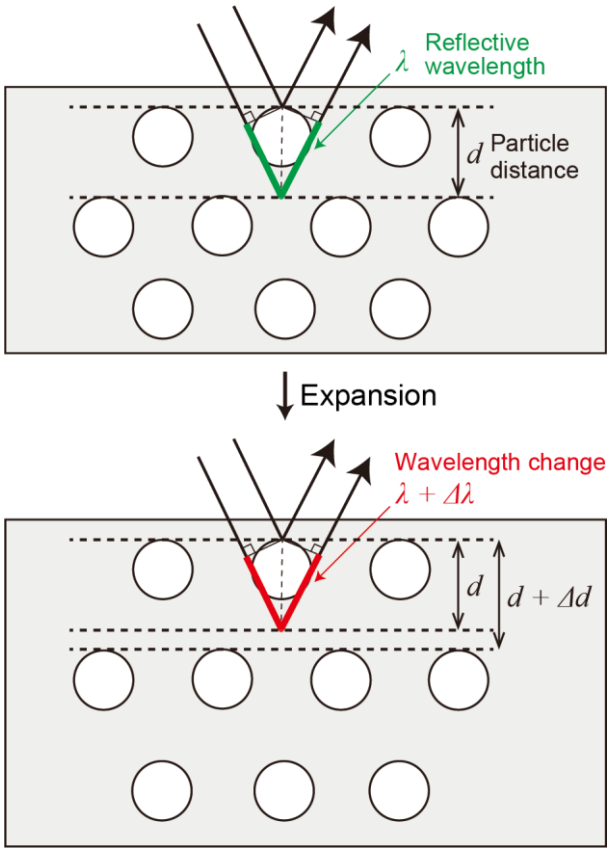

Figure 2.2 The expansion of the structural color polymer causes the wavelength change to larger wavelength. From the difference of the wavelength $\Delta\lambda$, the mechanical stress was calculated.

This equation suggests that mechanical stress can be calculated from measurements of the initial reflective wavelength λ and the difference in the reflective wavelength $\Delta\lambda$.

2.4 Amorphous Structure of Nanoparticles in Structural Color Polymer

To decrease the angle dependence, the amorphous structure of nanoparticles has been reported. In 2009, K. Ueno *et al*. fabricated angle-independent structural color in ionic liquid [49]. After that, Y. Takeoka *et al*. showed angle-independent structural color in a

hydrogel [50]. The FFT (fast Fourier transform) of SEM images showed the disordered alignment of particles. However, the following analysis showed that the particles had a short-range correlation due to electrostatic force [51]. Such a structure is sometimes called the amorphous structure. The amorphous structure has been fabricated by the self-assembly method, which is easier than the manual assembly methods shown in Section 1.3.

In strict calculation, this angle-independent structural color was also caused by Mie scattering [52,53]. In Mie scattering, particles have larger diameters than the particles in Rayleigh scattering. The scale parameter is expressed as

$$\alpha = \frac{2\pi r}{\lambda} \tag{2. 9}$$

and $\alpha > 0.13$ was said to be appropriate for Mie scattering [54]. In the following experiments, α was in the range of 0.67-1.57.

Mie scattering has a complex derivation from Maxwell's equations. Moreover, the dispersed particles have a different refractive index from the dispersive media. Such a situation is expressed by the scattering mean free path l_s, which is written as

$$\frac{1}{l_s} = \rho \int_{4\pi} \frac{d\sigma}{d\Omega}(\theta) S(\theta) d\Omega. \tag{2. 10}$$

The $\frac{d\sigma}{d\Omega}$ is the differential scattering cross section and S is the static structure factor (detail for Appendix B). The S depends on the particle structure shown as Figure 2.2. The calculation of S suggested the result was similar to the Bragg-Snell law (2.1) (Figure 2.3 (a)-(c)) [52]. Thus, the equation (2.1) was still used in the following experiments for engineering.

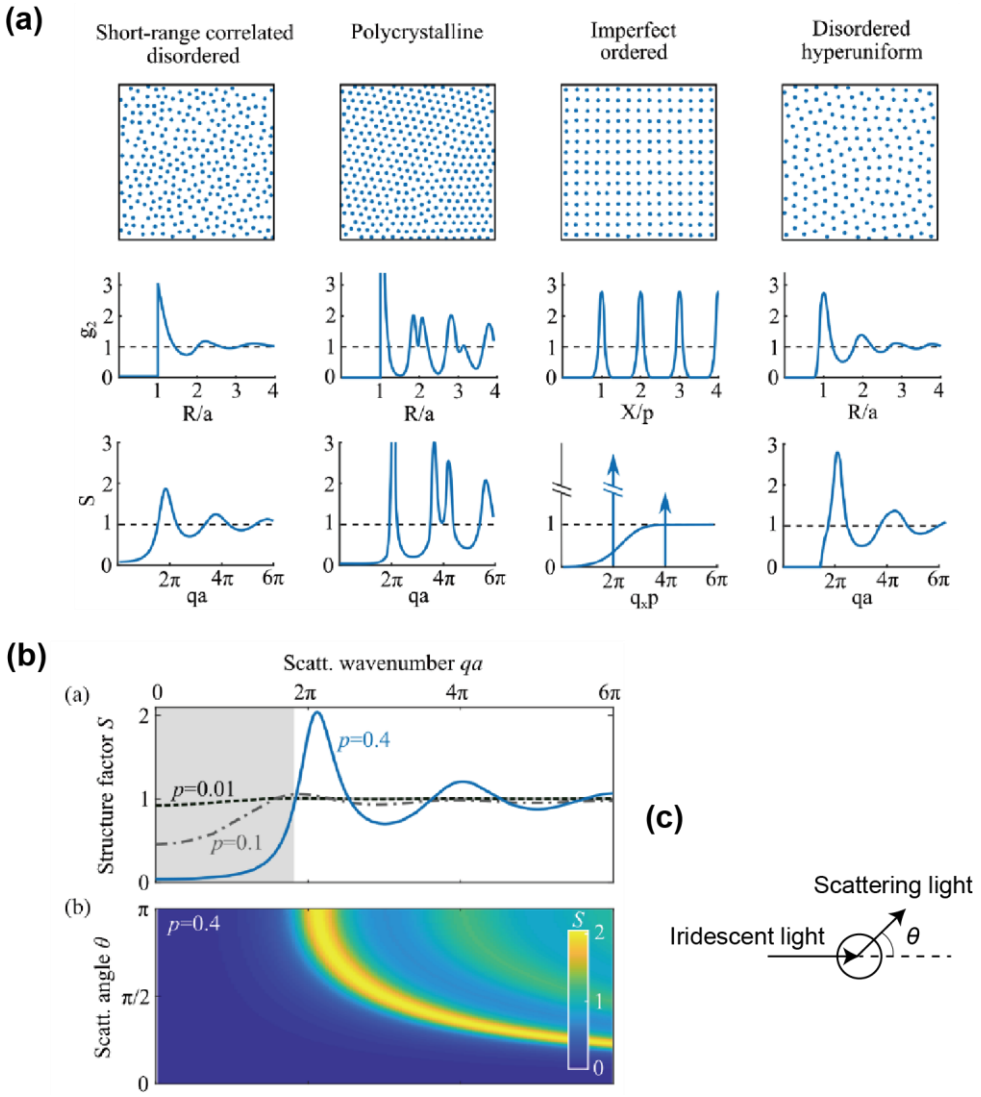

Figure 2.3 (a) Relationship between the static structure factor S and actual particle structure. Here, a is particle diameter and q is the wavenumber in the media. The S has peaks at $qa = 2\pi$. [52] (b) Relationship between S and the scattering angle θ. $\theta = \pi$ means backscattering, similar to Bragg reflection. [52] (c) Definition of the scattering angle θ.

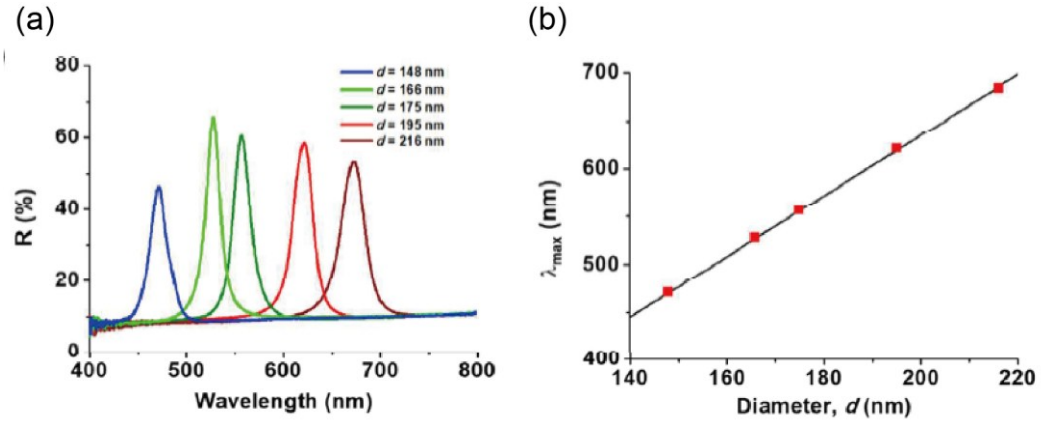

Figure 2.4 Relationship between the silica particle diameter and the reflective wavelength [30]. (a) Reflective spectra in five kinds of silica particles. The volume fraction was 0.33. (b) Diameter dependence of the peaks of the reflective spectra.

2.5 Particle Diameter and Reflective Wavelength

Previous research [30] showed that the reflective wavelength on the structural color polymer increased linearly corresponding to the particle diameter when the volume fraction of the silica particles was constant (Figure 2.4). From the graph, it has been assumed that the particle distance was also constant due to the solvation layers caused by the electrostatic repulsion force between particles. The particle diameter was adjustable in the silica particle fabrication process (Stöber method [30]). The silica particles in this dissertation were produced in a factory to suppress the variation of the particle diameter.

2.6 Viscoelastic Model of Polymers

As written, the structural color polymer was made of polymer and microparticles. Actually, the polymer has viscoelastic properties. In this section, the viscoelastic model of polymers is explained.

When the polymer is extended vertically, the polymer simultaneously shrinks horizontally (Figure 2.5 (a)). Thus, there are two strains: the longitudinal strain (vertical) and the transverse strain (horizontal). Those strains are written as

$$\epsilon_L = \frac{\Delta l_L}{l_L} \tag{2. 11}$$

$$\epsilon_T = \frac{\Delta l_T}{l_T}. \tag{2. 12}$$

With the strains, Poisson's ratio is defined as

$$\nu = -\frac{\epsilon_T}{\epsilon_L}. \tag{2. 13}$$

The Poisson's ratio has a range of 0-0.5; for example, copper has 0.34 and PDMS (poly-dimethylsiloxane) has 0.49 [55].

The stress-strain diagram often suggests nonlinearity of the polymer's elasticity (Figure 2.5 (b)). Equation (2. 4) is rewritten as

$$\sigma = E(\epsilon)\epsilon \tag{2. 14}$$

when the material does not follow the Hooke's law.

Moreover, some polymers have time-dependent deformation properties such as stress relaxation and creep. The stress relaxation means that the stress in constant strain has decreased depending on time. The creep means that the strain with constant stress has increased depending on time. Especially the stress relaxation happens rapidly, sometimes causing errors of deformation prediction. The models of the stress relaxation are suggested as follows:

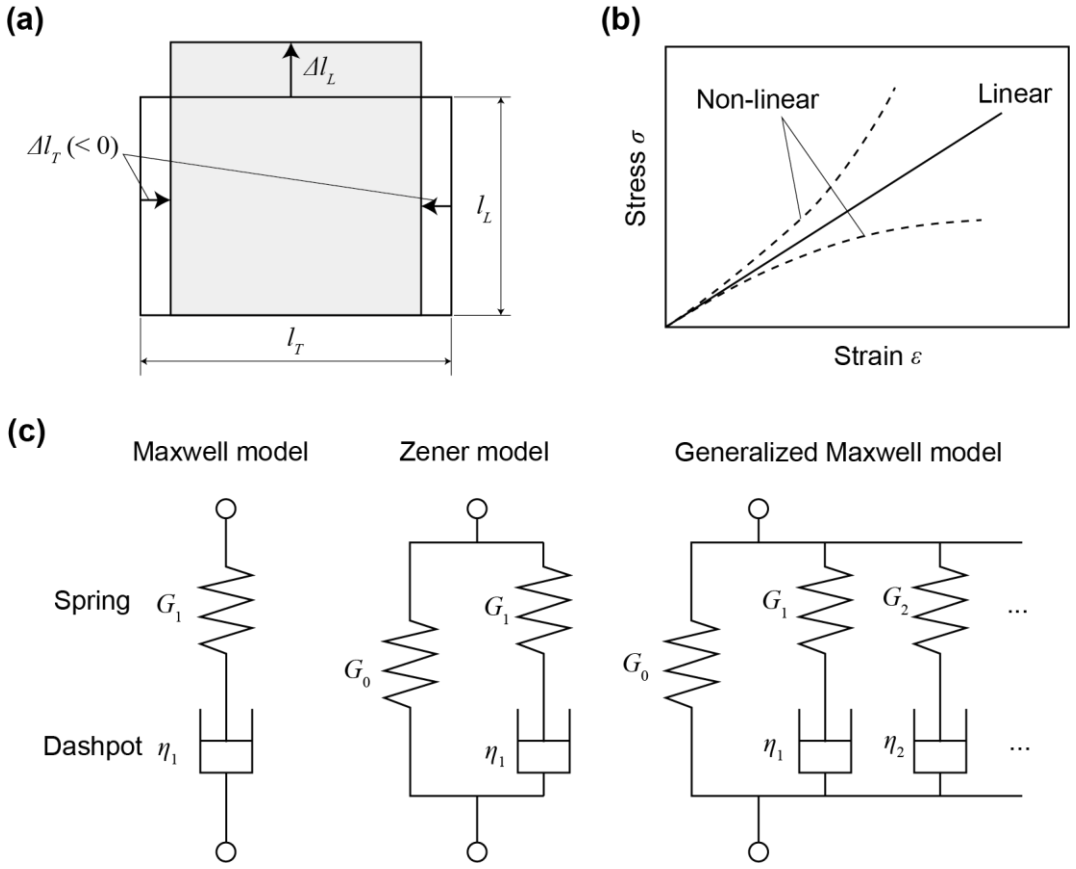

Figure 2.5 Viscoelastic polymer model. (a) Deformation model of a polymer. The initial shape is shown with dimensions l_L and l_T. The deformed shape is shown with a gray box. (b) An example of the stress-strain diagram. Polymers often have non-linear curves in the diagram. (c) Stress relaxation models of the viscoelastic polymer shown by springs and dashpots. The increase of the spring and dashpot factors leads to fitting of the measured stress relaxation curve.

Maxwell model $$G(t) = Ge^{-\frac{t}{\tau}} \quad (2.15)$$

Zener model $$G(t) = G_0 + G_1 e^{-\frac{t}{\tau}} \quad (2.16)$$

Generalized Maxwell model $$G(t) = G_0 + \sum_{i=1}^{n} G_i e^{-\frac{t}{\tau_i}} \quad (2.17)$$

when

$$G(t) = \frac{\sigma(t)}{\epsilon_0}. \quad (2.\ 18)$$

The strain ε_0 is a constant value and τ is relaxation time expressed as $\tau = \eta/E$ (also see Figure 2.5 (c)). $G(t)$ is seen as the combination of springs (elasticity modulus G_i) and dashpots (viscosity coefficient η_i). The generalized Maxwell model has the capability of precise expression with most viscoelastic materials.

2.7 Conclusion

In this chapter, principles of the structural color polymer were introduced. The ordered structure of particles has an angle dependence, resulting in color changes when the viewing point is changed. The amorphous structure of the particles prevents the color change depending on the viewing angle. This feature is preferred for devices using colors, such as displays and color indicators.

CHAPTER 3. FABRICATION OF A STRUCTURAL COLOR POLYMER

3.1 Introduction

In this chapter, the fabrication of a silica-PEGPEA structural color polymer and its characteristics are explained. First, the fabrication process is illustrated. Silica nanoparticles are self-assembled due to electrostatic forces by the washing process. The polymer fabrication is based on UV curing, leading to keeping the structure of silica nanoparticles. Second, the structure of the particles is observed with SEM. The alignment pattern of the silica nanoparticles is calculated with image analysis software. Third, the mechanical characteristics of the fabricated polymer are measured.

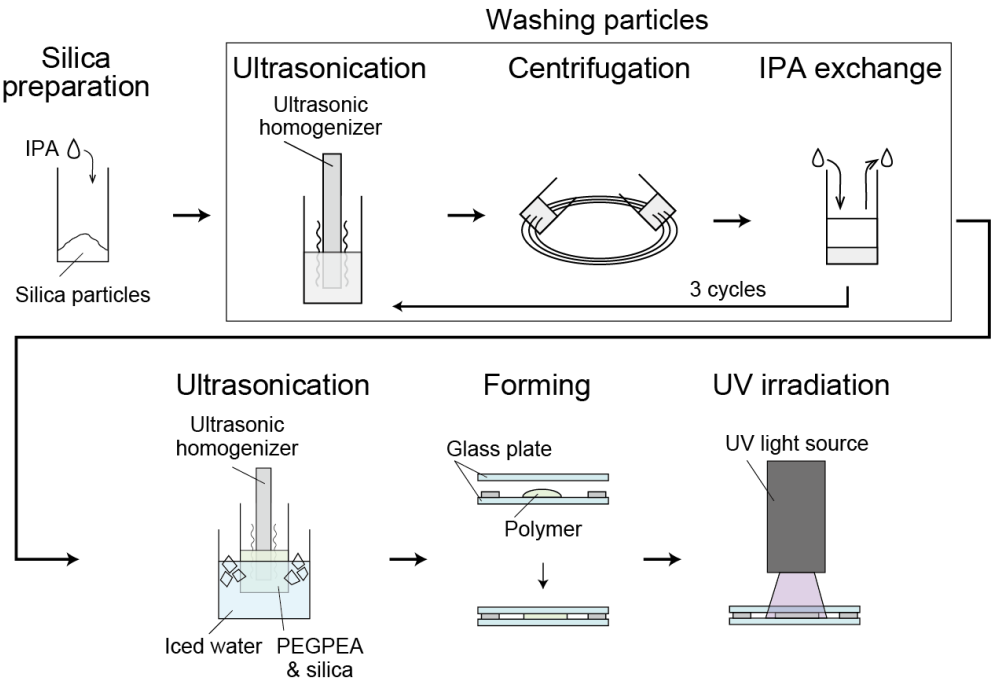

Figure 3.1 Fabrication process of a structural color polymer based on silica and PEGPEA. Silica particles were washed by IPA to induce electrostatic force. After that, silica particles and PEGPEA were mixed with the ultrasonic homogenizer. The mixture was infused on a glass plate and compressed to target thickness. Finally, UV light was irradiated to the mixture.

3.2 Fabrication Process of a Silica-PEGPEA Structural Color Polymer

The fabrication process of the silica-PEGPEA polymer is described in this section (also see Figure 3.1). The bottle of the silica nanoparticles (SG-SO200D, Sukgyung AT Co., Ltd.), whose diameter was 202 nm (factory measured value), was bought [30,56,57]. Next, 0.35 g of the silica nanoparticles were dispersed in IPA (2-propanol) by 1 min of ultrasonication. The silica nanoparticles were centrifuged for 10 min at 6200 rpm. The IPA in the top layer was exchanged with a new IPA. These washing processes, dispersion, centrifugation, and IPA exchange, were conducted three times to induce the electrostatic force between the silica nanoparticles. After that, IPA was completely evaporated from the silica at

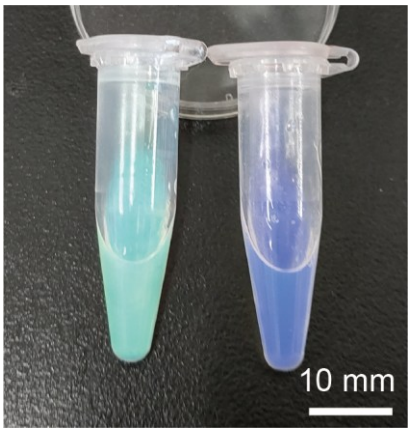

Figure 3.2 The fabricated pre-polymer.

75 °C. This process clarified the amount of IPA in the following process. Next, 200 μL PEGPEA, 200 μL IPA, and 2.0 μL Darocur 1173 (photoinitiator) were added to the washed silica nanoparticles. The IPA in this process was just for the dispersion medium. Those materials were mixed by ultrasonication with cooling by ice water. The completely dispersed materials were next heated at 75 °C to remove the IPA. After approximately 2 h of IPA evaporation, the pre-polymer was obtained. (Figure 3.2) For polymer shaping, the pre-polymer was set between two fluorine-coated glass plates. The fluorine-coating agent was CYTOP (AGC chemicals). Then, shear stress was applied to the pre-polymer manually to make the structural color brighter. In winter, this process was conducted on a heater at 55 °C because the viscosity of the pre-polymer tended to be low at 50-60 °C. After that, the UV light (MAX-350, Asahi Spectra Co., Ltd.) was irradiated to the pre-polymer at 50 mW/cm^2 for 30 s. Finally, if needed, Fluoro Surf (FluoroTechnology Co., Ltd.) coating was applied to the shaped polymer to reduce the surface adhesiveness. The initial color was red with the above processes.

To change the initial color, SG-SO180D (diameter = 180 nm) particles for green and SG-SO150D (diameter = 150 nm) particles for blue were applicable. The diameters of the silica particles were measured with SEM images (Figure 3.3). For the diameter measurement, the three-point method was used. The measurement was conducted in the software ImageJ with my add-in of the three-point method (see Appendix). As a result, the

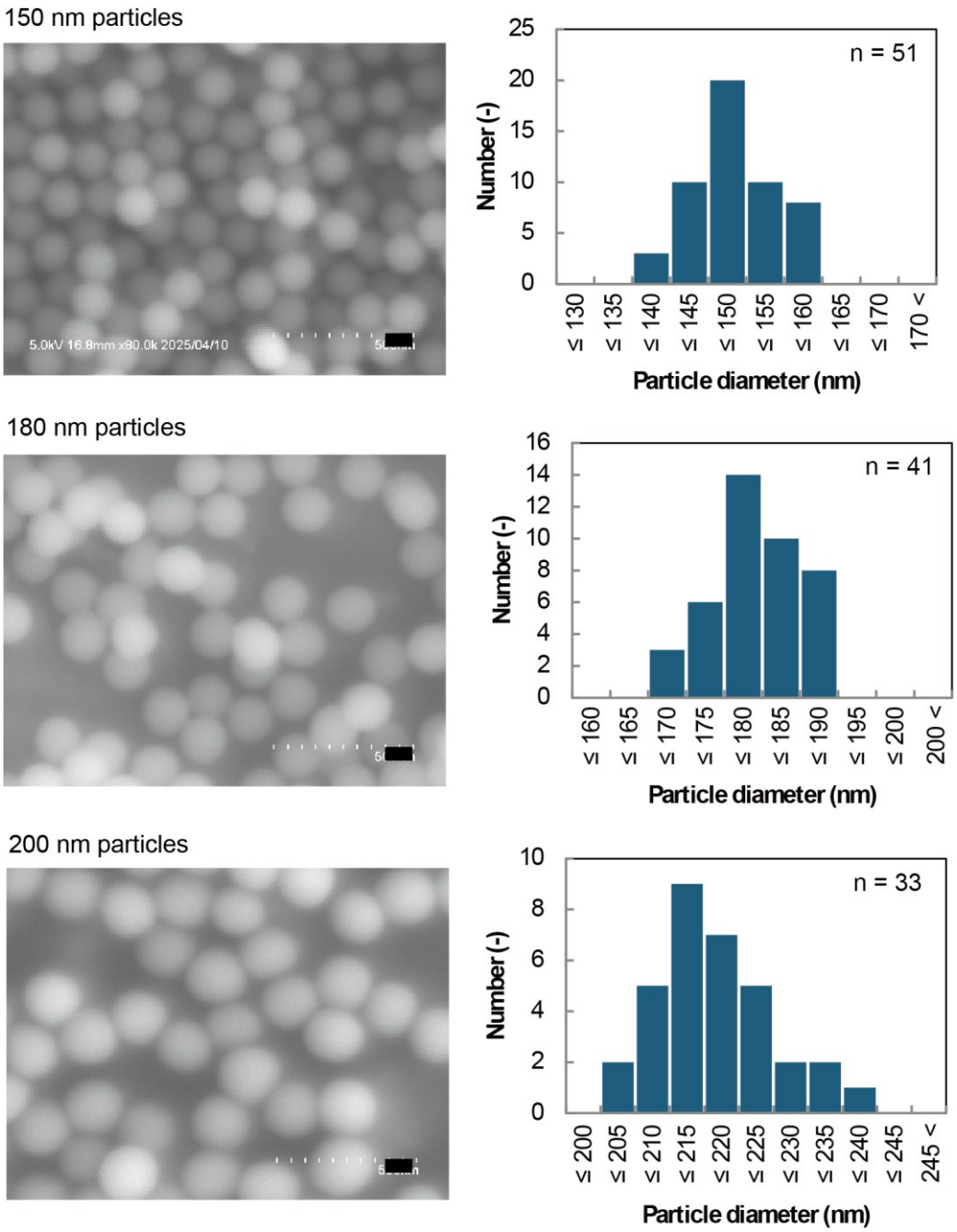

Figure 3.3 The SEM images and histograms of the used silica particles. Scale bar = 100 nm. The histograms showed the particle diameters followed normal distribution.

average particle diameters were as follows: SG-SO200D was 216.7 ± 26.1 nm, SG-SO180D was 179.3 ± 14.3 nm, and SG-SO150D was 148.6 ± 10.6 nm (±s.d.). All three kinds of

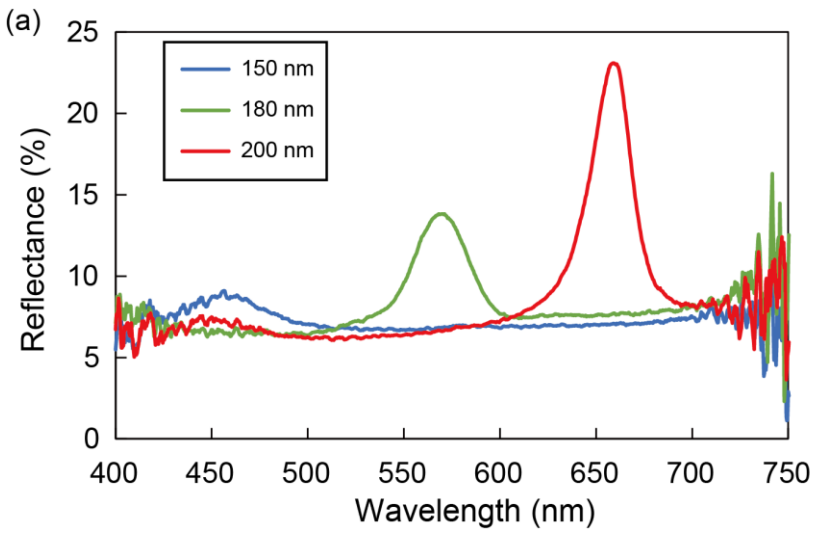

(c)

Measured λ_{peak} (nm)	Calculated λ_{peak} (nm)
456.49	464.53
569.99	555.34
659.37	665.97

Figure 3.4 (a) The spectra of the structural color polymer sheets with three kinds of silica particles. (b) Relationship between the particle distance d and the gap between the particles d_g. (c) The measured peak wavelength λ_{peak} and calculated λ_{peak} by Equation (3.2).

particles had normal distributions, shown in the histograms. With the particles, 0.1 mm-thick silica-PEGPEA structural color polymer sheets were fabricated to measure the reflective spectra. The sheet permeated an electrolyte to make the color brighter. Here, the used electrolyte was a 1.0 M solution of LiTFSI (lithium bis(trifluoromethane-sulfonyl)imide) in EC (ethylene carbonate) and DMC (dimethyl carbonate) solution. The spectra were measured with a visible light spectrometer (USB2000+, Ocean optics). The result (Figure 3.4) showed that each sheet had a peak of the reflective wavelength. The sheet containing 200-nm silica particles had a peak at 659.4 nm. Similarly, corresponding peaks were observed at 570.0 nm and 456.5 nm for 180-nm and 150-nm particles, respectively. From the result, it was confirmed that the particle diameters and reflective wavelengths had a linear relationship. The equation was expressed as

$$\text{Theoretical:} \quad \lambda_{peak} = kd = k(D + d_g) \tag{3.1}$$

$$\text{Experimental:} \quad \lambda_{peak} = 2.96D + 24.98 = 2.96(D + 8.44)\ (\text{nm}) \tag{3.2}$$

where D was the particle diameter, k was a constant, and d_g was the gap between the particles (Figure 3.4(b)). Note that Equation (3.2) contained errors due to the number of plots.

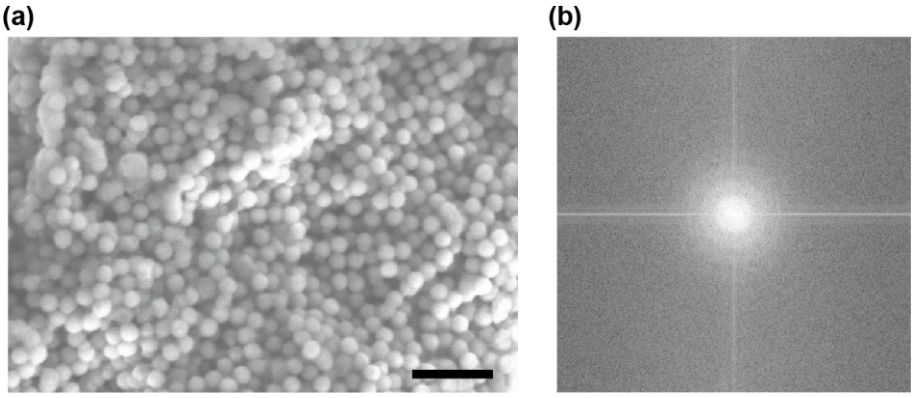

Figure 3.5 (a) SEM image of the fabricated structural color polymer. Scale bar = 1 μm. (b) 2D-FFT image of the SEM image. The white circle showed there was no order.

3.3 Structure Analysis of the Fabricated Polymer

The particle structure of the red polymer was observed with SEM (Scanning electron microscope, SU-70, Hitachi High-tech Corp.) to confirm which structure the particles have (Figure 3.5 (a)). The red polymer was cut with a disposable surgical knife after the polymer had been cooled by liquid nitrogen. The cut surface was set on the observation table of the SEM. The image was analyzed with two methods: the first was 2D-FFT (two-dimensional fast Fourier transform) of the SEM image, and the other was the distance distribution between the adjacent particles. Both analyses were calculated with image processing software (ImageJ).

When particles have an ordered structure, a hexagon pattern of six dots will be observed after 2D-FFT [51]. However, the result of 2D-FFT for the fabricated polymer showed no pattern (Figure 3.5 (b)). This suggested that the fabricated polymer had a disordered structure.

Next, the distribution of the particle distances was calculated. The SEM image of the fabricated polymer had shadows. Thus, CLAHE (contrast limited adaptive histogram equalization) was used to reduce the shadow (Figure 3.6 (a)). The CLAHE caused some noise,

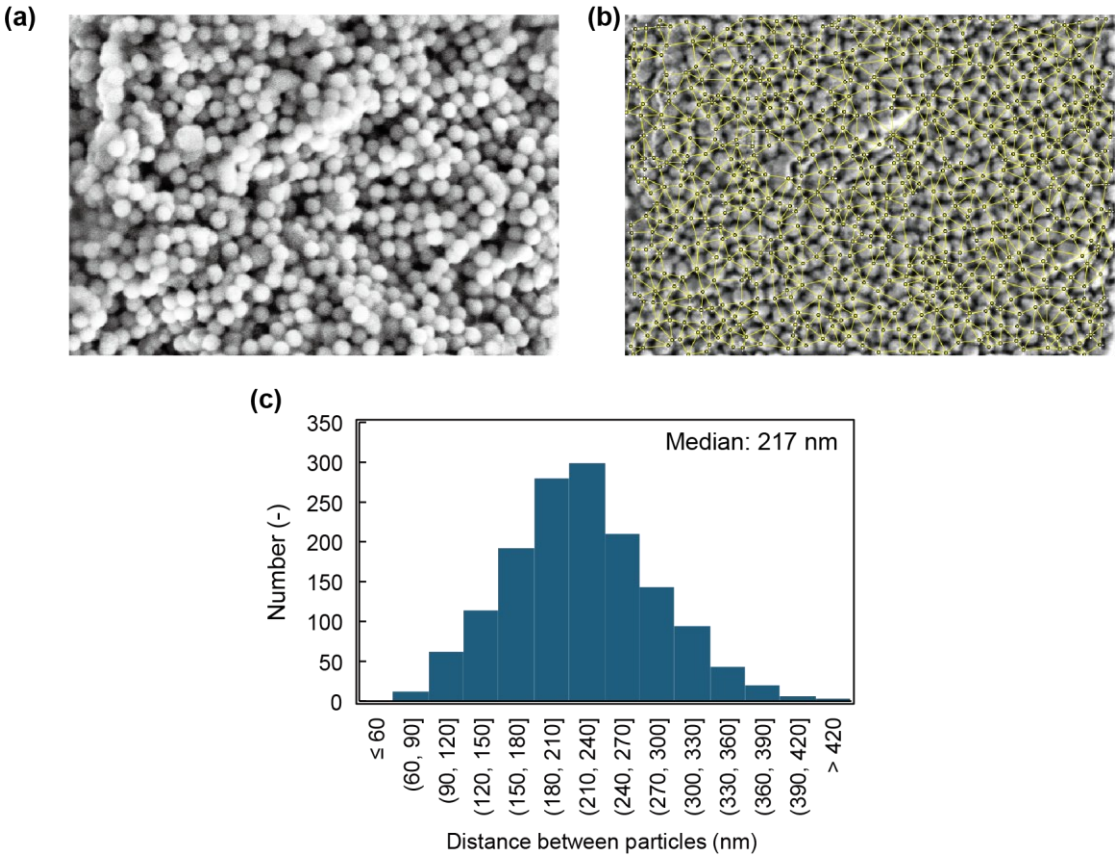

Figure 3.6 (a) CLAHE process was applied to the SEM image (Figure 3.3 (a)). (b) The result that Gabriel graph algorithm was applied to Figure 3.4 (a). (c) Histogram of particle distance distribution. Median was 217 nm.

reduced by noise smoothing. After that, maxima detection was conducted to detect the center of the particles. Finally, the Gabriel graph was used for adjacent point detection and distance measurement (Figure 3.6 (b)). The yellow lines in Figure 3.6 (b) show the adjacent distance calculated by the Gabriel graph algorithm. The result of the distance distribution showed that the particle distance histogram had a normal distribution (Figure 3.6 (c)). The median distance between the adjacent particles was 217 nm. The normal distribution suggested that the structural color polymer had a correlated structure. Such a structure came from the electrostatic force caused by the washing process [30].

When the particle distance is already known, the polymer color is able to be

estimated. The effective refractive index n_{eff} was calculated as n_{eff} = 1.478. This value was calculated from Equation (2.2), (2.3), diffraction ratio of silica (SiO_2) $n_{particle}$ = 1.45, diffraction ratio of PEGPEA $n_{polymer}$ = 1.50 [30], volume of silica $V_{particle}$ = 159 μL, and volume of PEGPEA $V_{polymer}$ = 200 μL. When d = 217 nm and n_{eff} = 1.478 were substituted for Equation (2.1), λ was calculated as 644 nm. This calculated value was close to the measured value of 659 nm peak. Therefore, it was confirmed that the fabricated polymer had an amorphous structure (disordered and correlated) for the color reflection.

3.4 Mechanical Characteristics of the Fabricated Polymer

3.4.1 Stress-Strain Diagram (Compression)

Next, the mechanical properties of the fabricated structural color polymer were evaluated. First, the elasticity of the silica-PEGPEA structural color polymer was compared with the elasticity of pure PEGPEA and silica-AAm (acrylamide) structural color gel (Figure 3.7 (a)). The silica-AAm structural color gel was fabricated with the following process: (1) MP-1040 silica colloid (particle diameter = 100 nm, Nissan Chemical) was desalted by MB AG® 501-X8. (2) 150 mg/mL acrylamide solution with *N,N*'-Methylenebis(acrylamide) (1/120 volume of AAm) was fabricated. (3) The desalted silica and a polymerization initiator Irgacure 1173 were added to the AAm solution. (4) 50 mW/cm^2 of UV light was irradiated to obtain the structural color gel.

The deformation and the force data were obtained with an elasticity measurement instrument (Figure 3.7 (b), force meter: FGP-1, Nidec SHIMPO, 1-axis stage: OSMS26-50, OptoSigma). The probe diameter was 3 mm, larger than the samples (silica-PEGPEA: 2 mm diameter, pure PEGPEA: 2 × 2 mm, silica-AAm: 2.5 mm diameter) to follow the standard measurement method (JIS K 6254: 2016).

Young's modulus of the silica-PEGPEA was calculated as 564 kPa (strain ≤ 0.25) from the graph (Figure 3.7 (a)). This value was larger than the value of the pure PEGPEA

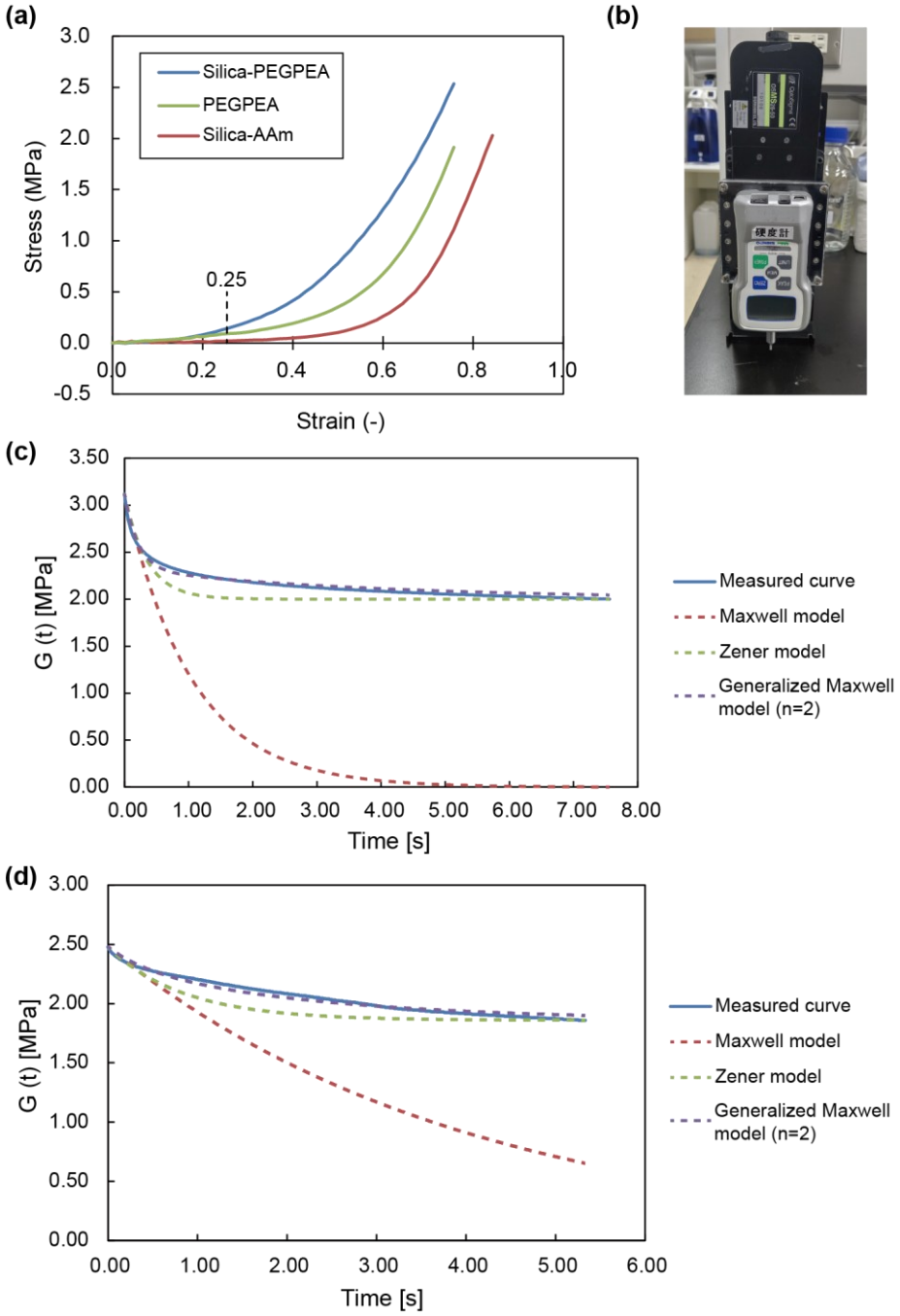

Figure 3.7 Mechanical properties of the fabricated structural color polymer in compression. (a) Stress-strain diagram of silica-PEGPEA, pure PEGPEA, and silica-Aam (acrylamide) in compression. (b) The elasticity measurement instrument. (c) Stress relaxation of the structural color polymer (silica-PEGPEA). (d) Stress relaxation of PEGPEA.

(360 kPa) and silica-AAm (79 kPa). Moreover, the strain-stress curves were not linear at

larger strains, increasing exponentially. Although the volume ratio of the silica nanoparticles was high in silica-PEGPEA polymer (calculated as 44.3%), the curve shape was similar to the pure PEGPEA polymer. The larger elasticity of the silica-PEGPEA possibly came from the silica particles, whose Young's modulus is known as 70 GPa [58]. As an aside, the silica-AAm hydrogel had the lowest elasticity, possibly caused by the structure containing water molecules.

In addition, stress relaxation was confirmed after the compression of the polymer was stopped (Figure 3.7 (c)-(d)). The stress relaxation of the silica-PEGPEA structural color polymer (Figure 3.7 (c)) had a relaxation time, 3.3 s for 90% relaxation. This relaxation time is smaller than the relaxation time of pure PEGPEA (Figure 3.7 (d), 3.9 s for 90% relaxation). This phenomenon showed that the structural color polymer had viscoelastic properties as well as pure PEGPEA. It was also expected that this phenomenon would cause signal delays in compression, limiting the minimum measurement time in the experiments of the in-line color sensor.

From the two curves and Equations (2.15)-(2.17), I estimated the viscoelastic model of the silica-PEGPEA and pure PEGPEA. To fit the estimated curve to the measured curve, I first fit the slopes around 0 s by changing the parameters. As a result, the generalized Maxwell model (n = 2) was the most fitted in both curves. The parameters of the estimated silica-PEGPEA relaxation curve (the broken violet line in Figure 3.5 (c)) were G_1 = 0.80, τ_1 = 0.21, G_2 = 0.32, τ_2 = 3.80, and G_0 = 2.001. On the other hand, the parameters of the estimated pure PEGPEA relaxation curve (the broken violet line in Figure 3.5 (d)) were G_1 = 0.15, τ_1 = 0.40, G_2 = 0.47, τ_2 = 2.20, and G_0 = 1.859. Thus, both polymers were approximated well with the viscoelastic model.

3.4.2 Stress-Strain Diagram (Tensile)

Tensile stress of the structural color polymer was also measured. To measure the tensile stress, an 8.3 mm (width) × 12.7 mm (length) × 0.7 mm (thickness) test specimen (Figure 3.8 (a)) and specimen clamping tools were prepared (Figure 3.8 (b)). After the specimen was clamped, the initial length between the tools was 6.15 mm. The pulling speed

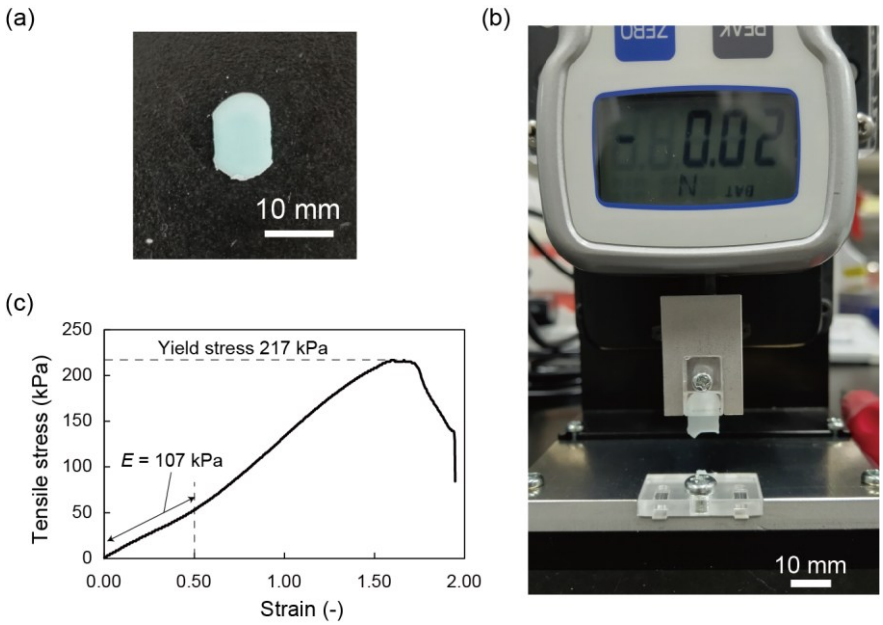

Figure 3.8 Mechanical properties of the fabricated structural color polymer in tensile. (a) Specimen of silica-PEGPEA in tensile. (b) The cramping tools attached to the elasticity measurement instrument. (c) Stress-strain diagram of the silica-PEGPEA in tensile.

was set to 1.0 mm/s. The result showed that Young's modulus of the polymer in tensile was 107 kPa (strain ≤ 0.50) and the yield stress was 217 kPa (Figure 3.8 (c)). The Young's modulus in tensile 107 kPa was smaller than in compression 564 kPa. This difference was possibly caused by the silica nanoparticles. The compressed particles obstructed large deformation. Note that Poisson's ratio was ignored in this calculation because it was difficult to measure the width in tensile. Therefore, Poisson's ratio was measured in the following part. The yield stress of 217 kPa suggested the limitation of color changes to larger wavelengths. Thus, the stress-sensing ability is limited by the yield stress.

3.4.3 Stress-Strain Diagram (Integrated Estimation)

Here, the calculated Young's moduli of the silica-PEGPEA polymer are E_{tensile} = 107 kPa (strain <0.50, Fig. 3.8(c)) and $E_{\text{compression}}$ = 564 kPa (strain < 0.25, Fig. 3.7 (a)). Both

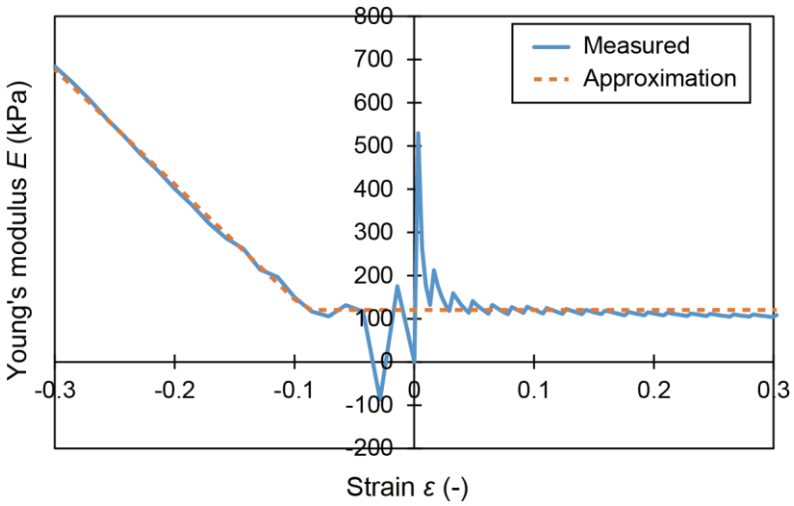

Figure 3.9 Young's modulus-strain diagram of the silica-PEGPEA polymer.

Young's moduli were calculated from nominal stress, not from true stress. When the strain was small enough to use the nominal stress for the calculation, an integrated Young's modulus-strain diagram was able to be drawn (Fig. 3.9). Here, compression was the negative direction and tensile was the positive direction. In small strain ε, large measurement errors of the elasticity measurement instrument were confirmed, causing difficulty in stress calculation with the structural color polymer sensing. Thus, the broken orange line (Fig. 3.9) was used as Young's modulus, whose equation was linearly approximated as

$$E\ (\mathrm{kPa}) = \begin{cases} -2661.5\,\epsilon - 121.9\ (-0.3 < \epsilon < -0.091) \\ 120\ (-0.091 \leq \epsilon < 0.3) \end{cases} \tag{3.3}$$

for ease of calculation. The measurement errors were expected to be decreased by the improvement of the stage moving resolution and the force resolution.

3.4.4 Poisson's Ratio

Next, the Poisson's ratio of the silica-PEGPEA structural color polymer was measured (Figure 3.10). The device was fabricated for the Poisson's ratio measurement. The diameter of the polymer was measured in four directions. The compression of the polymer was changed by a screw from 0.00 mm to 0.25 and 0.50 mm. The thickness of the polymer

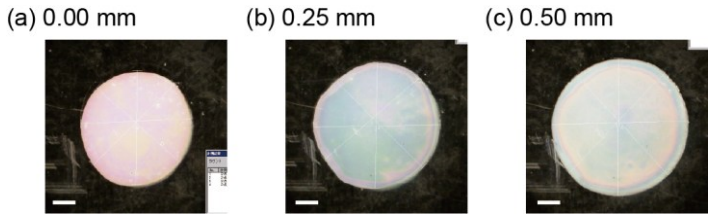

Figure 3.10 Poisson's ratio measurement of silica-PEGPEA polymer with the compression change. The measurement positions were shown in white lines. Scale bars are 1 mm. (a) Initial state of the polymer. (b) 0.25-mm compressed polymer. (c) 0.50-mm compressed polymer.

sample was 0.70 mm. The measurement was conducted at four positions for each condition. Then, the Poisson's ratio was calculated as 0.315 (0.25-mm compression) and 0.307 (0.50-mm compression) by using Equation (2. 13). Generally, Poisson's ratio of incompressible materials including pure elastomers tends to be around 0.5 (e.g. PDMS: 0.495 [55]), while many compressible materials have 0.3 of Poisson's ratio. Poisson's ratio of pure PEGPEA was 0.27-0.36 with the same measurement method (the edge of pure PEGPEA was fragile, causing large measurement errors). On the other hand, Poisson's ratio of pure SiO_2 is reported as 0.15 [58]. Here, Poisson's ratio of SiO_2 has a wide variety between 0.1 – 0.4 depending on the purity. The used SiO_2 nanoparticles were ensured to be > 99.9% purity by Sukgyung AT, possibly leading to a close value to 0.15. From the above, it seemed that pure PEGPEA was dominant in deciding the Poisson's ratio of silica-PEGPEA polymer, resulting in a typical Poisson's ratio of the general compressive materials.

3.4.5 Thermal Deformation

The temperature change is also a deforming factor of the polymer. To investigate the effects of thermal deformation, the dimensions of the polymer at room temperature (25°C) and high temperature (68°C) were measured. The temperature was adjusted by a film heater (HET-ON4) (Figure 3.11 (a)). The film heater had a thermistor to provide feedback on the temperature. The temperature distribution at 68°C (the thermistor value) was measured with

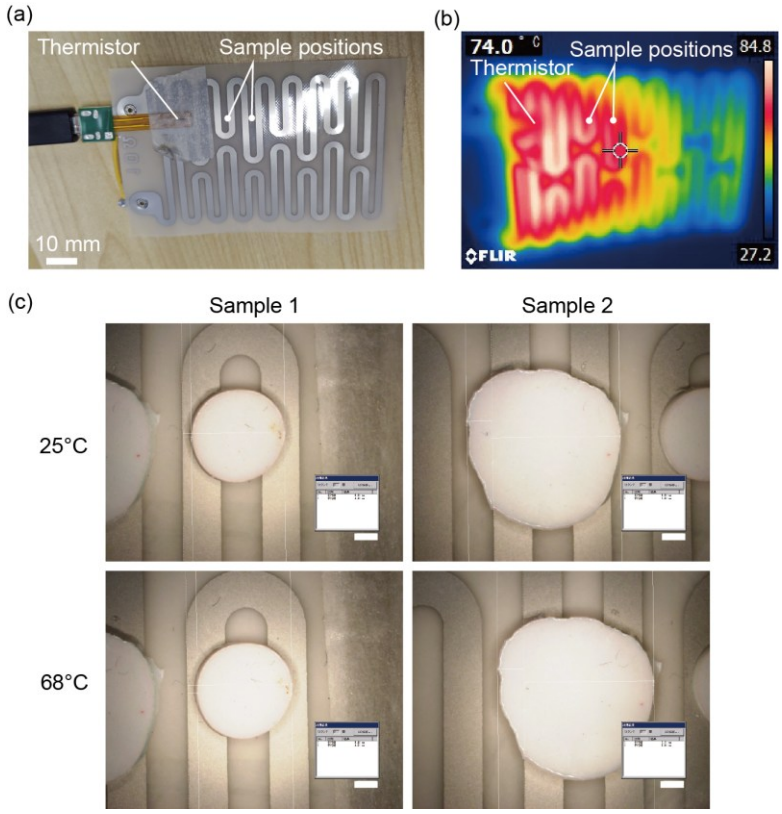

Figure 3.11 Deformation measurements during a temperature increase. (a) A film heater to increase the temperature. (b) The temperature distribution when the thermistor showed 68°C. The temperature at the sample positions were close to the temperature at the thermistor position. (c) Deformation of the silica-PEGPEA polymer by increasing temperature. Scale bar = 1 mm.

thermography (ETS320, Teledyne FLIR LLC). The temperature at the thermistor position and the sample positions were close, as shown by red (Figure 3.11 (b)). The film heater had approximately a 10°C temperature distribution near the sample positions. This effect is discussed after the calculation of the thermal deformation. The dimensions of the polymer were measured at two positions: horizontal dimension from top view and horizontal dimension from side view. The measured positions were selected because relatively large dimensions, unlike thickness, were expected to provide a higher accuracy of the dimension measurement. The result of the dimension measurement (Figure 3.11 (c)) showed that the

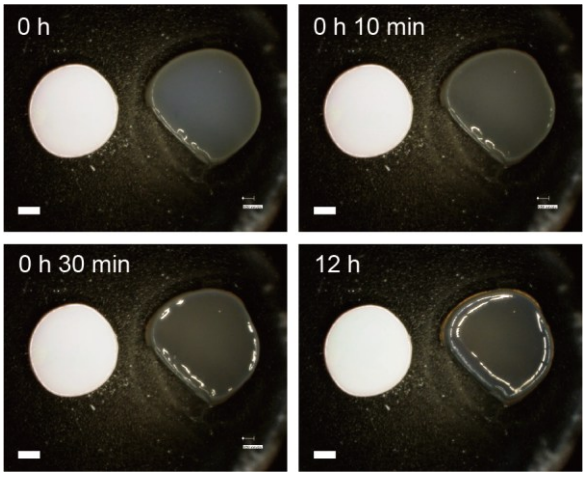

Figure 3.12 Deformation of polymers by evaporation. Left: silica-PEGPEA polymer, right: silica-AAm (acrylamide) hydrogel. Scale bar = 1 mm. The right sample shrunk in first 30 min. with a concaved surface. The left sample looked no shrinkage.

silica-PEGPEA polymer expanded by +1.4% (average of 2 positions in 2 samples) at a 43°C temperature increase. The coefficient of linear thermal expansion was calculated as 3.1×10^{-4} K^{-1}. This value was close to the value of PDMS, 3×10^{-4} K^{-1} [55], suggesting that the silica-PEGPEA polymer had a reasonable thermal expansion coefficient. Here, the temperature distribution (~10°C) had an influence on the coefficient of linear thermal expansion as suggested above. However, the deformation ratio of the polymer was small (+0.31% in +10°C) to increase the reflective wavelength on the polymer, according to Equation (2.8). Strictly, the wavelength on the polymer is expected to be increased by +0.31% in +10°C. Thus, these results suggest that the silica-PEGPEA structural color polymer is relatively stable with temperature increase.

3.4.6 Deformation by Evaporation

The fabricated polymer did not contain water in the polymeric matrix unlike hydrogels. To confirm the polymer is not deformed by water evaporation, the dimensions of the silica-PEGPEA polymer and the silica-AAm hydrogel were measured for 12 h in air at room temperature (~23°C) (Figure 3.12). The thickness of both samples was 0.7 mm.

Horizontal and vertical distances were calculated from the coordinates of four specific points for each sample. From the distances, silica-PEGPEA shrunk 0.9-2.2% and silica-AAm shrunk 5.0-6.1% after 12 h. The silica-AAm hydrogel had clearly shrunk, while the silica-PEGPEA shrinkage was not clear due to the measurement errors. It is suggested that this shrinkage in air also influences the reflective wavelength of the structural color. In the visible light range (400 nm-700 nm), 5% of deformation is equivalent to a 20-35 nm wavelength difference, possibly causing color changes. In terms of appearance, the center of the hydrogel became concave after 12 h, while the silica-PEGPEA polymer did not. From these results, it was suggested that the shape stability of the silica-PEGPEA polymer in air is superior to that of the silica-AAm hydrogel because the silica-PEGPEA polymer does not contain water in the polymeric matrix.

3.5 SEM Observation of the Compressed Structural Color Polymer

To understand the polymeric structure in compression, the cross-sectional view of the polymer was observed with SEM. An electrolyte was permeated into the silica-PEGPEA polymer to provide electrical conductivity. To clarify the structure in compression, the electrolyte penetration was used instead of the osmium coating, which has often been used in normal SEM observations. This is because the osmium coating was expected to cause some cracks in the polymer compression. The electrolyte consisted of 1.0 M LiTFSI (lithium bis(trifluoromethane-sulfonyl)imide) in EC (ethylene carbonate) and DMC (dimethyl carbonate) solution. This electrolyte has small evaporation, resulting in successful observation in the vacuum chamber of the SEM. The polymer compression was induced by a screw attached to the observation jig (Figure 3.13 (a)). The measurement area was close to the screw position to decrease the effect of Poisson's ratio, causing expansion toward the vertical direction against the cross-sectional surface. In the SEM observation, the series of particles in ±30° were chosen (Figure 3.13 (b)) to measure the particle distance for vertical and horizontal directions, caused by the compression. In the following measurement, 20 series of particles were chosen.

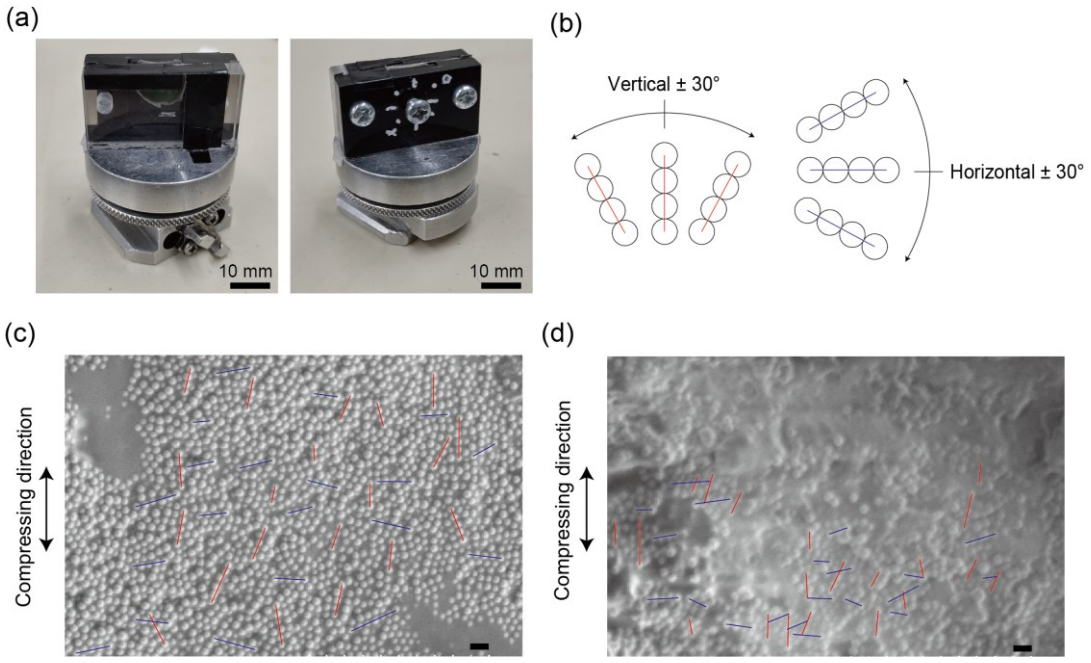

Figure 3.13 (a) The compression jig for the structural color polymer on the SEM table. The screw in the center was for the compression. (b) The rule of the measurement of the particle distances. First, more than two aligned particles in vertical or horizontal direction ±30° range were chosen. Next, the dimensions were divided by ((the number of the particles) - 1). The red lines mean the "vertical" particles, while the blue lines mean the "horizontal" particles. (c) The cross-sectional view of the structural color polymer without compression. The measured particles are shown by the red lines and the blue lines explained in Fig. 3.10 (b). Scale bar = 500 nm. (d) The cross-sectional view of the structural color polymer in compression. Scale bar = 500 nm.

Before the polymer compression (Figure 3.13 (c)), it was observed that the silica nanoparticles were aligned in the polymer. During the polymer compression (Figure 3.13 (d)), the particles were less observed because the electrolyte possibly leaked out from the surface. The polymer compression was 0.25 mm; the polymer thickness was changed from 0.70 mm to 0.45 mm. The measurement result (Table 3.1 and Figure 3.14) showed that there was no significant difference between the particle distances of the initial and compressed polymer. The average of the particle distances in the vertical direction (the compressing direction) had

changed from 226.3 ± 8.4 to 234.3 ± 14.4 nm (±s.d.). This result suggested that the polymer on the surface of the particles rarely deformed. The defects of the particles might decrease. However, the leaked electrolyte caused difficulty in observing the particles. In addition, the effect of the deformation vertical to the cut surface was not completely decreased, possibly causing less compressive deformation. As suggested above, the SEM observation of the compressed silica-PEGPEA polymer was still difficult due to the leaked electrolyte during polymer compression. More improvement of the SEM observation method could reveal the structure of the compressed silica-PEGPEA polymer.

If the silica particles move in a horizontal direction by vertical compression of the polymer, the displacement is expected to follow Poisson's ratio. From Sec. 3.4.4, Poisson's ratio of the silica-PEGPEA polymer was around 0.31. From the definition of Poisson's ratio (Equation (2.13)), the horizontal strain will be 0.31 times the vertical strain. When the vertical strain is 0.1, the horizontal strain is 0.031, resulting in a +3.1% increase of the reflective wavelength on the structural color polymer. The view angle is generally not horizontal. Thus, the wavelength increase is expected to be smaller than 3.1%.

(n = 20)	Average particle distance (± s.d.) [nm] Vertical	Horizontal
Initial (0 mm)	226.3 ± 8.4	230.1 ± 17.3
In compression (0.25 mm)	234.3 ± 14.4	234.2 ± 20.3

Table 3.1 The measurement result of the particle distances before/after compression. The vertical direction means the compressing direction. This time, no significant differences were observed.

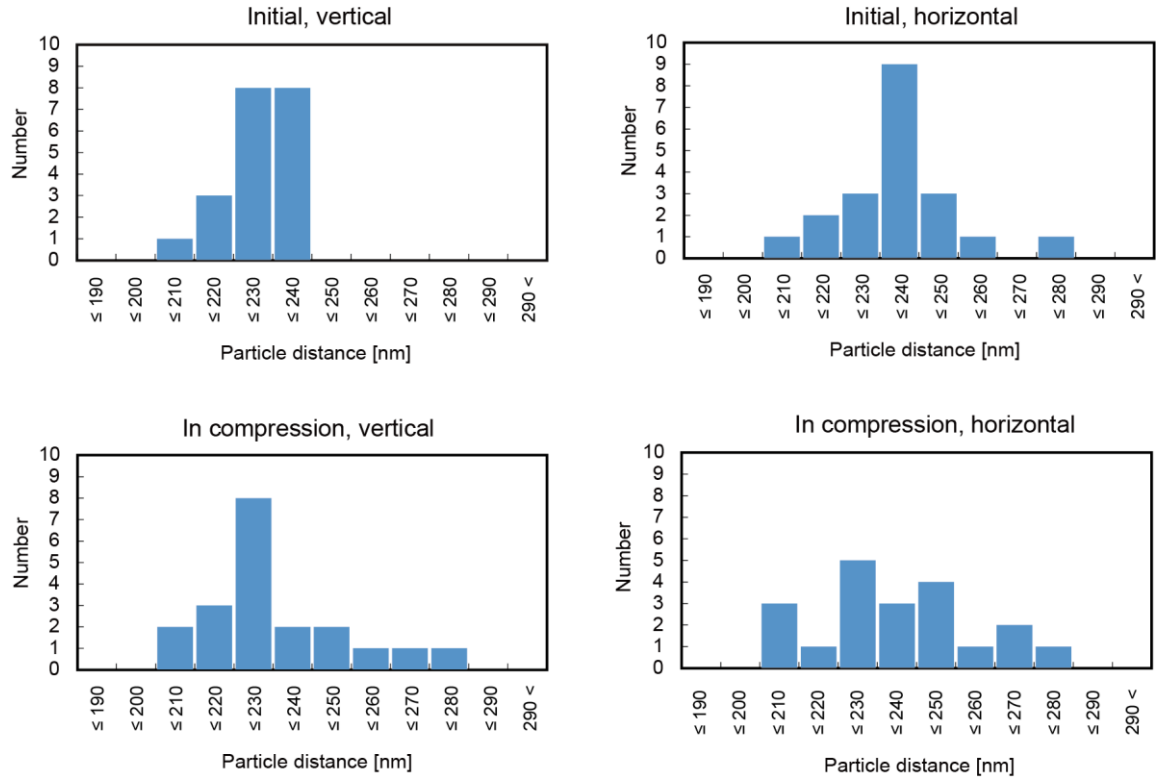

Figure 3.14 Histograms of the particle distances before/after compression (n = 20).

3.6 Angular Dependence on the Structural Color Polymer

To estimate the particle structure with the optical method, the reflective spectra of the structural color polymer with various angles were measured. The spectra were measured with a spectrometer (USB2000+). The probe of the spectrometer was tilted to change the measurement angle θ. This time, the light path was in coaxial direction (like left of Figure 3.15(a)) due to the ease of measurement: the spectra derived from the particle distance in coaxial direction should be the same as in the reflective direction, as shown in Figure 3.15 (a). The intensity in the coaxial direction would be lower than in the reflective direction because the light in the coaxial direction was scattered, while the spectral shape would be similar. Next, the spectra measurement was conducted. When multiple values were obtained for the peak wavelength, the average of these values was considered the true peak wavelength. The peak wavelength λ_θ would be proportional to the particle distance d_θ in the measurement angle θ, estimated from Bragg's law (Equation (2.1)).

The result showed that the peak wavelength λ_θ increased when the measurement angle θ was decreased (Figure 3.15(b) and Table 3.2). The increase of the peak wavelength at a 30° angle was +4.4% against the peak wavelength at a 90° angle. This value was not explained by the particle-layer assumption (Fig. 3.15(c)) or face-centered cubic (fcc) structure assumption (Figure 3.15(d) and Table 3.2). If those assumptions were true, the increase of the peak wavelength should be much larger. Therefore, it seemed that the particle structure was almost amorphous (random) and the particle distance in the vertical direction tended to be smaller than the particle distances at smaller angles (Figure 3.15(e)).

The fact that the plate-shaped structural color polymer had a small angular dependency was a different result from the sphere-shaped structural color polymer, suggesting no angular dependency [33]. The interface stress between the glass and silica particles or compressive stress in the polymer forming process might affect the particle structure (Figure 3.15(f)).

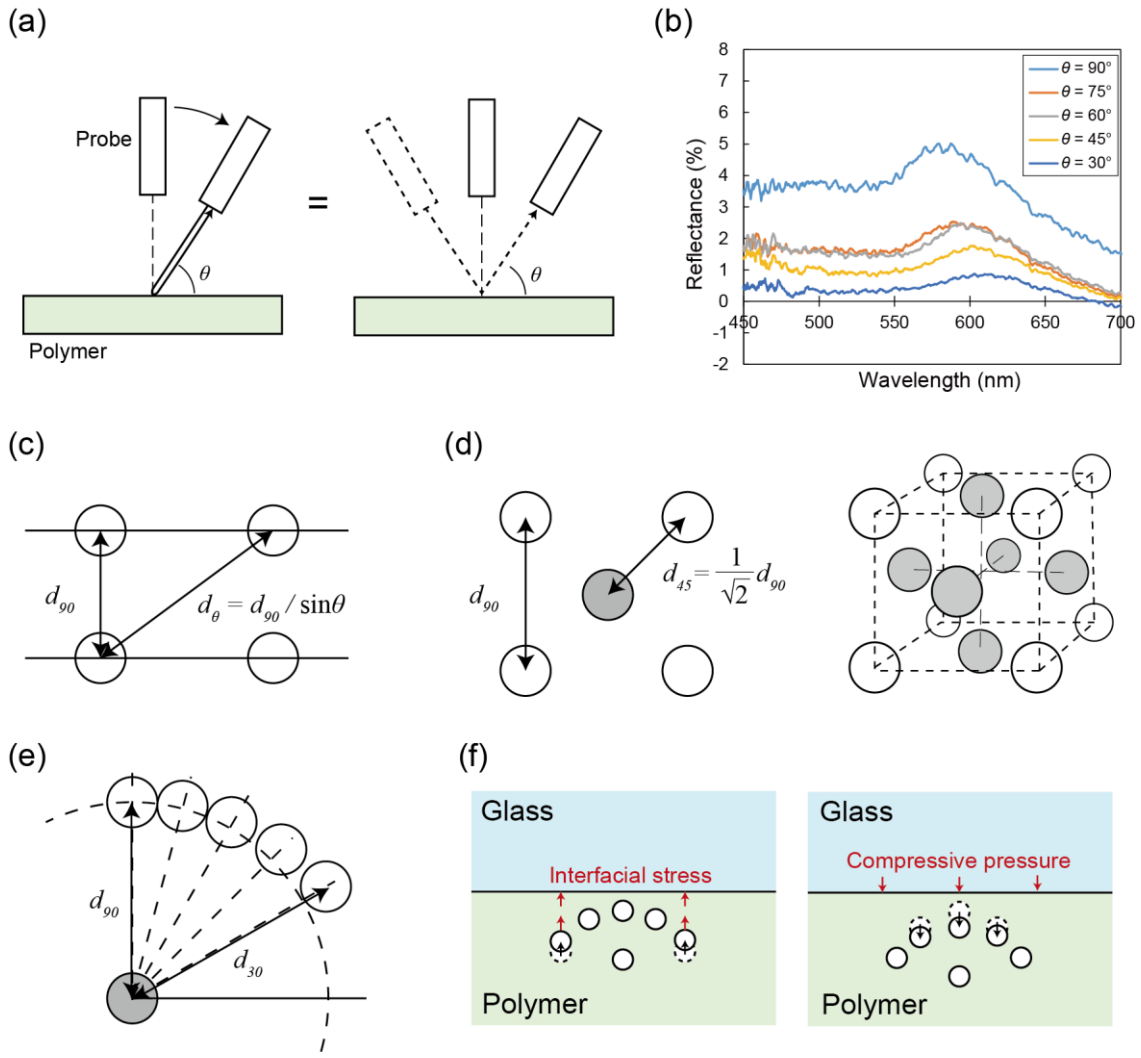

Figure 3.15 The particle structure estimation with optical spectra measurements. (a) The definition of the measurement angle θ. (b) Results of the reflective spectra measurement. (c) A particle structure assumption that the particles were aligned in layers. The particle distance d_θ would be proportional to the reflective wavelength. (d) A particle structure assumption that the particles formed fcc (face-centered cubic) structure. (e) The estimated particle structure from the spectra measurements. The structure was almost amorphous and vertically compressed. (f) The estimated theories to induce the particle structure. The interfacial stress or compressive pressure possibly led to the vertically compressed structure.

	Peak wavelength (nm)				Ratio (-)	Assumption of peak wavelength (nm)		
θ (°)	1	2	3	Ave. λ_θ	$\lambda_\theta / \lambda_{90}$	Layer $\lambda_{90} / \sin\theta$	Fcc $1/\sqrt{2}\,\lambda_{90}$	Fcc $1/\sqrt{2}\,\lambda_{45}$
90	579.546	587.307		583.43		583.43		425.36
75	589.068			589.07	1.010	604.01		
60	593.994			593.99	1.018	673.68		
45	600.667	602.421		601.54	1.031	825.09	412.54	
30	603.122	610.124	613.968	609.07	1.044	1166.85		

Table 3.2 The result of peak wavelength measurements and assumptions of the peak wavelength with specific structures shown in Figure 3.15(c)-(d).

3.7 Conclusion

This chapter describes the fabrication process and characteristics of the silica-PEGPEA structural color polymer.

With the fabrication process, the silica nanoparticles made a disordered and correlated amorphous structure. This structure resulted in a small angle dependence on the reflected color. This feature is preferred over experimental devices that do not require high precision. In addition, the described fabrication process is easier than metal mesh or manually aligned particles. In conclusion, those two features – flexibility of design and easier fabrication – are expected to facilitate the development of structural color polymers.

CHAPTER 4.
IN-LINE LIQUID MONITORING SYSTEM

4.1 Introduction

In this chapter, an in-line microliter liquid color monitoring sensor is proposed.

Monitoring liquid conditions is a critical technology for chemical reactions in scientific research and for the stabilization of industrial production [59–61]. In such a monitoring system, many parameters related to liquids have been strictly measured and controlled, such as pH, temperature, and viscosity. Especially, liquid color is one of the most essential parameters in the monitoring system [61]. The liquid color change indicates the liquid conditions directly, such as changes in molecular structure or concentration. Thus, automatic color monitoring systems have been used in the production lines. Among the color monitoring systems, the in-line type of liquid color sensors is a useful system [62]. “In-line” means “in the middle of pipelines,” resulting in that the in-line sensors do not need manual sampling. Generally, the in-line liquid monitoring sensors also use vibration [63,64] or electromagnetic waves [65] as principles, resulting from the useful structure. Furthermore, the in-line color sensors are also expected to be applied to microfluidic devices, including μTAS (Micro Total Analysis System) [66–72]. The in-line method causes no contamination or sample loss in microfluidic systems. Therefore, the in-line sensors have an essential role in monitoring micro- or nano-litter samples inside the μTAS devices.

To achieve microliter liquid color monitoring, miniaturization of the in-line color

sensors to a millimeter size is required. To date, two major approaches for miniaturization of the in-line color sensors have been reported: (1) combination of LEDs (light emitting diodes) and PDs (photodiodes), and (2) micro-spectrometers. The smaller system in the two methods is (1) the LED/PD system [66,67]. One of the LED/PD systems [67] was ~20 mm in size. However, most LEDs have only a single wavelength (color). Thus, multiple pairs of LEDs/PDs for different wavelengths should be aligned to detect the liquid color changes. This alignment causes a size increase as a result. On the other hand, (2) micro-spectrometers have prisms or gratings that are a mechanism to change the light wavelength continuously [73]. This mechanism realizes liquid spectra analyses and color change detection. However, the spectrometers tend to be large because the prisms or gratings use the difference in diffraction angles for irradiation wavelength adjustment, requiring long light paths. To decrease the size of spectrometers, some mechanisms have been reported. One of the mechanisms is that the measurement point and the spectrometers are separated – an optical fiber probe is inserted in the pipeline [68]. The probe downsizes the parts around a pipe, while the whole size is large. Also, concave diffraction gratings have a small body [73]. The grating changes the reflection direction according to the wavelength, and the linear image sensor measures the light irradiance of each wavelength. Therefore, the obtained spectral data is theoretically discrete. Therefore, despite these efforts, the miniaturization of the whole spectrometer system is still challenging. As shown above, both the LED/PD and spectrometers have issues in realizing the in-line microliter liquid color sensors.

Here, an in-line microliter liquid color sensor with an optical filter of a structural color polymer is presented (Figure 4.1(a)). This sensor is (2) the spectrometer type. The structural color polymer is made of aligned silica (SiO_2) nanoparticles and PEGPEA, displaying a bright color due to Bragg's reflection. The sample liquid passes through a glass capillary in the device, resulting in color monitoring without contamination or sample loss (Figure 4.1(b)). The mechanism is as follows (Figure 4.1(c)): A sunlight-type white LED irradiates the light onto the filter. Then, the filter reflects a specific wavelength due to Bragg's reflection. Next, the reflected light transmits the sample liquid in the 1 × 1 mm glass capillary. The transmitted light is detected with a single PD. The reflective wavelength on the color

filter is continuously tunable by filter compression, enabling a scan of the liquid spectrum with a single PD (Figure 4.1(d)). Moreover, the light path in the presented device is fixed during the compression of the color filter. This structure makes it possible to omit the optical fiber probe. For these two reasons, the filter made of the structural color polymer saves the whole size compared to the typical LED/PD systems or spectrometers. In this chapter, it is shown that the characteristics of the optical filter using the structural color polymer and the sensor availability for color, concentration, and pH measurements.

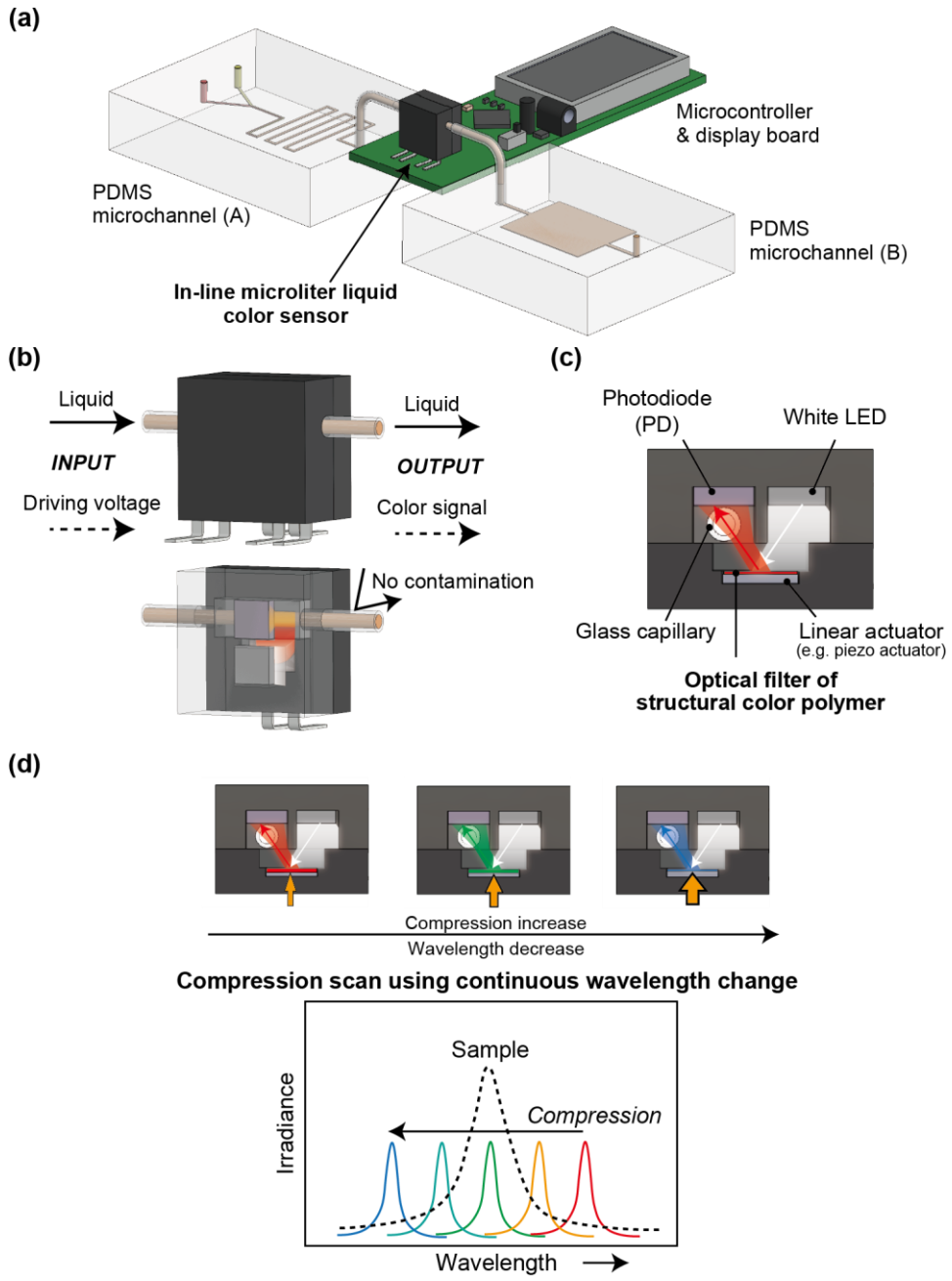

Figure 4.1 Concept of in-line microliter liquid color sensor. (a) An example of in-line liquid sensing system. Combined with microchannels or microchambers, the system detects the liquid color without sampling. (b) Input and output signal of the presented in-line sensor. (c) Cross-sectional diagram of the in-line sensor. (d) Mechanism of the in-line color sensor.

4.2 Mechanisms of the In-Line Sensor

In this section, principles of the in-line liquid color sensor are explained, excluding the principles of the structural color polymer. After that, the mechanical structure of the sensor is described.

4.2.1 Principle of Light Transmission

The symbols used in this chapter are as follows.

I_0	irradiance before transmission [W/m^2]
I	irradiance after transmission [W/m^2]
ε	molar absorption coefficient [L/mol·m]
C	concentration [mol/L]
L	capillary width [m]
λ	wavelength [nm]
δ	compression [m]
V_{out}	output voltage of photodiode [V]
V_{w}	output voltage of photodiode in $C = 0$ liquid [V]

The reflected light on the structural color polymer transmits the sample liquid in a glass capillary. The light irradiance after transmission, I, is shown as Lambert-Beer-Bouguer's law:

$$I = I_0 e^{-\epsilon CL} \tag{4.1}$$

(Figure 4.2). This equation is transformed to

$$I/I_0 = e^{-\epsilon CL}. \tag{4.2}$$

Here, ε is constant when the liquid composition is the same. L in the presented in-line sensor is also constant. Thus, I / I_0 in each wavelength λ is decreased according to an increase of concentration C. This relation was examined in the experimental section.

In color detection, the relation of Equation (4.2) is applied in each wavelength. In

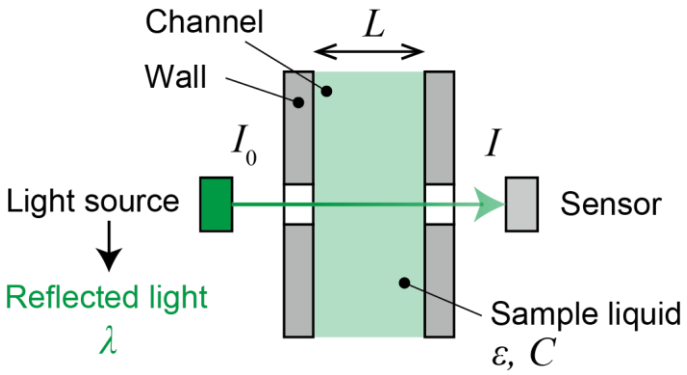

Figure 4.2 Principles of the light transmission. In the in-line sensor, the reflective light on the structural color polymer behaved as a light source. Similarly, the photodiode was a sensor, and the glass capillary was a channel.

reality, the input spectrum has a width as shown in Figure 4.3 (a). To simplify the calculations, the relationship at the peak of the reflective spectrum is considered. I_0 is the irradiance peak of the spectrum reflected on the optical filter, while I is the irradiance after liquid transmission. Depending on the compression of the filter, the input spectrum moves to the shorter wavelength (Equation (2.1)). For example, the filter displays green, and the liquid sample is blue initially (Figure 4.3 (a): left graph). By filter compression, the wavelength at the irradiance peak of the input spectrum comes close to the wavelength at the irradiance peak of the liquid transmission spectrum. Then, the irradiance measured with the PD becomes a higher voltage. The measured value reaches a maximum when the two spectra overlap. On the contrary, the red liquid is considered, for example. By filter compression, the input spectrum is apart from the liquid transmission spectrum. This causes a decrease in PD output voltage. In summary, a comparison between the PD voltage trends results in the estimation of the liquid transmission spectrum (Figure 4.3 (a): right graph). In the experimental section, the voltage trend is evaluated based on the slope in a linear approximation to simplify the calculations.

Similarly, concentration measurement is considered (Figure 4.3 (b)). The filter displays green, and the liquid color is blue. From Equation (4.1), an increase in liquid concentration decreases the irradiance of the liquid transmission spectrum. This is

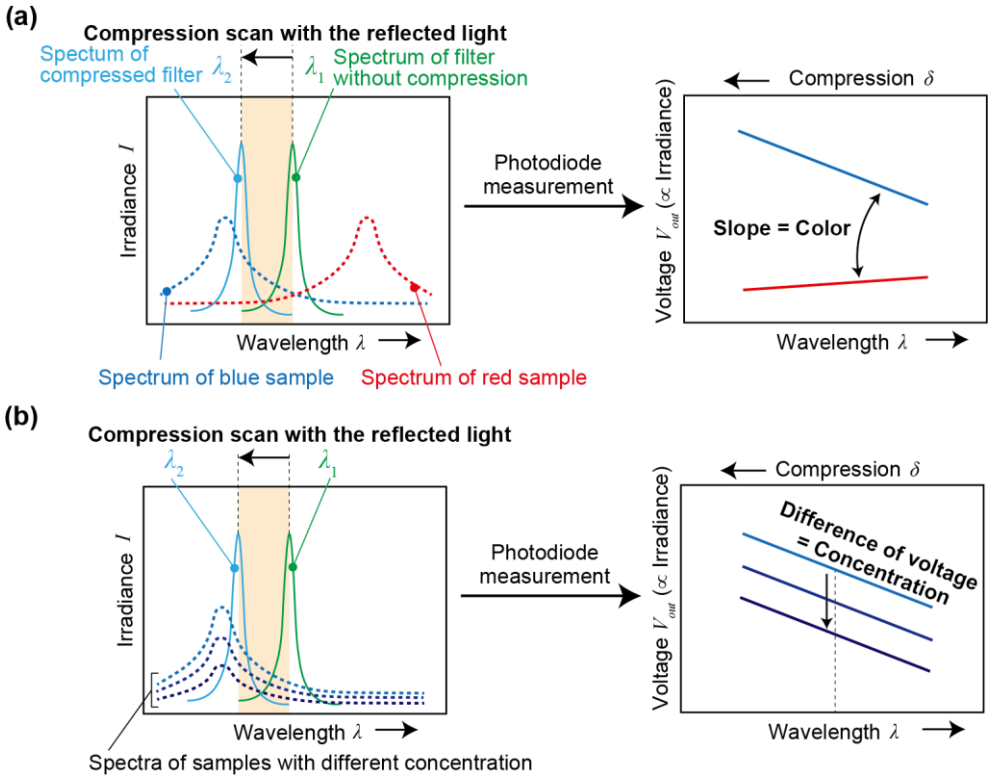

Figure 4.3 Principles of the in-line color sensor. (a) Principle of the sensor in color detection. The slopes in λ-V_{out} graph shows the wavelength at the peak of the sample spectrum. (b) Principle of the sensor in concentration detection. The values in λ-V_{out} graph with the same wavelength shows irradiance at the peak of the sample spectrum.

independent of the wavelength and the filter compression. Thus, when the concentration is changed, the value of the PD output voltage is decreased while the trend (slope) is the same. From this, the concentration of the liquid sample is estimated.

The summary of the above calculations is shown in the flow chart (Figure 4.4). The irradiation spectrum of the LED is I_{LED} (λ). The specific wavelength λ_1 is reflected on the filter with I_0 (λ_1) irradiance according to Equation (2.1). The wavelength λ_1 is changed by the filter compression δ_1 according to Equation (2.4). The irradiance I_0 (λ_1) decreases to I (λ_1) after the transmission through the sample liquid according to Equation (4.1). The PD measures the irradiance I (λ_1), outputting the output voltage V_{out} (λ_1). V_{out} and I are proportional in the prepared PD. The above process is conducted at each wavelength ($\lambda = \lambda_1$,

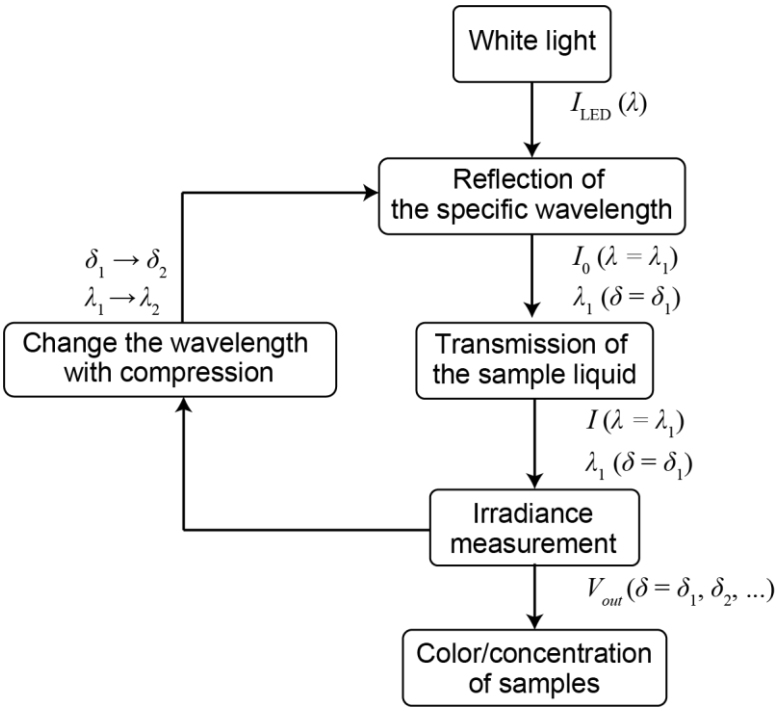

Figure 4.4 Flow chart of the presented in-line microliter liquid color sensor. The reflective wavelength is selected by compression of the structural color polymer. The irradiance at each wavelength is measured with output voltage of the photodiode. As the compression is changed, each irradiance at each wavelength is recorded.

λ_2, …) to obtain plots. The λ_1 is shifted to λ_2 by changing the compression from δ_1 to δ_2. V_{out} with the wavelength λ_2 is also measured with the process. With the series of compression and measurement, the output voltage V_{out} ($\delta = \delta_1, \delta_2, \ldots$) is plotted. Note that the V_{out} contains the PD characteristics and should be normalized by V_w, the output voltage in $C = 0$ liquid. This is expressed as

$$V_w \propto I = I_0 \tag{4.3}$$

using Equation (4.1), $C = 0$, and the proportional property of the PD. Finally, the values and the slopes of approximation lines are determined from $V_{out} / V_w (\delta)$. Thus,

$$V_{out}/V_w \propto I/I_0 = e^{-\epsilon CL} \text{ for all } \lambda \tag{4.4}$$

is derived from Equations (4.2) and (4.3). The values and the slopes correspond to the

concentration and the color of the sample liquid.

4.2.2 Design and Mechanical Structure of the In-Line Sensor

A prototype of the in-line liquid color sensor was fabricated to obtain the plots (Figure 4.5 (a)-(b)). The prototype mainly consisted of top, middle, and bottom bodies made of black acrylic to prevent ambient light. The entire size was 40 × 40 × 15 mm (Figure 4.5 (c)). A white LED (sunlight type, ENB01-NHSD7-F1, Toyoda Gosei) and a PD (S7183, Hamamatsu Photonics) were set on the top body. A square glass capillary (internal dimension was 1 × 1 mm) was placed on the middle body. A cover glass, a movable stage, and the fabricated filter were sandwiched between the middle and bottom bodies. The stage was moved by a screw, resulting in the filter compression. The pitch of the screw was 0.5 mm. The compression stroke was calculated from the pitch and rotation angles. In the following experiments, a 0-1/2 rotation was used to prevent breaking the cover glass. The screw was manually rotated to match the angle scale written on the bottom body. All bodies were fixed by four screws.

The optical design is as follows. As already explained, the light from the LED reflected on the filter, transmitted through the glass capillary, and reached the PD (Figure 4.5 (c)-(d)). The incidence angle was set to 60°. The optical path was limited by the black acrylic body (Figure 4.5 (d)). The filter of the structural color polymer had less angle dependence, allowing relaxation of the angle condition. Thus, the optical slit was omitted in the sensor. The optical path remained unchanged during the filter compression, as the top surface of the structural color polymer was fixed by the cover glass.

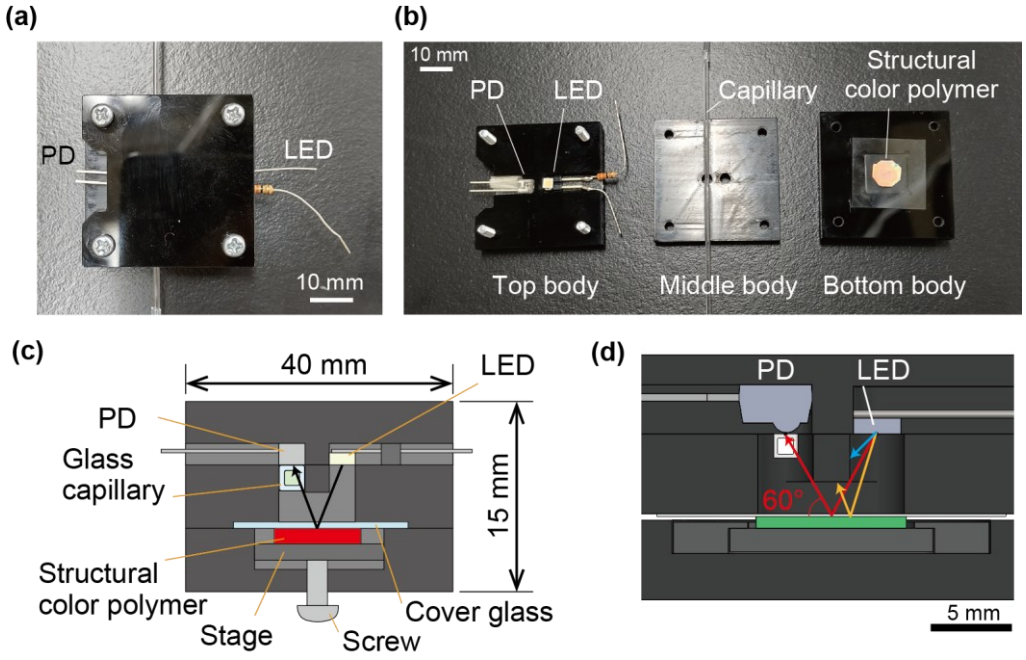

Figure 4.5 Design of the in-line color sensor. (a) Fabricated prototype of the in-line microliter liquid color sensor. (b) Disassembled prototype. The structural color polymer was placed in the bottom body. (c) Cross-sectional view of the proposed sensor. The size was 40 × 40 × 15 mm. (d) Optical path design. The light except reflective angle = 60° was absorbed by the black body.

4.3 Experimental Methods

4.3.1 Evaluation of the Structural Color Polymer for In-Line Sensor

Three sheets of structural color polymer were fabricated 0.70 mm thick (Figure 4.6 (a)) according to the process shown in Section 3.2. Then, the polymer was observed with an SEM (SU-70, Hitachi High-tech Corp.). The fabricated polymer did not contain water, enabling this SEM observation. The polymer was osmium-coated to add electrical conductivity. The SEM image of the polymer (Figure 4.6 (b)) clearly showed that the silica nanoparticles were aligned in the polymer.

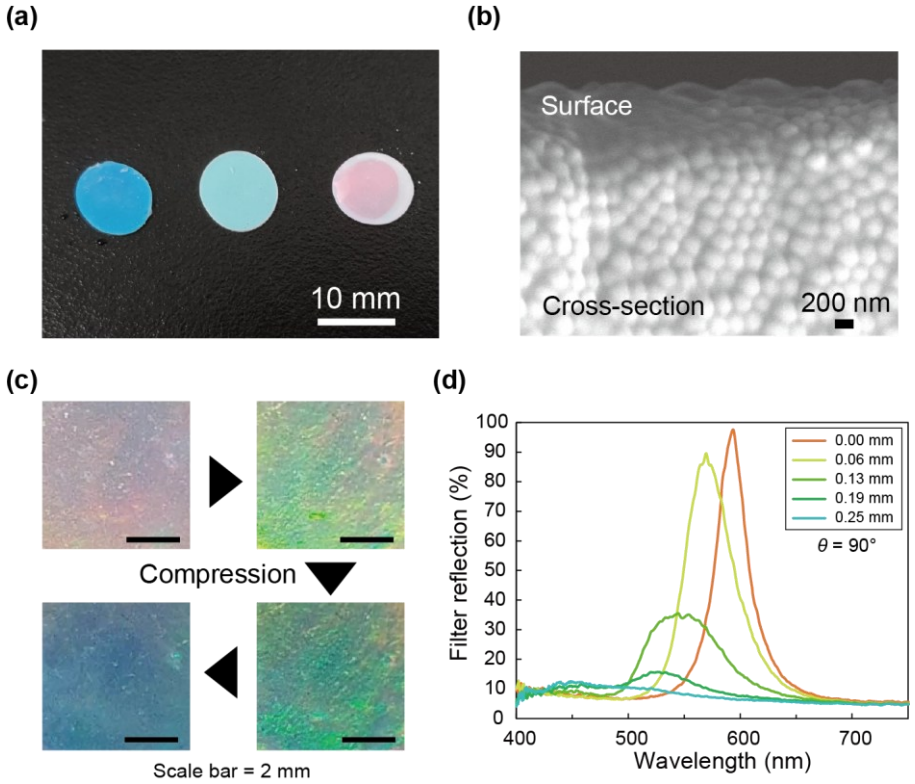

Figure 4.6 (a) Three colors of the fabricated structural color polymer. (b) SEM image of the cross-sectional surface of the structural color polymer. (c) Color change of the structural color polymer in compression. The reflective wavelength became shorter, causing the color change from red to blue. (d) Spectrum change of the structural color polymer in compression. The irradiation angle was 90°.

The compression of the polymer showed the color change from red to blue (Figure 4.6 (c)). This color change was measured with a spectrometer (USB2000+, Ocean Optics). The angles of incidence and reflection were both 90°. Then, the irradiance peak of the reflective spectrum was changed from 590 nm to 450 nm by 0.25 mm compression (Figure 4.6 (d)). In addition, the reflection at the spectrum peaks decreased depending on the compression.

4.3.2 Available Range of the In-Line Sensor

To grasp the scan range of the sensor, the spectrum change of the filter (initial color was red) was measured after the filter was assembled in the prototype sensor (Figure 4.7(a)-

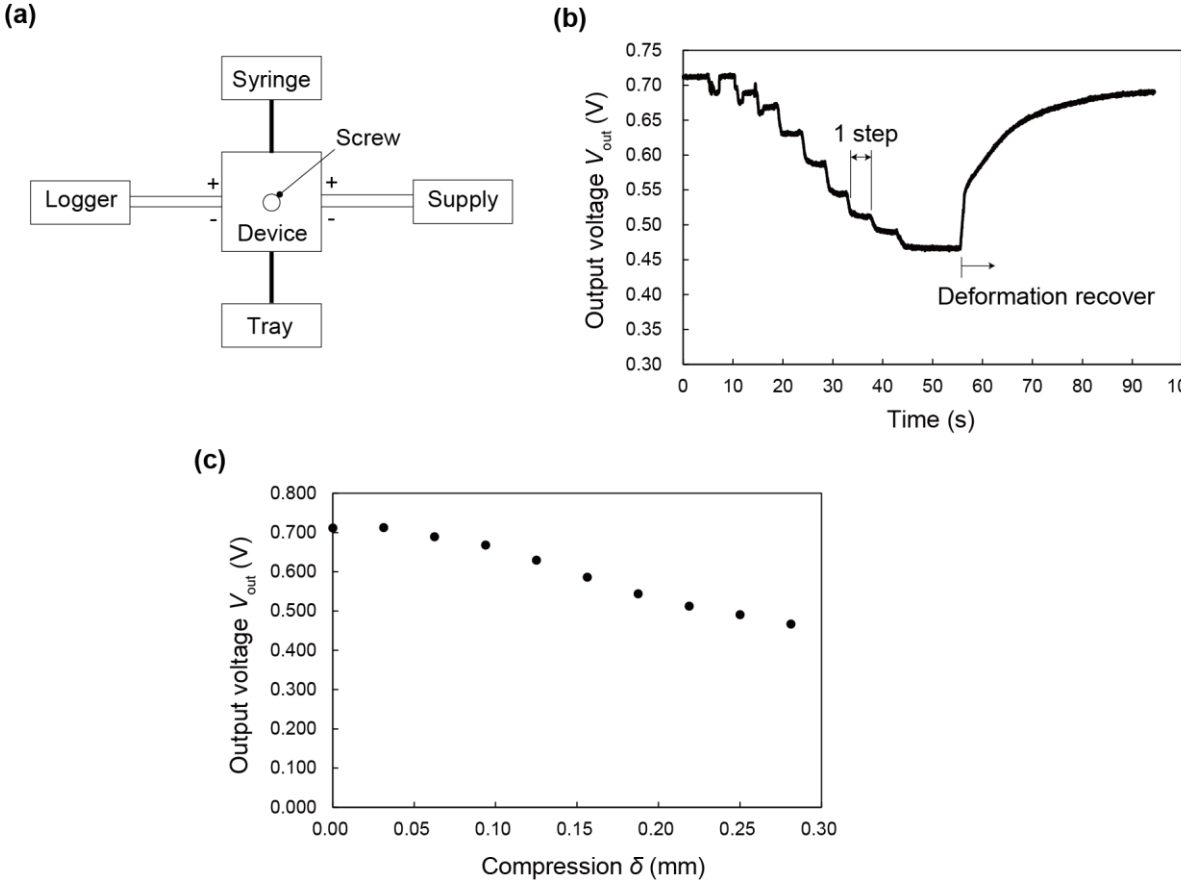

Figure 4.7 Availability evaluation method of the in-line color sensor. (a) Connection of the in-line sensor. (b) An example of a spectrum measurement result. To obtain a plot in each compression step, the waiting time ~5s was set. (c) Output voltage in each compression step.

(c)). The assembled sensor had the LED and the PD. Thus, the LED was connected to a power supply (voltage: 5 V, current: 60 mA) and a 33 Ω resistor, while the PD was connected to a data logger (DL350, Yokogawa Electric Co.) (Figure 4.7(a)). One end of the glass capillary was connected to a 1 mL syringe with a silicone tube. The other end had another silicone tube going to a tray. In the following experiments, the sample liquid was in a static state. The sensor would work theoretically even in a situation where the liquid moves along the capillary.

After the connection, measurements with deionized (DI) water and colored water were conducted. The following measurement process was common in the measurement of

water or a sample liquid. To initialize the glass capillary, DI water was first infused into the capillary. Then, the capillary was washed by pumping water back and forth with the syringe. After that, the sample liquid was infused into the glass capillary. The size of the glass capillary was 1 × 1 × 100 mm = 100 μL. Because water droplets often remained in the capillary, more than 100 μL of the sample was injected to push out the low-concentration portion into the tray. The actual measurement process was as follows: First, the filter in the sensor was compressed by 1/16 turn of the 0.5-mm pitch screw (approx. 0.031 mm) manually (Figure 4.7 (b)). Then, I waited for 5 s as a single measurement step. After that, the compression step was repeated until 0.25 mm (strain $\leq$ 0.33). The output voltage of the PD was recorded during all compression steps. After all steps were finished, I waited for 2 – 3 min until the deformation of the polymer had recovered (the curve in Figure 4.7 (b), the phenomenon was also explained in Section 3.4). In fact, the recovery was also seen with the output voltage in real-time, because the irradiance decreased in the polymer compression (see Figure 4.6 (d)). After the deformation monitored with the output voltage was recovered, the next measurement sequence was conducted. After all sequences of the measurements, the plots of the output voltage were calculated (Figure 4.7 (c)). Each compression step had approximately 5 s of voltage data. From the data, a stable 100-ms interval was selected and averaged. This measurement process eliminated the effect of the stress relaxation (Figure 3.3 (b)). The compression sequence was conducted three times.

According to the above measurement process, DI water was measured with the PD and the spectrometer (USB2000+) probe. Note that the PD was replaced with the spectrometer when spectra were measured. The red polymeric filter was used. The result of the spectra measurement (Figure 4.8 (a)) showed that the wavelength at the spectrum peaks decreased depending on the filter compression increase. This suggested that Bragg's reflection (Equation (2.1)) worked properly on the filter.

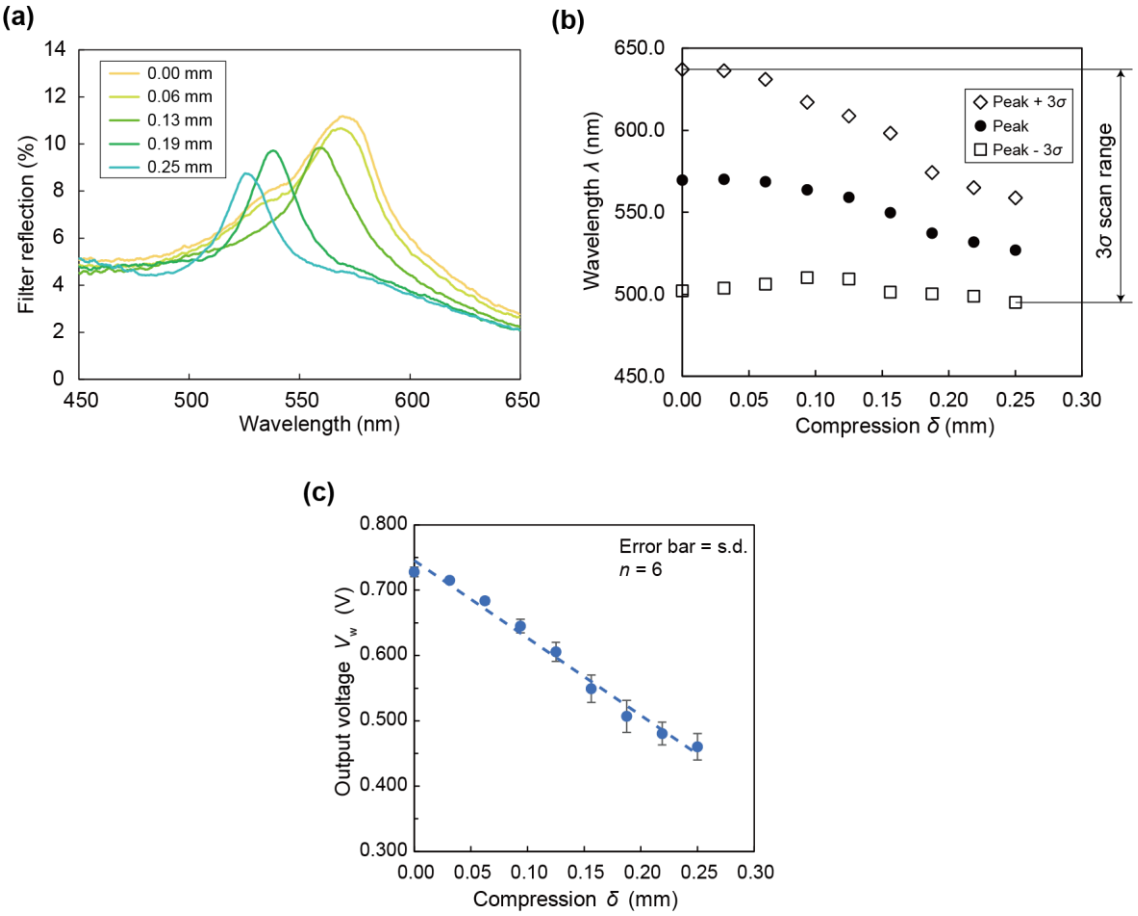

Figure 4.8 (a) Spectrum change in the in-line sensor depending on the filter compression. (b) The spectrum peak and $\pm 3\sigma$ (σ: standard deviation) wavelength change in the compression. (c) Calibration of the PD with DI water sample.

The available range of the sensor, called the "scan range," was calculated by the wavelength shift in the compression range. Then, the scan range of the sensor was 526.8 – 570.0 nm (peak) (Figure 4.8 (b)). The initial peak was 570.0 nm, possibly derived from Equation (2.1) at $\lambda = 596$ nm and $\theta = 60°$, even though the angle dependence was decreased. This range of 526.8 – 570.0 nm corresponds to green to yellow. Thus, green and yellow liquids were prepared in the following experiments.

More strictly, the reflected spectra had widths calculated from FWHM (Full width at half maximum). The FWHM was calculated from

$$(\text{Reflection}) = \frac{(\text{Maximum reflection}) - (\text{Minimum reflection})}{2}$$
$$\text{when } \lambda = \lambda_{peak} \pm \frac{FWHM}{2}. \tag{4.5}$$

The FWHMs shown in Figure 4.8(a) were 40 – 80 nm. Thus, the PD had the possibility to respond to a wider wavelength range. Here, the white plots in Figure 4.8 (b) showed the 3σ range of the spectra calculated from FWHMs. The standard deviation σ was calculated from

$$FWHM = 2\sigma\sqrt{2\ln 2}. \tag{4.6}$$

From this spectra range, 3σ scan range that means the possible responding range was calculated as 494 – 640 nm. This range corresponds to blue to red.

4.3.3 Calibration of the In-Line Sensor

As already said in the previous section, the irradiance peaks of the spectra decreased as the filter compression increased (Figure 4.8 (a)-(b)). It was expected that this irradiance decrease would cause a decrease in output voltage at the PD. The graph (Figure 4.8 (c)) also showed that the output voltage from the PD in water measurement (V_w) decreased linearly when the compression (δ) increased. Moreover, this decreasing trend also contained the optical properties of the PD. Thus, the voltage decrease was normalized in the following experiments as a calibration.

4.3.4 Preparation of Dyed Water

Yellow food dye (Kyoritsu Foods Co., Ltd.) and green food dye (Watashi-no Daidokoro Co., Ltd.) were used for dying water. The yellow dye contained 86% dextrin and 14% tartrazine. The green dye contained 75% gardenia yellow, 20% gardenia blue, and 5% dextrin. The green dye contained blue and yellow dyes, probably causing a similar spectrum

to the yellow spectrum around 570-590 nm. The dye powder was weighed and then mixed with water to obtain the required concentration.

4.4 Experimental Results

4.4.1 Color Detection with the In-Line Sensor

Two colors of dyed water (yellow and green) were measured with the in-line microliter color sensor to evaluate the color detectability of the sensor. 5.0 mg/mL of yellow and green dyed water for liquid samples was prepared (Figure 4.9 (a)).

First, the actual spectra of liquid samples were measured. The spectra of liquid samples were measured with a spectrometer (USB2000 +). It was shown that the major difference between yellow and green samples was around 500 nm in wavelength (Figure 4.9 (b)). Next, the expected output values with the PD were calculated to compare with the experimental output values. The irradiance spectra of the yellow and green samples (yellow and green lines in Figure 4.9 (b), $I(\lambda)$) were normalized with the irradiance spectrum of the DI water sample (black line in Figure 4.9 (b), $I_0(\lambda)$). The normalized data are shown in Figure 4.9 (c). Here, In was defined as

$$I_n = I/I_0. \tag{4.7}$$

For easy comparison, the slopes of each data were calculated by linear approximation in the 3σ scan range (red broken line in Figure 4.9 (b)). The calculated slopes were 1.4×10^{-3} nm^{-1} (yellow) and -1.6×10^{-3} nm^{-1} (green), respectively (Figure 4.9 (c)). The slope of the yellow sample was much larger than the slope of the green sample due to the difference of around 500 nm wavelength. More strictly, the convolution of the reflected light on the filter (Figure 4.8 (a)) and the sample spectra (Figure 4.9 (b)) should be conducted. In this experiment, a comparison of the difference between the slopes was focused on. The curve shapes of the normalized spectra were not required for the judgment of the difference.

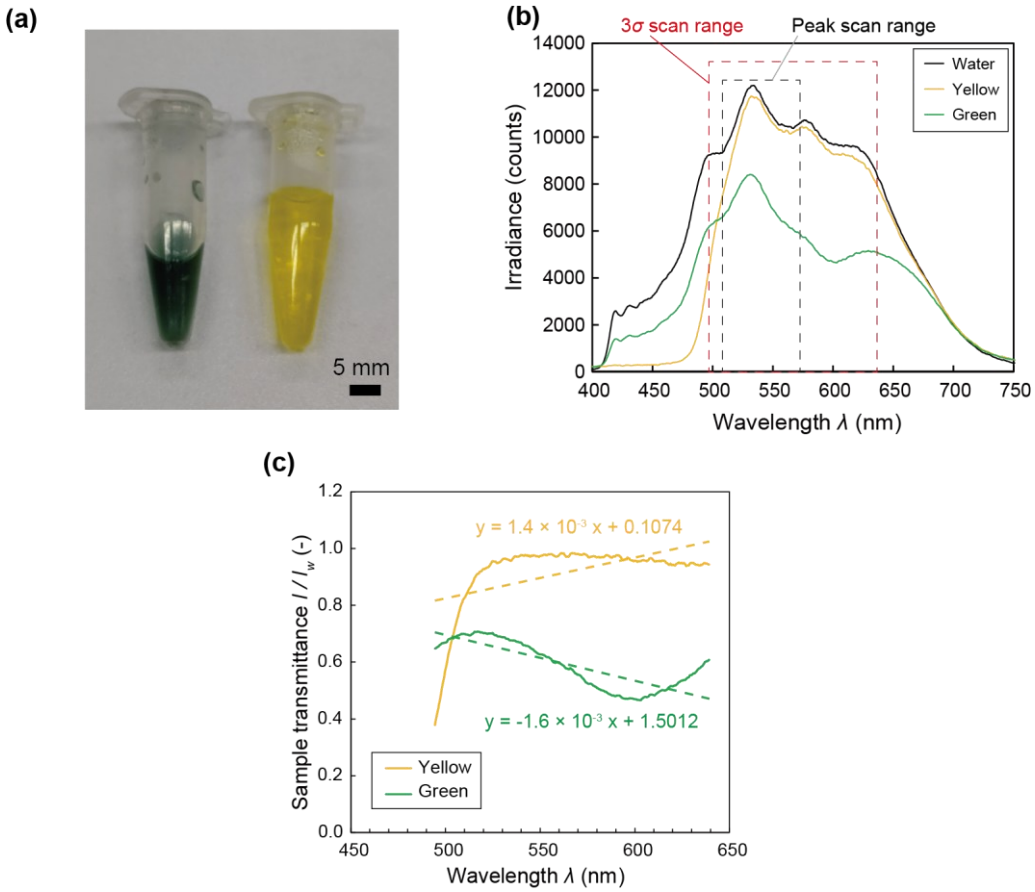

Figure 4.9 (a) The colored water sample. Green and yellow samples were prepared. (b) The spectrum data with the spectrometer. (c) The normalized data of Figure 4.9 (b). The broken lines were the predicted trends: the yellow sample would have larger slope than the green sample.

After the calculation of the expected data, the experimental color measurements with the in-line sensor were conducted (Figure 4.10 (a)-(b)). The result was expressed as the relationship between the normalized output voltage V_n and wavelength λ. Here, V_n was defined as

$$V_n = V_{out}/V_w. \tag{4.8}$$

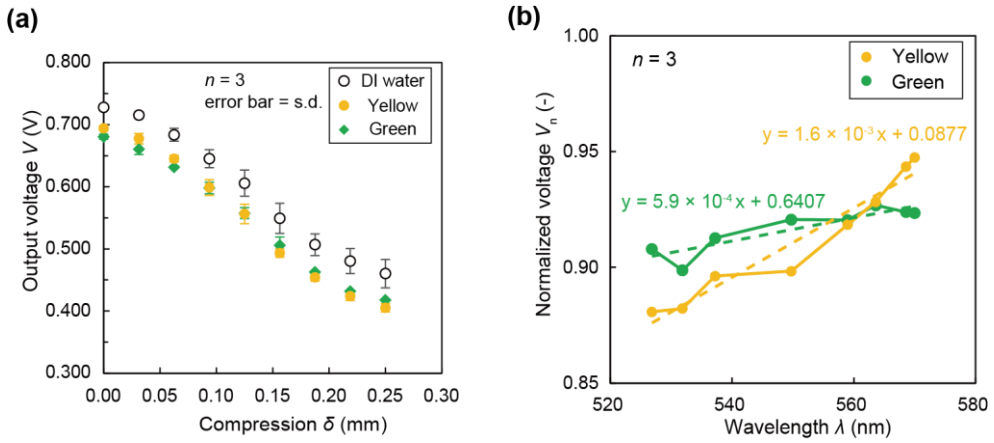

Figure 4.10 The results of the measurements with the in-line sensor. (a) The raw data of the color detection. The graph showed the relationship between the filer compression and the output voltage of the PD. (b) The normalized data of Figure 4.10 (a). The yellow sample had larger slope in the broken line than the green sample. The normal line suggested spectra.

From Equations (4.6), (4.7), and (4.8), it was shown that

$$V_n \propto I_n \quad \text{for all } \lambda, \tag{4.9}$$

enabling comparison between the actual spectrum data and sensor data. First, the output voltage of PD in the sensor (V_{out}) and the compression of the filter (δ) was plotted (Figure 4.10 (a)). Next, V_{out} was normalized by V_w and rewritten as V_n according to Equation (4.8). Wavelength λ was calculated from the relationship shown in Figure 4.7 (b). The result of the spectra measurement (Figure 4.10 (b)) showed that the slope of the yellow sample was 1.6×10^{-3} nm^{-1}. This was much larger than the slope of the green sample, 5.9×10^{-4} nm^{-1} ($n = 3$). These slopes had a similar trend compared with the estimation (Figure 4.9 (c)). Note that the continuous lines show the spectra predicted by the in-line sensor, which also had a similar shape to the actual spectra. The electric noise and the variation in the manual mechanical operation of the sensor were small enough (shown in Figure 4.7 (b)). The electric noise was under 0.005 V. The variation in the mechanical operation of the sensor was under 0.013 V (standard deviation shown in Figure 4.10 (a)). Thus, the result suggested that the sensor successfully distinguished yellow and green with the slopes in the 3σ scan range.

4.4.2 Concentration Detection with the In-Line Sensor

Next, three samples of green-dyed water with different concentrations were measured to evaluate the concentration detectability of the in-line sensor (Figure 4.11 (a)-(c)). The concentration of the green dye was 5, 10, and 20 mg/mL (Figure 4.11 (a)). The plots of V_n and λ were calculated in the same way as the color detection. (Figure 4.11 (b)-(c)). The raw data with PD (Figure 4.7 (b)) showed that the plots decreased depending on the concentration. The variation of the plots was also low. The slopes of the linear approximation lines (Figure 4.11 (c)) were between $1.6 – 5.6 \times 10^{-4}$ nm^{-1}, resulting in the approximated lines being aligned in parallel. This result showed that the sensor detected the colors were the same because the spectral trend was similar. On the other hand, V_n values at a specific wavelength decreased depending on the increase in the concentration. For example, V_n values at 531 nm wavelength (at the actual peak in reflective wavelength of the green dye) decreased from 0.777 to 0.568 as the concentration increased from 5.0 to 20 mg/mL. The result suggested that the in-line sensor successfully detected the concentration difference.

To confirm that the transmission law (Equation (4.1)) worked normally within the sensor, the molar absorption coefficient ε was calculated from Equation (4.1). The coefficient was calculated from the normalized voltage values near 531 nm (at the actual peak in the reflective wavelength of the green dye) in Figure 4.11 (c). Here, the unit of concentration was expressed by g/L instead of mol/L because the dye contained multiple chemical compounds. Thus, the unit of ε was L/g·mm, and the name of ε should be “absorption coefficient by weight.” The calculated result of ε obtained with the in-line sensor was $2.8 – 5.0 \times 10^{-2}$ L/g·mm. These calculated values were reasonably close to the values with the commercial spectrometer (USB2000+) of $4.1 – 6.4 \times 10^{-2}$ L/g·mm. This result suggested that the prototype in-line sensor had a detectability of the concentration according to Lambert-Beer-Bouguer’s law (Equation (4.1)).

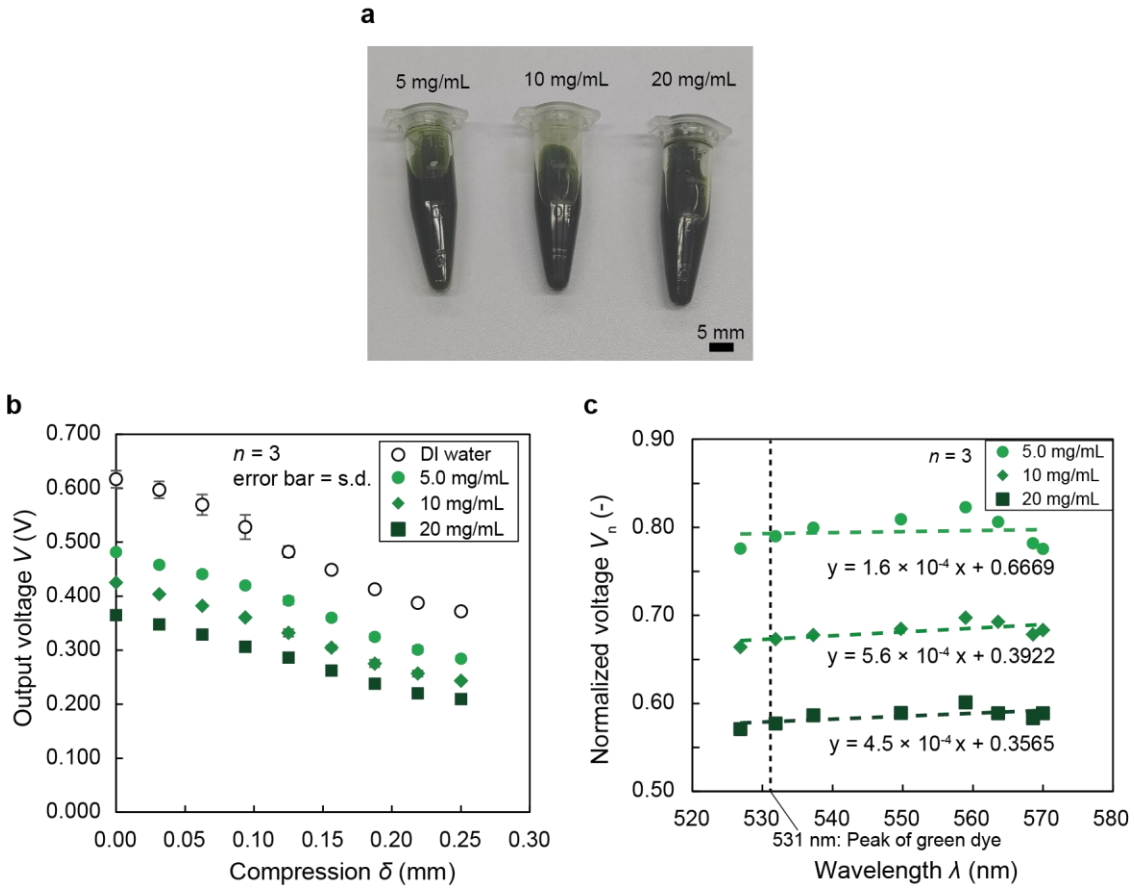

Figure 4.11 Results of the concentration detection with the presented in-line color sensor. (a) Green samples with different concentrations for the measurement. (b) The raw data of the concentration measurements. The graph showed the relationship between the filer compression and the output voltage of the PD. (c) The normalized data of Figure 4.11 (b).

4.5 Demonstration with the In-Line Sensor

Finally, pH values of three different liquid samples with BTB (bromothymol blue) indicator were measured for a demonstration of biochemical applications. Three different sample solutions (pH: 5.32, 6.77, and 7.01) were prepared by mixing BTB solution (ACS, Reag. Ph Eur, Merck KGaA), phosphate solution (pH 7 standard solution, 100–7, HORIBA), and DI water (Figure 4.12 (a)). The concentration of BTB for all samples was 100 mg/L. With the three pH conditions, the colors of the samples ranged from green to yellow. Next, the spectra of the liquid samples were measured with the spectrometer (USB2000+) (Figure 4.12 (b)). The results showed large differences in the 500 nm – 630 nm wavelength range. After that, the three samples were measured with the in-line sensor in the same way as the color detection. The result (Figure 4.12 (c)) showed that the slope of the graph increased from -2.89×10^{-4} to 1.55×10^{-5} after the pH decreased from 7.01 to 5.32. This result showed that the in-line color sensor had a pH detectability from 100 μL of liquid samples combined with pH indicator solutions.

4.6 Conclusion

In this chapter, the in-line microliter liquid color monitoring sensor is proposed.

It was successfully confirmed that the spectrometer-type in-line microliter liquid color sensor with the filter of the structural color polymer had color and concentration detectability. The reflected wavelength was changed by the filter compression, enabling the color detection of the sample liquids with the comparison of the slopes in the λ-V_n graph. In addition, the presented in-line sensor followed the Lambert-Beer-Bouguer law, enabling detection of concentration differences in the sample liquid by comparing the V_n values within the scan range. In addition, it was confirmed that the in-line sensor was applicable to pH detection.

The in-line sensor had the detectability of color and concentration with 100 μL of sample liquid, enabling a compact and simple color/concentration monitoring system for

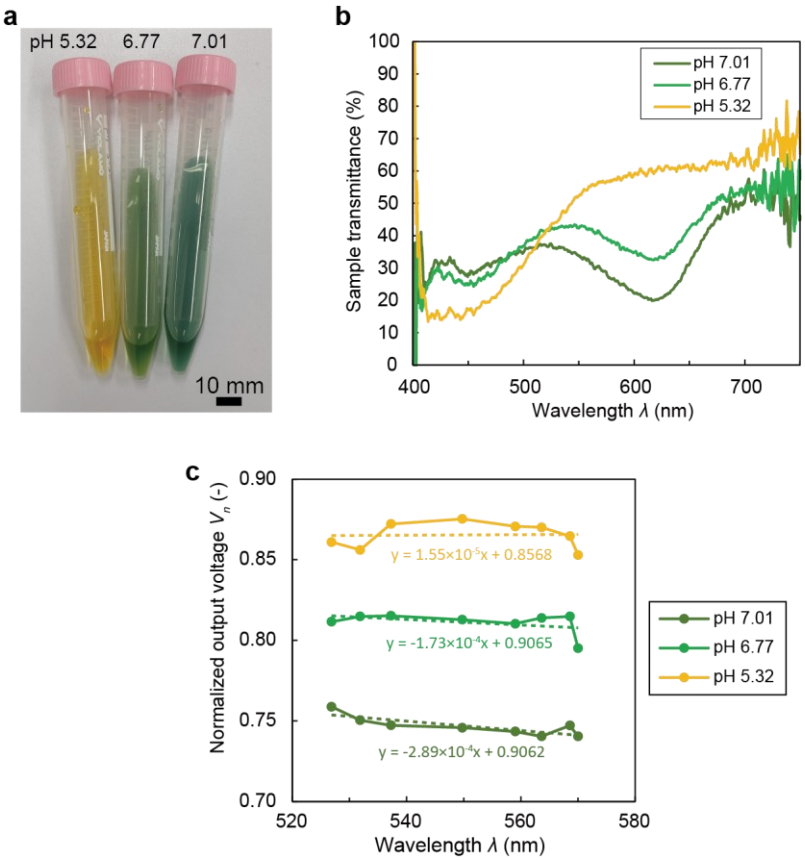

Figure 4.12 Results of the pH detection with the presented in-line color sensor. (a) Measured samples with different pH values. (b) The spectra measured with the commercial spectrometer. (c) The result of the measurement with the in-line sensor.

microfluidic devices. The suggested spectrometer-type in-line color sensor has the possibility for further miniaturization with the following improvements. The current size of the prototype sensor was 40 × 40 × 15 mm. The four screws for fixing the sensor bodies would be replaced with adhesives. Moreover, a piezoelectric actuator or a small linear actuator could be mounted instead of the screw for the filter compression. Therefore, it seemed that approximately 20 × 20 × 15 mm would be achieved easily. This size is smaller than a commercial spectrometer USB2000+ (89.1 × 63.3 × 34.4 mm) or a multiple LED/PD system L-Col 6100 (Anton Paar GmbH, over 100 mm, Max. 4.3 kg). I am sure that the use of the structural color polymer as an optical filter would contribute to miniaturizing the size of in-

line liquid color sensors.

In practical use, some issues with the presented sensor should be solved. The first is the optical resolution. The optical resolution of the presented sensor was around 40 – 80 nm in FWHM, which is much larger than 0.1 – 10 nm in typical commercial spectrometers. The resolution of the structural color polymer is related to the variation of the nanoparticle diameter. By using another bottle of silica nanoparticles with insufficient diameter control (MP-2040, Nissan Chemical), the FWHM was approximately 100 nm. Thus, the diameter of the silica particles must be precisely controlled in mass production. Further process improvements are needed to achieve such precise production. Until this, the suggested in-line sensor is applicable for rough color detection like Section 4.4. Many materials with a visible color often have wide optical spectra [74]. Thus, an optical resolution of less than 10 nm is not necessary only to distinguish the color difference. As evidence, the typical commercial single-color LEDs have 50 nm FWHM. The RGB color sensors (S11059–02DT, Hamamatsu Photonics) have 80 – 100 nm FWHM. Like this, the resolution of the presented color sensor is reasonable as a color/concentration sensor.

Another issue is the operation time of the presented sensor. In the experiments, I waited for 2 – 3 minutes after every scanning sequence until the stress relaxation of the filter had ended. This waiting time is much larger than conventional spectrometers or LED/PD systems, causing a hurdle to rapid spectrum scanning. Property improvement of the polymer, such as decreasing viscosity or increasing elasticity, would lead to shortening the waiting time.

The suggested in-line microliter liquid color sensor is applicable for various applications. As demonstrated in Section 4.5, pH change is measured by the combination with pH-responsive substances. The culture medium also contains a pH-responsive material [75,76]. Thus, automatic cell culturing with color monitoring is also an attractive application. Moreover, quality control of drinks or chemical materials in commerce is one of the most in-demand applications. I believe the presented in-line microliter liquid color sensor with the structural color sensor leads to expanding the field of microfluidic color analysis.

CHAPTER 5.
LITHIUM BATTERY STRESS MONITORING SYSTEM

5.1 Introduction

In this chapter, a mechanical stress sensor for the separator of lithium batteries is proposed.

Energy storage has rapidly grown in demand due to recommendations to decrease gas emissions against climate change with efficient energy use [77,78]. Recently, many applications with energy storage have been developed, such as mobile phones, electric vehicles (EVs), and renewable energy power plants. Especially, lithium batteries have been widely used for such energy storage systems because lithium has a high energy density [79,80]. This property lets us bring our electronic devices anywhere without power lines. However, lithium batteries also have hazardous risks, including smoke emission or fire under overused conditions [81]. Therefore, the abnormality monitoring of lithium batteries has been widely reported to prevent dangerous battery incidents.

Today, three methods for abnormality sensing in lithium batteries have been developed: electric condition (voltage and current) [82–84], temperature [84–86], and dimension monitoring [87–90]. Conventional lithium batteries have electric monitoring ICs (integrated circuits) in battery modules. Also, the temperature is simultaneously monitored with temperature sensors. However, conventional lithium battery modules do not have

displacement or strain sensors, despite the well-known risks of physical breakage or electrical short. One reason is that the prediction of the battery deformation remains challenging. The battery deformation is induced by multiphysic phenomena [91], such as the growth of the lithium dendrites [92–94] or the gas emission [95] from electrolyzed battery materials (electrodes, separators, and electrolytes). Thus, many complex calculations are needed to determine the acceptable threshold of the battery deformation. Even though the displacement sensors would be attached to the lithium batteries, such complex phenomena would lead to large variability. Some studies reported the deformation measurement of the batteries with a conventional displacement meter [87], three-dimensional laser scanning [88], or neutron imaging [89], showing the wavy battery deformation. Moreover, the displacement sensor and FBG (fiber Bragg grating) [90] limit the battery deformation by themselves elasticity. Thus, simultaneous non-contact observation for the distribution of the battery deformation and for the physical phenomena in the battery is one of the effective methods to understand the battery status.

Here, a structural color polymer-based separator is proposed, which also works as a colorimetric stress sensor to detect the battery deformation status (Figure 5.1(a)). This separator stress sensor is named CSDS (colorimetric stress-detectable separator). The CSDS is made of a structural color polymer consisting of aligned silica nanoparticles in PEGPEA (Figure 5.1(b)). The structural color polymer exhibits a specific visible color dependent on the mean distance between the nanoparticles, enabling separator deformation sensing. The CSDS also transfers ions after electrolyte penetration, as well as separators in conventional lithium batteries [96]. Repeated charging and discharging cause gas generation and dendrite growth in the lithium batteries, changing the distance between the nanoparticles. Then, the distance change causes a color change in the separator. These mechanisms are preferable to external strain sensors because the colorimetric sensor enables direct observation of deformation distribution inside the battery electrodes. The battery pouch and one of the electrodes were intentionally punched to form a window for direct observation from outside the battery. The CSDS and the battery window achieve the simultaneous detection of deformation and phenomena such as gas emission and dendrite growth. The CSDS as an

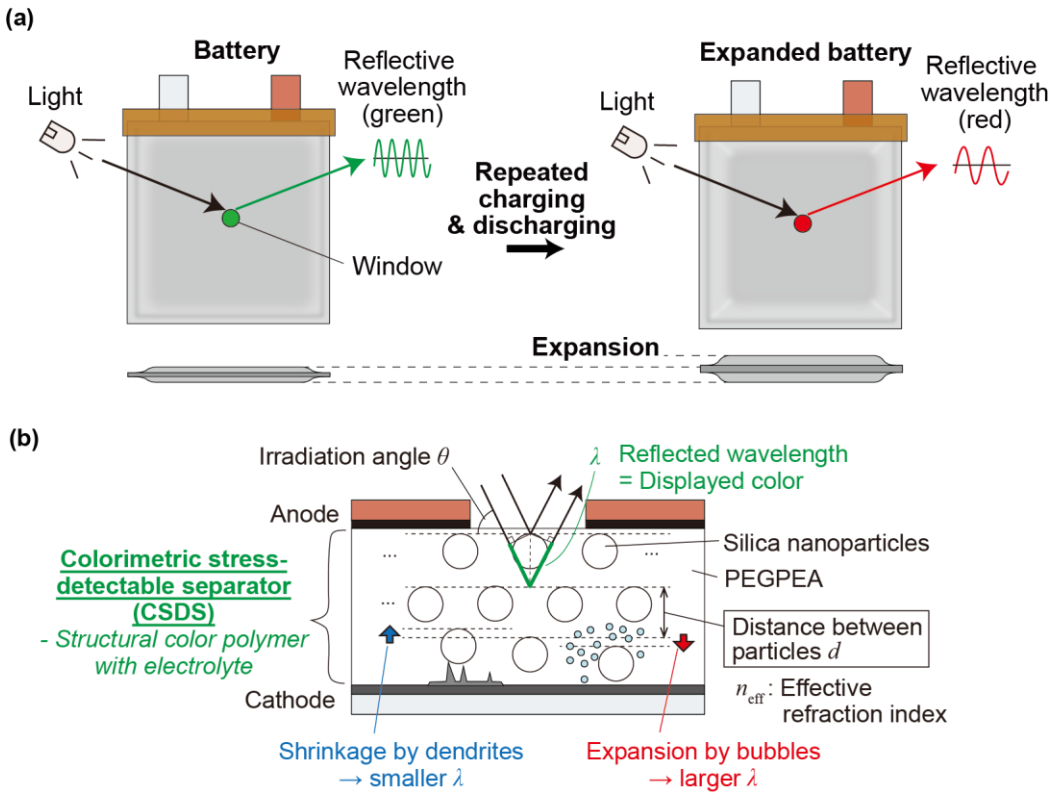

Figure 5.1 Concept of the colorimetric stress-detectable separator (CSDS). (a) The presented lithium battery has the CSDS, displaying the battery expansion with color change to red. (b) The CSDS is applied into lithium battery to observe deformation inside of the battery. Bubbles cause expansion of the separator, leading to color change to red. On the other hand, dendrites cause shrinkage, leading to color change to blue.

additional status notification sensor enables us to detect abnormalities related to deformation at the ends of the battery lives.

5.2 Principles of Lithium Batteries

5.2.1 Normal Chemical Reaction in Lithium Batteries

A typical lithium-ion battery consists of an anode, a cathode, a separator, and an electrolyte. In the following experiments, a C/Cu (carbon/copper) anode, a $LiFePO_4$(lithium

iron phosphate)/Al(aluminum) cathode, and a LiTFSI (lithium bis(trifluoromethane-sulfonyl)imide) / EC (ethylene carbonate) + DMC (dimethyl carbonate) solution for the electrolyte. Generally, the chemical reaction in $LiFePO_4$ battery systems, including the above system, is expressed as

$$\text{(anode)} \qquad x\mathrm{Li}^+ + xe^- + 6\mathrm{C} \rightleftarrows \mathrm{Li}_x\mathrm{C6} \tag{5.1}$$

$$\text{(cathode)} \qquad \mathrm{LiFePO_4} \rightleftarrows \mathrm{Li}_{1-x}\mathrm{FePO_4} + x\mathrm{Li}^+ + xe^-. \tag{5.2}$$

Here, the rightward arrows indicate discharging reaction and the leftward arrows indicate charging. In initial charging, the Li ions are introduced into the carbon structure. The layer formed by this initial reaction is called SEI (solid electrolyte interphase). Dendrites often grow from the SEI layer after the repeated chemical reactions shown above. This reaction is not abnormal but troublesome in that the dendrites cause the battery deformation.

5.2.2 Abnormal Chemical Reaction in Lithium Batteries

After cyclic charging and discharging, some gases are also produced from organic solvents at high voltage and high temperature [95]. The examples of such reactions are expressed as

$$2\mathrm{EC} + 2e^- + 2\mathrm{Li}^+ \rightarrow (\mathrm{CH_2OCO_2Li})_2 + \mathrm{C_2H_4\,(g)} \tag{5.3}$$

$$2\mathrm{ROCO_2Li} + \mathrm{H_2O} \rightarrow 2\mathrm{ROH} + \mathrm{Li_2CO_3} + \mathrm{CO_2\,(g)} \tag{5.4}$$

$$\mathrm{EC} + 2\mathrm{Li}^+ + 2e^- \rightarrow \mathrm{Li_2CO_3} + \mathrm{C_2H_4\,(g)}. \tag{5.5}$$

Those unintended reactions cause microbubbles of those gases, resulting in mechanical stress to the battery structure. In addition, unintentional electrolysis of electrode and separator materials has been reported. A material of the electrolyte in conventional lithium batteries $LiPF_6$ (lithium hexafluoro-phosphate) is reported to cause HF (hydrogen fluoride) after

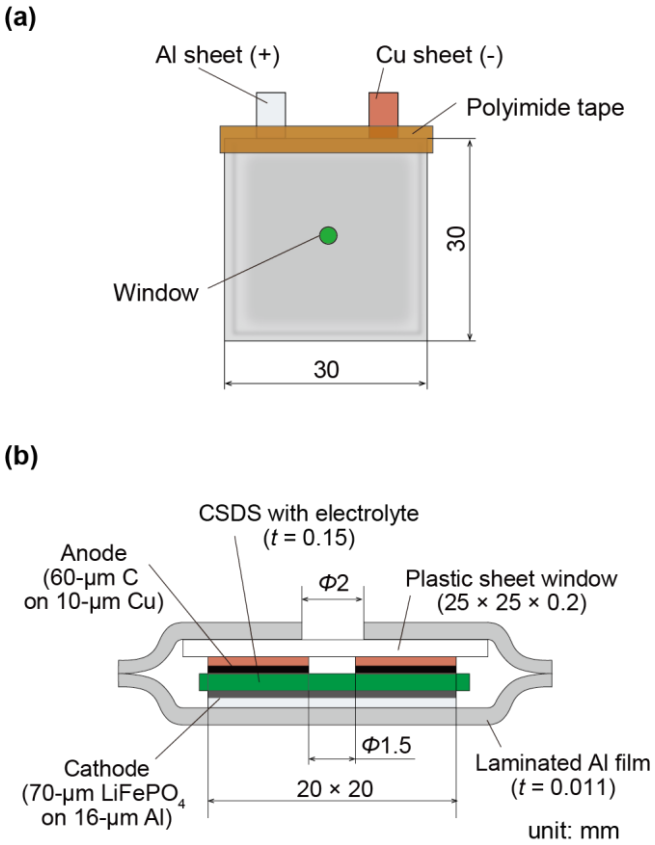

Figure 5.2 Design of the lithium battery. (a) Front view of the battery. The battery size was 30 × 30 mm. (b) Cross-sectional view of the battery. The electrode size was 20 × 20 mm.

reaction with water. Thus, LiTFSI was used in the following experiments instead of $LiPF_6$.

5.3 Design of the Stress Sensor and the Lithium Battery

In this chapter, the design of the proposed battery is explained. The size of the battery pack was set to 30 × 30 mm (Figure 5.2 (a)). The CSDS was sandwiched between a cathode and an anode (Figure 5.2 (b)). The sizes of the electrodes were both 20 × 20 mm. To observe the stress distribution with visible colors from outside the battery pack, a 2-mm window was designed. The anode also had a 1.5-mm window for observation of the CSDS.

The window of the battery pack was made of a plastic sheet sealed with adhesive. The material of the window should be transparent and colorless for accurate color observation and fire-resistant for safety. At this time, the window was made of a normal plastic sheet, PLA (polylactic acid), because transparency took priority over the fire resistance to demonstrate the concept. A small glass window would be a better choice for practical use.

5.4 Assembly of the Lithium Battery with the Stress Sensor

Next, the assembly process of the lithium battery is explained. The lithium battery was assembled after the polymer fabrication (Figure 5.3 (a)). The fabrication process of the structural color polymer was explained in Chapter 3. The thickness of the polymer was set to 0.15 mm. This thickness was determined by the lower limit of manual fabrication. Next, a 1.0 M LiTFSI/EC+DMC solution was prepared for the electrolyte. The ratio of the EC and the DMC was 1 : 1. After that, 50 μL of the electrolyte was spread on the CSDS by a fluorine-coated glass. 24 hours were required for the completion of the electrolyte penetration. By changing the particle diameter, three colors of the CSDS sheets were fabricated (Figure 5.3 (b)). In the next step, a cathode ($LiFePO_4$, 1.25 mAh/cm^2, NANOMYTE BE-60E, NEI corporation) and an anode (C, 2.40 mAh/cm2, NANOMYTE BE-200E, NEI corporation) were prepared. An Al sheet was attached to the cathode and a Cu sheet to the anode to connect to the external power source. After these preparations, the CSDS was sandwiched between the cathode and the anode, completing the cell assembly.

The battery pouch was made of a laminated aluminum sheet (30 × 60 mm, EQ-ALF-100-115, MTI Japan) and a transparent PLA sheet (25 × 25 mm, SBP101, Sheedom Co., Ltd.). The PLA sheet was glued to the laminated aluminum sheet with an adhesive (Aron Alpha for plastics, KONISHI Co., Ltd.). To prevent gas emissions, the adhesive was applied along the window. After that, the laminated aluminum sheet was folded along the center line. Heat compression bonding was conducted on the three edges of the aluminum sheet to fabricate a pouch. Next, the fabricated battery cell was inserted into the pouch. Finally, the

inlet of the pouch was sealed with polyimide tape (Figure 5.3 (c)). The metal sheets for connection were exposed at this time.

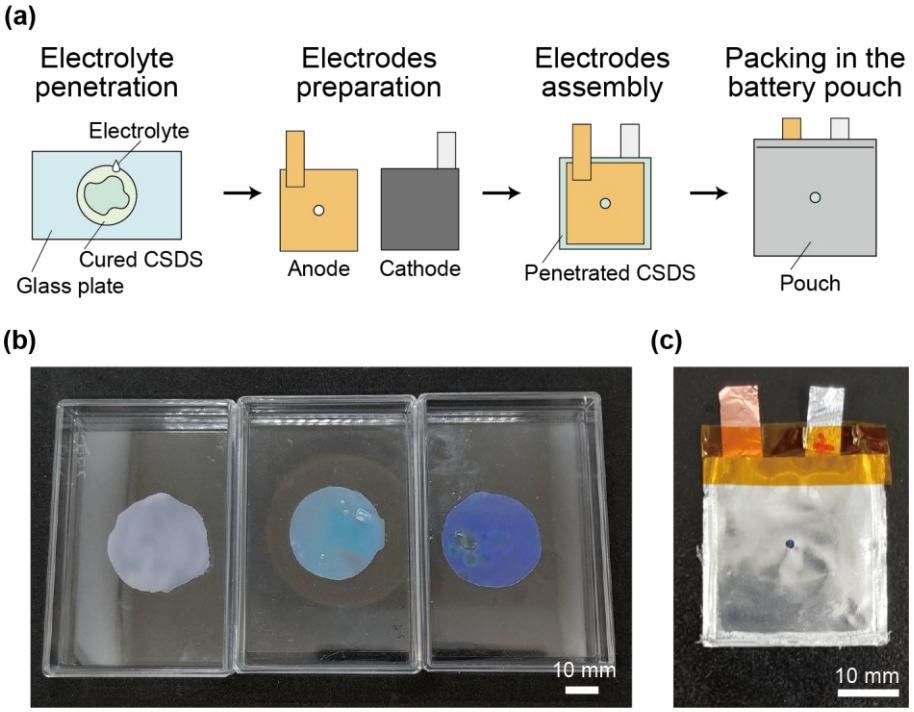

Figure 5.3 (a) Assembly process of the battery. (b) The fabricated structural color polymer sheets. Three colors of sheets were fabricated. (c) The fabricated lithium battery.

The impedance of an assembled battery was measured six times using an LCR meter (IM3536, HIOKI) at 1 kHz and 0.1 V before the initial charging. The impedance was 63.87±0.19 Ω (standard deviation) as a result. Thus, the electric conductivity of the electrolyte-penetrated polymer was confirmed. After that, the initial charging to form the SEI layer was conducted at 4.2 V and 10 mA for approximately 2 hours with a power source.

5.5 Experimental Results

5.5.1 Battery Capacity Decrease and Deformation in Charging and Discharging

To grasp the end of the battery life, the battery capacity and the battery expansion during charging and discharging were measured (Figure 5.4 (a)). Applied voltage and current were controlled with a charging/discharging tester (ECD5-5-LThUs1, Matsusada Precision Inc.). Electrical conditions were as follows: charging was conducted in CC-CV mode. First, 10 mA CC (constant current) charging was performed, followed by 4.2 V CV (constant voltage) charging for 30 minutes. Discharging was CC mode at 10 mA until the current decreased to 1 mA. The total time of charging and discharging fluctuated around 30 minutes. Under these electrical conditions, no temperature increase of the battery was observed (Figure 5.4 (b)) based on thermography (TIM-03, AS ONE). Note that the electrolyte of this battery sample was different: 1.0 M of LiTFSI/EMImTFSI(1-Ethyl-3-methylimidazolium Bis(trifluoromethanesulfonyl)imide, ionic liquid). The electrical conditions were fixed in the following experiments. The displacement monitoring system for the battery consisted of a laser displacement meter (HL-G103-A-C5, Panasonic Industrial Devices SUNX Co., Ltd.) and a data logger (DL350, Yokogawa Electric Co.). The displacement measurement point was set 5 mm away from the observation window because the edge of the window would cause unintended reflection of the laser. In addition, polyimide tape was attached to the laser measurement point to prevent the electrode from rusting. The displacement measurement was conducted after the initial charging because the charging time was stabilized from the second charging. For this reason, this second charging is written as cycle number one in the following experiments.

The monitoring result of the capacity change (Figure 5.4 (c)) showed that the charging capacity decreased depending on the increase in charging/discharging cycles. The capacity at 100 cycles was 0.51 mAh, a 69% decrease from the initial capacity of 1.67 mAh. The value of 0.51 mAh was the lower limit derived from the current measurement capability of the charging/discharging tester. Thus, the end of battery life was considered to be around 100 cycles. For this reason, the charging/decreasing cyclic test was conducted for 100 cycles

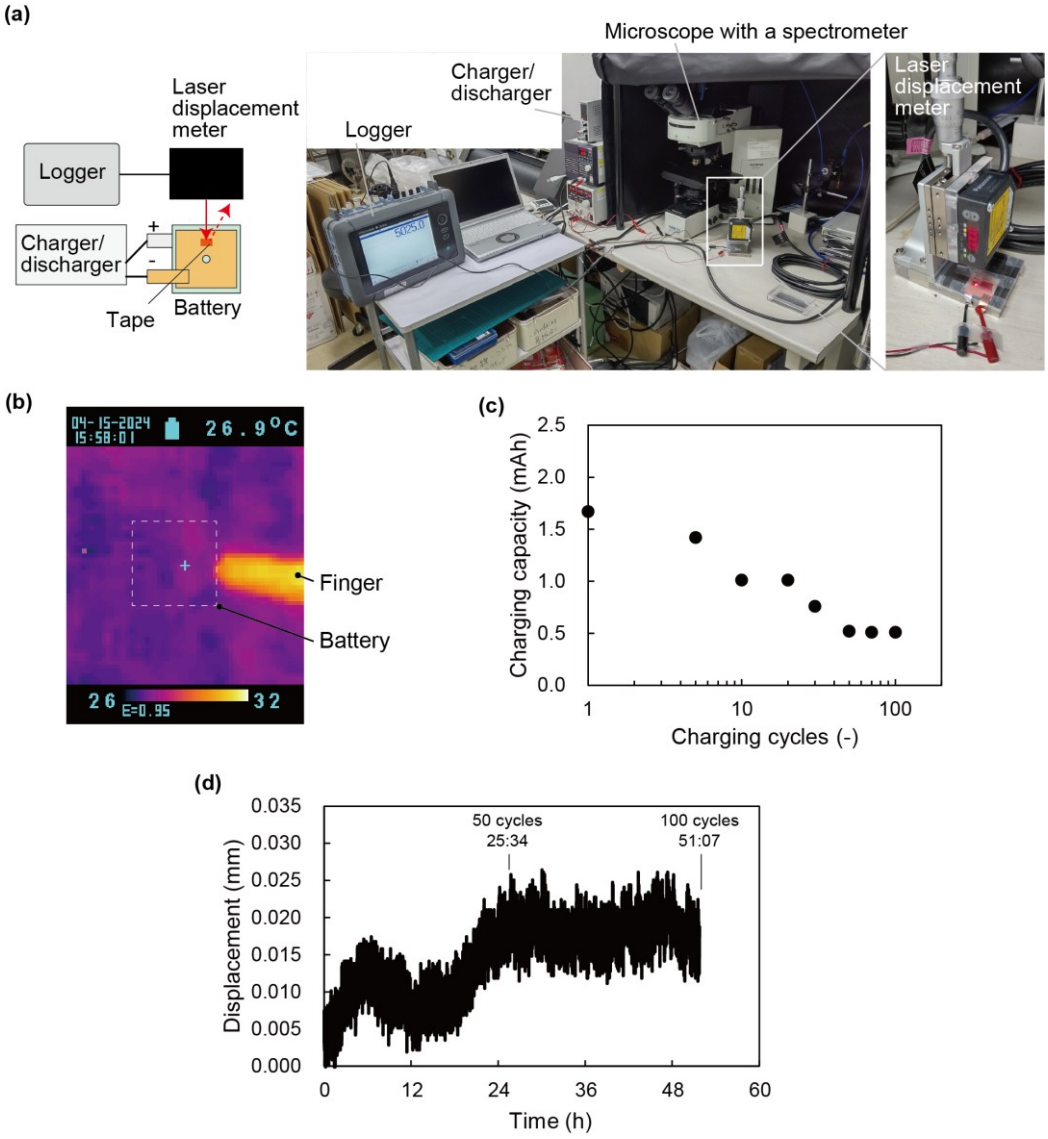

Figure 5.4 Monitoring results of capacity and expansion of the fabricated battery. (a) The measurement system for the battery capacity, the battery deformation, the CSDS spectra, and the CSDS color. For the color monitoring, the camera was attached to the eyepiece of the microscope. (b) The temperature increase of the battery in charging/discharging test. (c) The capacity change in the cyclic test of charging and discharging. 0.5 mAh was the lower limitation of measurement. (c) The displacement changes in the cyclic test of charging and discharging. The positive direction means the battery expansion.

in the following experiments. Here, the theoretical charging capacity was 5 mAh, much larger than the measured charging capacity, 1.7 mAh (Figure 5.4 (c)). I used minimum and safer

materials, possibly causing side reactions leading to this capacity decrease.

The monitoring result of the deformation showed that the battery expanded 0.015 mm after 100 cycles (approximately 50 h) (Figure 5.4 (d)). The thickness of the initial separator was 0.15 mm. Thus, a +10% expansion occurred after the cyclic test.

From these two monitoring results, it was confirmed that the conventional sensing methods for battery deterioration – battery capacity decrease and battery expansion – were effective even in the fabricated battery.

5.5.2 Stress Monitoring with Color Changes of CSDS in Charging and Discharging

To investigate the phenomena causing battery deformation during battery life, a color monitoring system with the CSDS was prepared (Figure 5.5 (a)). The initial color of the CSDS was green. Two microscopes were used depending on usage: for high-saturated timelapse images (Microscope BX53M with an LED light source BX3M-LEDR, Olympus) and for spectrum monitoring (Microscope BX50 with a halogen lamp U-LH100, Olympus). The color change of the CSDS was monitored with a camera (α6400L, SONY) and a spectrometer (USB2000+, Ocean Optics). The camera recorded the pictures every minute. The spectra were measured manually at specific times. The charging/discharging conditions were the same as in Section 5.5.1. The cyclic test was conducted 100 times.

First, the timelapse images of a fabricated battery were recorded with the camera. The timelapse images showed that the CSDS changed color during the cyclic charging/discharging test (Figure 5.5 (b) and Figure 5.6). The CSDS color changed to red, with some microbubbles simultaneously appearing at 10 h (~20 cycles). This result suggested that the electrolyzed gases expanded the separator in the early stages of the battery life. It was also confirmed that the color near the window edge turned blue, which differed from the trend at the center. Some crystals were formed along the edge of the window at 48 h (Figure 5.5 (b), right-bottom), suggesting the dendrites gave shrinking mechanical stress to the separator. The spectrum change in no current was not confirmed (Figure 5.6).

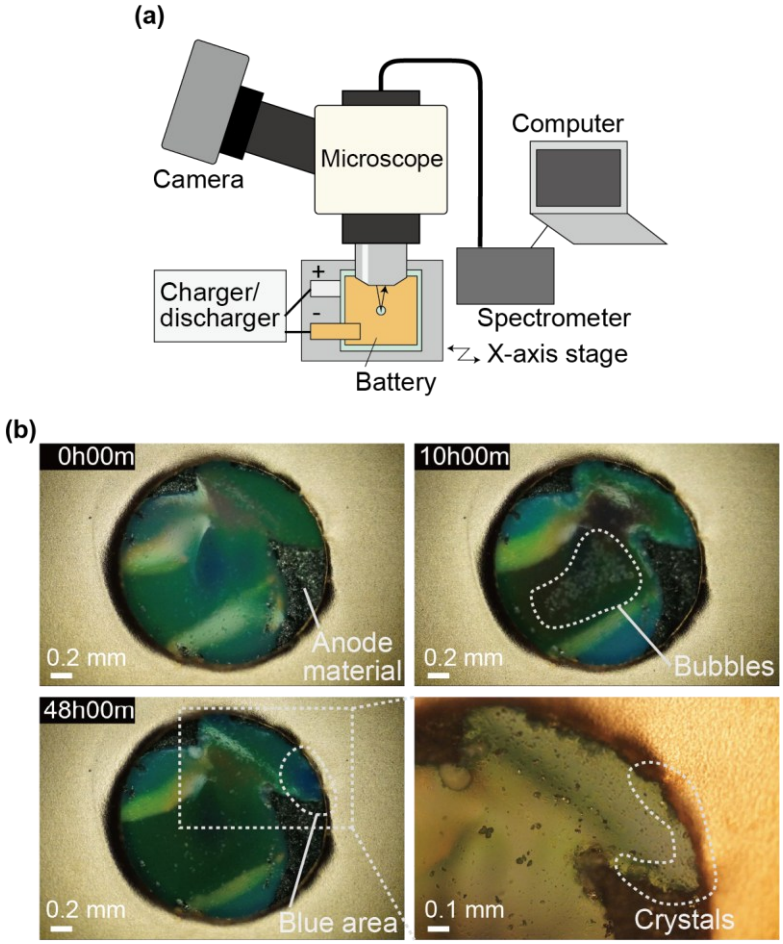

Figure 5.5 (a) Color and spectrum monitoring system. (b) Monitoring results of color observation with a camera. Microbubbles caused red color change and crystals growth caused blue color change.

Next, to quantify the color change with the spectrum change, the spectrum changes of the CSDS at five positions were measured with the camera (Figure 5.7 (a)) and the spectrometer (Figure 5.7 (b) and 5.8 (a)-(b)). A new battery was prepared for this experiment. The initial color of the CSDS was 524-538 nm (green) (Figure 5.8 (a)). The images and the spectrum graphs showed similar changes to Figure 5.5 (b): the spectra change at the center of the hole changed to red (~580 nm) twice, after 9 h (~18 cycles) and after 48 h (~95 cycles). This result suggested that the chemical reaction generating gases possibly had two stages:

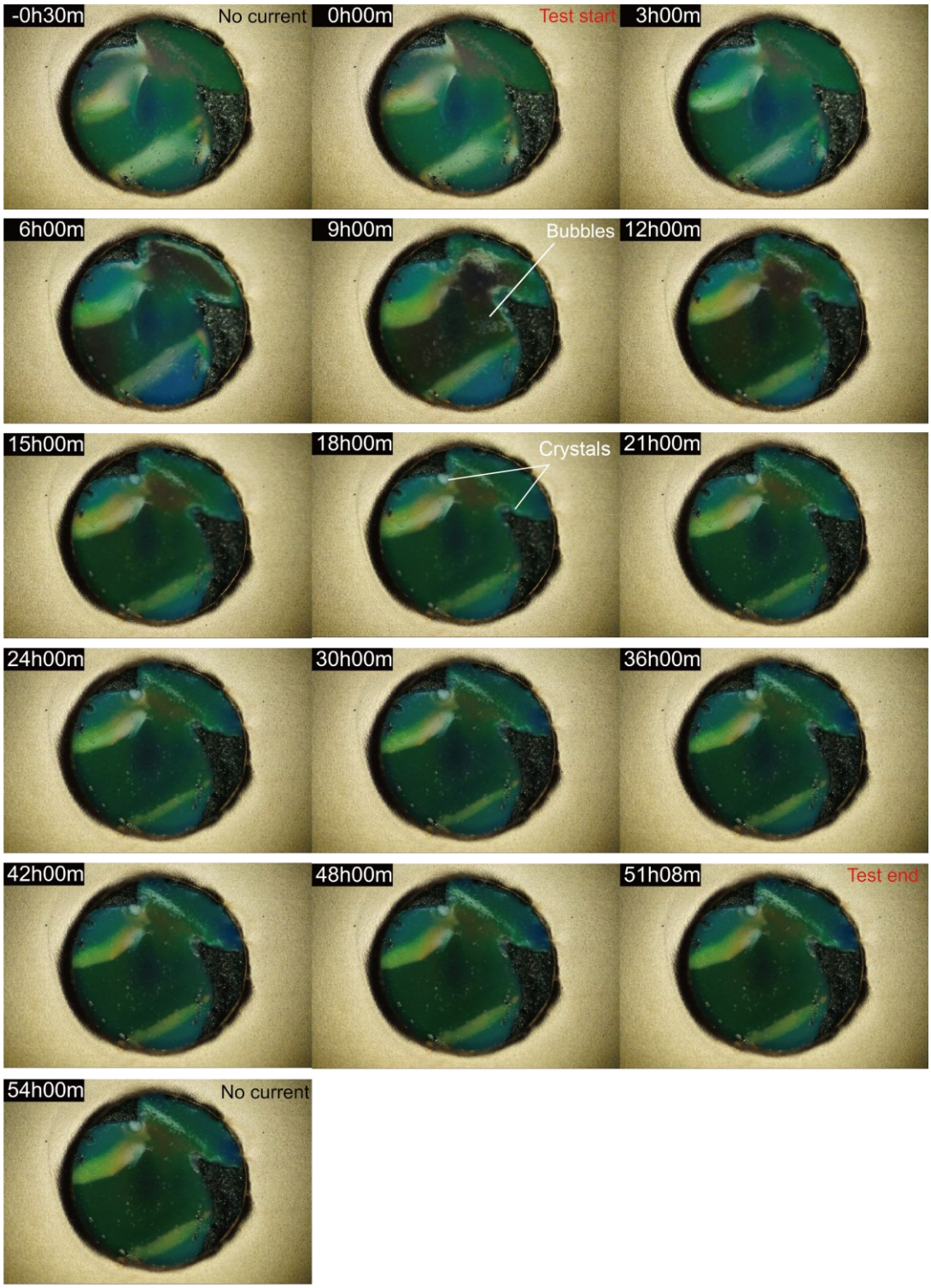

Figure 5.6 Detailed monitoring results of color observation with a camera.

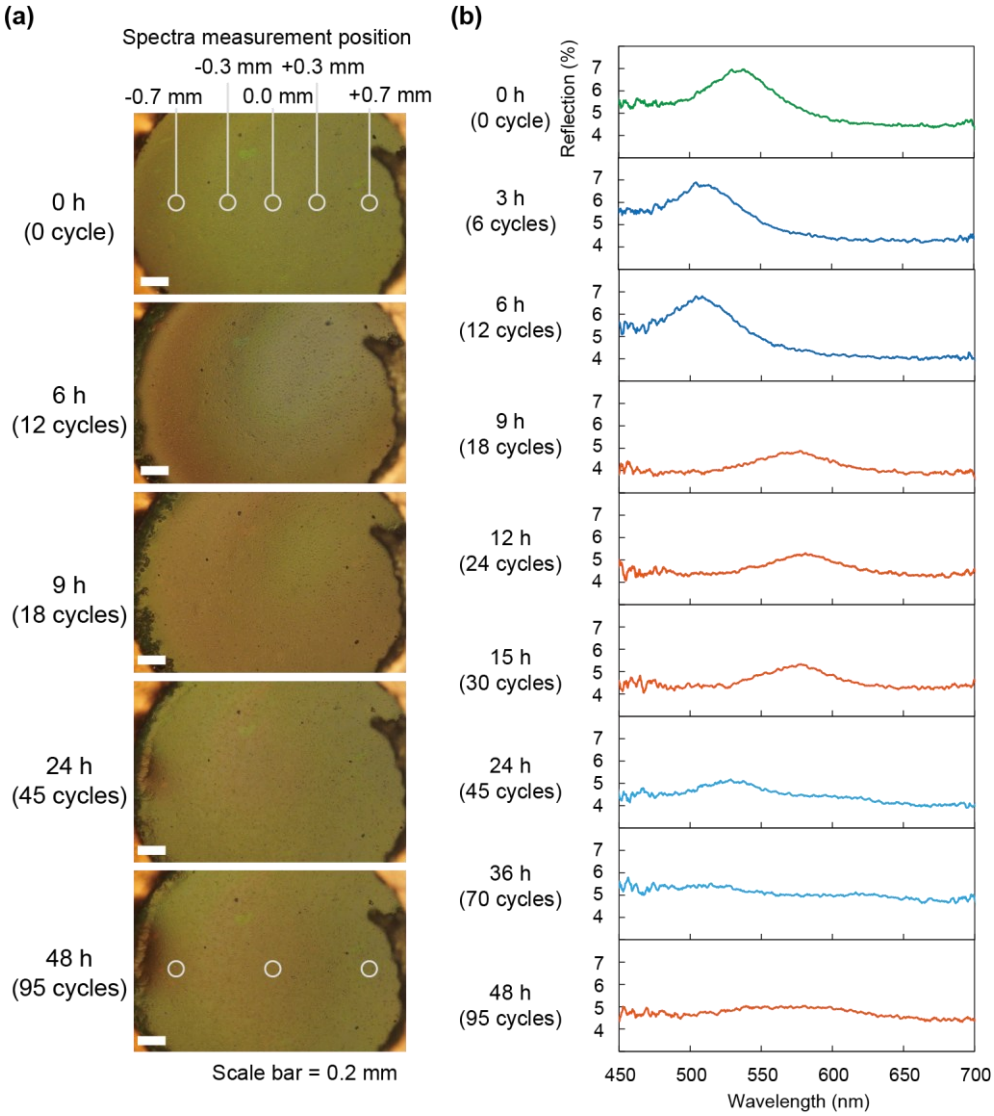

Figure 5.7 Simultaneous monitoring results of the color and spectrum change. (a) The color monitoring result. The spectra at five positions were measured. (b) The result of the measurement of the spectrum changes at 0.0 mm position.

initial reaction and deteriorating reaction. On the other hand, the color change near the edge of the window (+0.7 mm, -0.7 mm) showed the initial color change to red and the following color change to blue (Min. 514 nm). The crystals were also observed near the edge of the window. It suggested that the shrinkage force caused by the dendrites near the edge was more dominant than the expansion force caused by the gas microbubbles. The result of the position

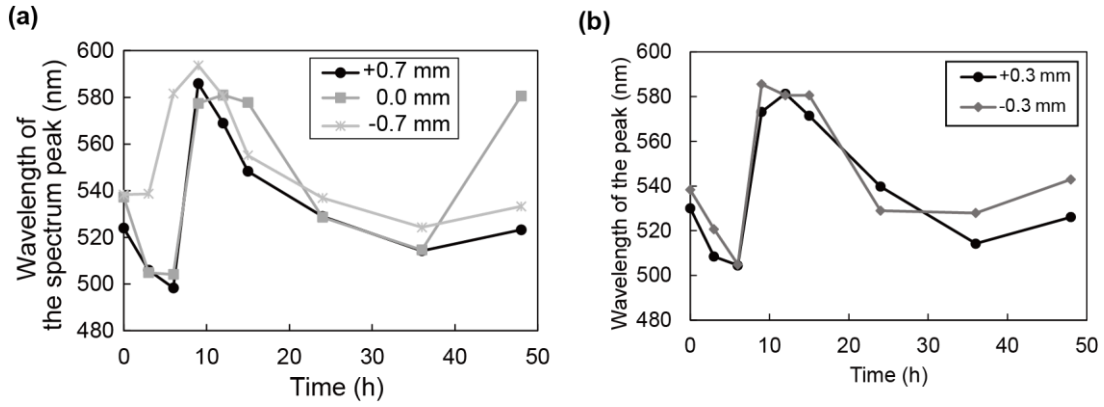

Figure 5.8 Monitoring results of the wavelength at the spectrum peaks. The measurement positions were (a) -0.7, 0.0, +0.7mm and (b) -0.3, +0.3 mm. The first stage of the battery life showed the red color (expansion). The second stage showed blue to green (shrinkage). The positions 0.0 mm and +0.3 mm showed third stage to red in the end of the battery life.

-0.3 mm showed a moderate change (543 nm) at 48 h (Figure 5.8 (b)). Combined with the result of the position 0.0 mm, the results suggested that the local change happened around the center of the window.

The peak values of the reflective spectra decreased but did not disappear at 48 h (Figure 5.7 (b)), suggesting the CSDS had sufficient endurance throughout 100 cycles, which represents the full battery life. As shown above, the expansion and shrinkage stress using the presented colorimetric stress-detectable separator was successfully observed with visible light throughout the battery life.

Finally, the mechanical stress was estimated (Figure 5.9) using Equation (2.8) and Equation (3.1). Here, the stress border determined from the strain border was -10.91 kPa. If the measured stress was smaller than this value, the upper equation in Equation (3.1) should be used. This time, the estimated stress values from E = 120 kPa were all higher than -10.91 kPa, resulting in the appropriate calculation. From the estimation (Figure 5.9), the maximum stress was 14.18 kPa expansion (+0.7 mm, 9 h), and the minimum stress was -7.39 kPa shrinkage (0 mm, 6 h). As shown above, the CSDS enabled local and small stress measurement through the color distribution of the structural color polymer.

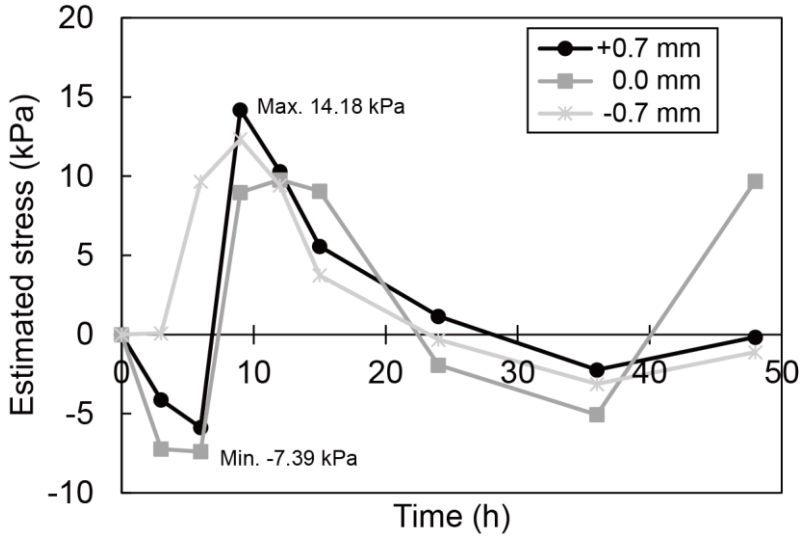

Figure 5.9 Estimated stress from Equation (2.8) and Equation (3.1). The optical data in Figure 5.8 (a) were used. The maximum stress was 14.18 kPa (expansion), while the minimum stress was -7.39 kPa (shrinkage).

5.6 Conclusion

In this chapter, the presented separator with the stress-sensing function, CSDS, was examined. The CSDS successfully visualized the stress change through color change during the charging and discharging cycles. The color changes were observed in areas where the microbubbles occurred and the crystals grew, possibly causing the deformation of the CSDS. The CSDS revealed that the color change from green to red (indicating polymer expansion) occurred twice, during the initial reaction and deterioration. The suggested CSDS has applicability to building a battery deterioration model in mechanical simulations and to utilizing a simple indicator of the battery deterioration status.

In the structure of the presented battery, a window was provided in the anode electrode to visualize mechanical stress with color in the battery. This would affect the electric field in the separator, possibly causing some different phenomena from the normal batteries. Thus, some simulations of the interaction between the mechanical stress and the

electric field should be conducted using feedback from the CSDS results. To ensure the accuracy of the multiphysics simulation, the unevenness of the CSDS color should be improved. This uneven color of the CSDS resulted from the fabrication and assembly processes. It is desirable to reduce the diameter variation of the silica nanoparticles and to compress the CSDS and electrodes vertically during the assembly process.

The proposed CSDS has the potential to be applied as a color indicator of battery life. When the color change process is fully predicted by the deformation simulation, the CSDS color enables clear visualization of battery deterioration at a glance. Such easy color-based notification will lead to the suppression of dangerous hazards such as fire or fuming, and to the recommendation of replacing lithium battery products.

CHAPTER 6. CONCLUDING REMARKS

6.1 Conclusion

The objective of this dissertation was to broaden the functional concept of non-hydrogel structural color polymers as transducers between light and deformation (optical and mechanical information) through the extension of sensing methodology. To achieve this goal, the author chose silica-PEGPEA polymer, which is stable against evaporation and under electric currents. The thin and soft polymeric sheet had some advantages against traditional transducers, such as ease of fabrication, continuous deformation-to-wavelength conversion, and sensing of stress distribution.

In this dissertation, two monitoring sensors with the silica-PEGPEA polymer were proposed. The first was the in-line microliter liquid color monitoring sensor. The fabricated polymer was used for an optical filter in the in-line spectrometer to change the wavelength of light irradiated onto the liquid sample, necessary for the spectrum scan. It was revealed that the parallel compression of the fabricated polymer resulted in continuous decreases in the reflective wavelength. With the relationship between the compression and wavelength, the presented in-line color sensor achieved color and concentration detection without interrupting the electric circuit. During the repeated spectrum scan, the silica-PEGPEA polymer had mechanical durability, resulting in small variations. Although the wavelength resolution was low due to the deviation of the particle diameters, the in-line sensor showed

long-term stable measurements with the simple device structure. The second is the stress monitoring sensor for the separator of lithium batteries. The silica-PEGPEA polymer had the capability of electrolyte penetration, enabling measurement in water-reactive materials, including but not limited to a lithium-based electrolyte. The fabricated polymer displayed mechanical stress distribution with color changes during the battery life, revealing that microbubbles caused expansion and crystal growth caused shrinkage. These phenomena were visualized by the structural colors of the silica-PEGPEA polymer, enabling people to grasp the battery condition at a glance using the sensor.

In summary, it was demonstrated that non-hydrogel structural color polymers are available for continuous transducers between stress distribution and reflective spectrum distribution. The methodology of non-hydrogel structural color polymers was extended through novel sensing mechanisms and stable material properties suitable for water-prohibited environments. In optical sensing, the soft silica-PEGPEA polymer showed continuous wavelength changes with the parallel compression mechanism. In deformation sensing, the polymer provided a measurement method for the stress distribution by chemical reactions in the long term, resulting from the color change of the thin silica-PEGPEA polymer. These unique advantages of the non-hydrogel structural color polymer are expected to contribute to the development of applications as transducers between light and mechanical deformation.

6.2 Future Perspectives

The non-hydrogel structural color polymer successfully worked as sensors or color-changing elements. However, some troublesome properties of the polymer also existed.

The first is the wide FWHM. A smaller FWHM will cause higher spectral measurement resolution. The minimum FWHM in this study was 50 nm, much larger than the resolution of current spectrometers: 0.1 nm. Therefore, it is necessary to decrease the FWHM by improving the particle diameter distribution and the particle alignment methods. However, this improvement will possibly increase costs and strengthen the angle dependence.

In practice, it is preferable to customize the particle diameter and alignment process according to the required resolution.

The second is the strong adhesiveness of the silica-PEGPEA polymer. The structural color polymer mounted on the in-line color sensor was fluorine-coated because the polymer stuck to hands, tweezers, and the acrylic housing. Section 4.3.2 showed it took several minutes for the reflective wavelength on the polymer to return to the initial state. This may be because the adhesiveness of the polymer was not sufficiently reduced. It was confirmed that the polymer did not adhere to PDMS or fluorine-coated glass. Thus, these materials are recommended in some situations where mechanical sliding or non-adhesiveness is required.

The third is that Young's modulus characteristics of the structural color polymers are different from those of pure polymers. The structural color polymers contain large amounts of silica nanoparticles, affecting the refractive index and Young's modulus. As shown in Figure 3.9, Young's modulus of the silica-PEGPEA polymer increased in the range of large compressive strain. Thus, designs without considering Young's modulus may result in failure.

Despite these characteristics, more application development of the structural color polymers is expected. The feature that the structural color polymer enables to convert force to color is useful for feedback to simulations. The structural color polymer enables the visualization of forces directly with reasonable temporal and spatial resolution. The temporal resolution was estimated from the stress relaxation shown in Fig. 3.7 (c); 90% relaxation in 3.3 s. The spatial resolution theoretically depends on the particle distance. In practical use, the probe diameter of spectrometers or the resolution of cameras limits the spatial resolution. This force-visualizing capability of the structural color polymer enables measurement of basic local forces, such as surface tension, stickiness, and friction. These basic measurements will lead to solving complex deformation phenomena, such as the deformation of the lithium battery. In addition, it was shown that the structural color polymer had high electrical conductivity after penetration of the electrolyte. This feature enables the development of devices related to force, light, and electricity. For example, Q. Lyu *et al*. have already reported

a touch display with a color response [97]. In our laboratory, H. Goto fabricated structural-colored microbeads for an ultrasonic display [98]. These developments will enhance human experiences in both research and daily life. By bridging the gap between force and light, structural color polymer-based transducers offer practical and innovative applications.

Acknowledgments

My research activities have received great cooperation from countless people. At the end of my dissertation, I would like to state my appreciation for it.

First of all, I would like to thank Prof. Hiroaki Onoe. He supported me during these years of the PhD course. This challenging plan to change my career could not have been achieved without his cooperation. I have learned many skills for research and writing from him through the years in my bachelor's, master's, and doctoral courses. I am sure that this experience with Prof. Onoe will help me in my next career.

Next, I would like to thank the members of the Onoe laboratory. Despite my sudden return, they accepted me and joined the discussion of my theme. In addition, their ideas were interesting and useful in my consideration of this micro- and nano-engineering field. Sometimes I joined their events and refreshed, resulting in better progress in my research.

Also, I would like to mention the graduated PhD members of the Onoe laboratory, especially Koki Yoshida and Shun Itai. I referred to their experience, leading to some troubleshooting in my research life.

Of course, I thank my parents for their great endurance during these years. I knew this plan was so challenging that I did not explain the details of my situation, probably causing a lot of anxiety. I must say a big thanks to them.

Finally, I apologize to the members of the relay team at Panasonic Corp. for the change of my mind regarding my career. My retirement might cause some changes in personnel planning. I hope the products I developed will grow.

During these doctoral years, generative AI (artificial intelligence) has spread, causing large changes in the manufacturing industry. Some groups may replace human intelligence with AI in the next decades. However, I am sure that the doctoral skills will lead to breakthroughs in various fields, never to be replaced by AI.

Anyway, I believe this PhD course could be completed thanks to the cooperation

of many others beyond those mentioned above. I sincerely appreciate the support and cooperation of everyone involved.

Satoshi Nishita

References

[1] Z. Zhang, Z. Chen, L. Shang, Y. Zhao, Structural Color Materials from Natural Polymers, Adv Materials Technologies 6 (2021) 2100296. https://doi.org/10.1002/admt.202100296.
[2] Z. Xuan, J. Li, Q. Liu, F. Yi, S. Wang, W. Lu, Artificial Structural Colors and Applications, The Innovation 2 (2021) 100081. https://doi.org/10.1016/j.xinn.2021.100081.
[3] H. Wang, K.-Q. Zhang, Photonic Crystal Structures with Tunable Structure Color as Colorimetric Sensors, Sensors 13 (2013) 4192–4213. https://doi.org/10.3390/s130404192.
[4] F. Qi, Z. Meng, M. Xue, L. Qiu, Recent advances in self-assemblies and sensing applications of colloidal photonic crystals, Analytica Chimica Acta 1123 (2020) 91–112. https://doi.org/10.1016/j.aca.2020.02.026.
[5] Y. Hu‡, Y. Zhang‡, D. Yang, D. Ma, S. Huang, Self-assembly of colloidal particles into amorphous photonic crystals, Mater. Adv. 2 (2021) 6499–6518. https://doi.org/10.1039/D1MA00477H.
[6] R. Hooke, Micrographia: Or Some Physiological Descriptions of Minute Bodies Made by Magnifying Glasses. With Observations and Inquiries Thereupon. By R. Hooke, Fellow of the Royal Society, Jo. Martyn, 1667.
[7] I. Newton, Opticks, Or, A Treatise of the Reflections, Refractions, Inflections & Colours of Light, Courier Corporation, 1952.
[8] J. Zi, X. Yu, Y. Li, X. Hu, C. Xu, X. Wang, X. Liu, R. Fu, Coloration strategies in peacock feathers, Proceedings of the National Academy of Sciences 100 (2003) 12576–12578. https://doi.org/10.1073/pnas.2133313100.
[9] S. Kinoshita, S. Yoshioka, K. Kawagoe, Mechanisms of structural colour in the *Morpho* butterfly: cooperation of regularity and irregularity in an iridescent scale, Proc. R. Soc. Lond. B 269 (2002) 1417–1421. https://doi.org/10.1098/rspb.2002.2019.
[10] J. Teyssier, S.V. Saenko, D. Van Der Marel, M.C. Milinkovitch, Photonic crystals cause active colour change in chameleons, Nat Commun 6 (2015) 6368. https://doi.org/10.1038/ncomms7368.
[11] J.B. Jones, J.V. Sanders, E.R. Segnit, Structure of Opal, Nature 204 (1964) 990–991. https://doi.org/10.1038/204990a0.
[12] C. Yang, W. Shen, Y. Zhang, K. Li, X. Fang, X. Zhang, X. Liu, Compact Multilayer Film Structure for Angle Insensitive Color Filtering, Sci Rep 5 (2015) 9285. https://doi.org/10.1038/srep09285.
[13] S. Daqiqeh Rezaei, J. Ho, A. Naderi, M. Tavakkoli Yaraki, T. Wang, Z. Dong, S. Ramakrishna, J.K.W. Yang, Tunable, Cost-Effective, and Scalable Structural Colors for Sensing and Consumer Products, Advanced Optical Materials 7 (2019) 1900735. https://doi.org/10.1002/adom.201900735.
[14] S.-W. Wang, D. Liu, B. Lin, X. Chen, Z. Li, Y. Shi, W. Wang, W. Lu, Realization of Integrated Narrow Bandpass Filters in the Infrared Region, International Journal of Infrared and Millimeter Waves 25 (2004) 1677–1683. https://doi.org/10.1023/B:IJIM.0000047457.40979.6e.
[15] S. Kinoshita, S. Yoshioka, J. Miyazaki, Physics of structural colors, Rep. Prog. Phys. 71 (2008) 076401. https://doi.org/10.1088/0034-4885/71/7/076401.
[16] J.-H. Liao, W. Wang, C.-J. Chen, C.-J. Yu, M.-C. Wu, Design and fabrication of large-area tunable MOEMS-based shortwave infrared Fabry-Pérot filters, Journal of Vacuum Science & Technology B, Nanotechnology and Microelectronics: Materials, Processing, Measurement, and Phenomena 37 (2019) 032002. https://doi.org/10.1116/1.5085259.
[17] E. Yablonovitch, Inhibited Spontaneous Emission in Solid-State Physics and Electronics, Phys.

Rev. Lett. 58 (1987) 2059–2062. https://doi.org/10.1103/PhysRevLett.58.2059.
[18] A.F. Kaplan, T. Xu, L. Jay Guo, High efficiency resonance-based spectrum filters with tunable transmission bandwidth fabricated using nanoimprint lithography, Applied Physics Letters 99 (2011) 143111. https://doi.org/10.1063/1.3647633.
[19] L. Cao, P. Fan, E.S. Barnard, A.M. Brown, M.L. Brongersma, Tuning the Color of Silicon Nanostructures, Nano Lett. 10 (2010) 2649–2654. https://doi.org/10.1021/nl1013794.
[20] N.K. Pervez, W. Cheng, Z. Jia, M.P. Cox, H.M. Edrees, I. Kymissis, Photonic crystal spectrometer, Opt. Express 18 (2010) 8277. https://doi.org/10.1364/OE.18.008277.
[21] J.G. Fleming, S.Y. Lin, I. El-Kady, R. Biswas, K.M. Ho, All-metallic three-dimensional photonic crystals with a large infrared bandgap, Nature 417 (2002) 52–55. https://doi.org/10.1038/417052a.
[22] P.V. Braun, P. Wiltzius, Electrochemically grown photonic crystals, Nature 402 (1999) 603–604. https://doi.org/10.1038/45137.
[23] D. Ge, E. Lee, L. Yang, Y. Cho, M. Li, D.S. Gianola, S. Yang, A Robust Smart Window: Reversibly Switching from High Transparency to Angle-Independent Structural Color Display, Adv. Mater. 27 (2015) 2489–2495. https://doi.org/10.1002/adma.201500281.
[24] S. Luo, Y. Li, Q. Jin, Z. Yu, H. Yu, Amorphous Arrays of Silica Nanoparticles Coated with PDMS Brushes Enable Water-Repellent Noniridescent Structural Colors for Optical Information Encryption, ACS Appl. Nano Mater. 5 (2022) 9584–9593. https://doi.org/10.1021/acsanm.2c01801.
[25] T. Endo, Y. Yanagida, T. Hatsuzawa, Colorimetric detection of volatile organic compounds using a colloidal crystal-based chemical sensor for environmental applications, Sensors and Actuators B: Chemical 125 (2007) 589–595. https://doi.org/10.1016/j.snb.2007.03.003.
[26] H. Fudouzi, T. Sawada, Photonic Rubber Sheets with Tunable Color by Elastic Deformation, Langmuir 22 (2006) 1365–1368. https://doi.org/10.1021/la0521037.
[27] X. Lai, J. Peng, Q. Cheng, A.P. Tomsia, G. Zhao, L. Liu, G. Zou, Y. Song, L. Jiang, M. Li, Bioinspired Color Switchable Photonic Crystal Silicone Elastomer Kirigami, Angew. Chem. 133 (2021) 14428–14433. https://doi.org/10.1002/ange.202103045.
[28] Y. Iwayama, J. Yamanaka, Y. Takiguchi, M. Takasaka, K. Ito, T. Shinohara, T. Sawada, M. Yonese, Optically Tunable Gelled Photonic Crystal Covering Almost the Entire Visible Light Wavelength Region, Langmuir 19 (2003) 977–980. https://doi.org/10.1021/la0207365.
[29] G.A. Williams, R. Ishige, O.R. Cromwell, J. Chung, A. Takahara, Z. Guan, Mechanically Robust and Self-Healable Superlattice Nanocomposites by Self-Assembly of Single-Component “Sticky” Polymer-Grafted Nanoparticles, Adv. Mater. 27 (2015) 3934–3941. https://doi.org/10.1002/adma.201500927.
[30] G.H. Lee, T.M. Choi, B. Kim, S.H. Han, J.M. Lee, S.-H. Kim, Chameleon-Inspired Mechanochromic Photonic Films Composed of Non-Close-Packed Colloidal Arrays, ACS Nano 11 (2017) 11350–11357. https://doi.org/10.1021/acsnano.7b05885.
[31] E. Inci, G. Topcu, M.M. Demir, Colloidal films of SiO2 in elastomeric polyacrylates by photopolymerization: A strain sensor application, Sensors and Actuators B: Chemical 305 (2020) 127452. https://doi.org/10.1016/j.snb.2019.127452.
[32] J. Zhu, L. Wan, C. Zhao, R. Sakai, Y. Mikami, T. Feng, C. Chen, W. Liu, H. Yoshioka, Z. Li, Y. Oki, Tunable and flexible deep-ultraviolet bandpass filters based on micro- and nanoparticle/polydimethylsiloxane hybrid membranes, Optical Materials 115 (2021) 111073. https://doi.org/10.1016/j.optmat.2021.111073.
[33] M. Tsuchiya, Y. Kurashina, H. Onoe, Eye-recognizable and repeatable biochemical flexible sensors using low angle-dependent photonic colloidal crystal hydrogel microbeads, Sci Rep 9 (2019) 17059. https://doi.org/10.1038/s41598-019-53499-2.
[34] H. Tan, Q. Lyu, Z. Xie, M. Li, K. Wang, K. Wang, B. Xiong, L. Zhang, J. Zhu, Metallosupramolecular Photonic Elastomers with Self-Healing Capability and Angle-Independent Color, Adv. Mater. (2018) 1805496. https://doi.org/10.1002/adma.201805496.

[35] G. Kamita, B. Frka-Petesic, A. Allard, M. Dargaud, K. King, A.G. Dumanli, S. Vignolini, Biocompatible and Sustainable Optical Strain Sensors for Large-Area Applications, Advanced Optical Materials 4 (2016) 1950–1954. https://doi.org/10.1002/adom.201600451.
[36] H. Kim, J. Choi, K.K. Kim, P. Won, S. Hong, S.H. Ko, Biomimetic chameleon soft robot with artificial crypsis and disruptive coloration skin, Nat Commun 12 (2021) 4658. https://doi.org/10.1038/s41467-021-24916-w.
[37] J.H. Lee, B. Fan, T.D. Samdin, D.A. Monteiro, M.S. Desai, O. Scheideler, H.-E. Jin, S. Kim, S.-W. Lee, Phage-Based Structural Color Sensors and Their Pattern Recognition Sensing System, ACS Nano 11 (2017) 3632–3641. https://doi.org/10.1021/acsnano.6b07942.
[38] H. Xu, M.K. Zhang, Y.F. Lu, J.J. Li, S.J. Ge, Z.Z. Gu, Dual-Mode Wearable Strain Sensor Based on Graphene/Colloidal Crystal Films for Simultaneously Detection of Subtle and Large Human Motions, Adv Materials Technologies 5 (2020) 1901056. https://doi.org/10.1002/admt.201901056.
[39] Y. Fang, W. Fei, X. Shen, J. Guo, C. Wang, Magneto-sensitive photonic crystal ink for quick printing of smart devices with structural colors, Mater. Horiz. 8 (2021) 2079–2087. https://doi.org/10.1039/D1MH00577D.
[40] S. Jung, K.I. MacConaghy, J.L. Kaar, M.P. Stoykovich, Enhanced Optical Sensitivity in Thermoresponsive Photonic Crystal Hydrogels by Operating Near the Phase Transition, ACS Appl. Mater. Interfaces 9 (2017) 27927–27935. https://doi.org/10.1021/acsami.7b07179.
[41] J. Kang, J.H. Moon, S. Lee, S. Park, S.G. Jang, S. Yang, S. Yang, Thermoresponsive Hydrogel Photonic Crystals by Three-Dimensional Holographic Lithography, Advanced Materials 20 (2008) 3061–3065. https://doi.org/10.1002/adma.200800141.
[42] J.D. Debord, L.A. Lyon, Thermoresponsive Photonic Crystals, J. Phys. Chem. B 104 (2000) 6327–6331. https://doi.org/10.1021/jp001238c.
[43] H. Jiang, Y. Zhu, C. Chen, J. Shen, H. Bao, L. Peng, X. Yang, C. Li, Photonic crystal pH and metal cation sensors based on poly(vinyl alcohol) hydrogel, New J. Chem. 36 (2012) 1051. https://doi.org/10.1039/c2nj20989f.
[44] K.W. Kimble, J.P. Walker, D.N. Finegold, S.A. Asher, Progress toward the development of a point-of-care photonic crystal ammonia sensor, Anal Bioanal Chem 385 (2006) 678–685. https://doi.org/10.1007/s00216-006-0453-y.
[45] S.A. Asher, V.L. Alexeev, A.V. Goponenko, A.C. Sharma, I.K. Lednev, C.S. Wilcox, D.N. Finegold, Photonic Crystal Carbohydrate Sensors: Low Ionic Strength Sugar Sensing, J. Am. Chem. Soc. 125 (2003) 3322–3329. https://doi.org/10.1021/ja021037h.
[46] K.I. MacConaghy, D.M. Chadly, M.P. Stoykovich, J.L. Kaar, Optically Diffracting Hydrogels for Screening Kinase Activity in Vitro and in Cell Lysate: Impact of Material and Solution Properties, Anal. Chem. 87 (2015) 3467–3475. https://doi.org/10.1021/acs.analchem.5b00442.
[47] A.K. Yetisen, H. Butt, L.R. Volpatti, I. Pavlichenko, M. Humar, S.J.J. Kwok, H. Koo, K.S. Kim, I. Naydenova, A. Khademhosseini, S.K. Hahn, S.H. Yun, Photonic hydrogel sensors, Biotechnology Advances 34 (2016) 250–271. https://doi.org/10.1016/j.biotechadv.2015.10.005.
[48] X. Wang, Y. Li, J. Zheng, X. Li, G. Liu, L. Zhou, W. Zhou, J. Shao, Polystyrene@poly(methyl methacrylate-butyl acrylate) Core–Shell Nanoparticles for Fabricating Multifunctional Photonic Crystal Films as Mechanochromic and Solvatochromic Sensors, ACS Appl. Nano Mater. 5 (2022) 729–736. https://doi.org/10.1021/acsanm.1c03474.
[49] K. Ueno, A. Inaba, Y. Sano, M. Kondoh, M. Watanabe, A soft glassy colloidal array in ionic liquid, which exhibits homogeneous, non-brilliant and angle-independent structural colours, Chem. Commun. (2009) 3603. https://doi.org/10.1039/b905108b.
[50] Y. Takeoka, M. Honda, T. Seki, M. Ishii, H. Nakamura, Structural Colored Liquid Membrane without Angle Dependence, ACS Appl. Mater. Interfaces 1 (2009) 982–986. https://doi.org/10.1021/am900074v.
[51] Y. Takeoka, Angle-independent structural coloured amorphous arrays, J. Mater. Chem. 22 (2012)

23299–23309. https://doi.org/10.1039/C2JM33643J.
[52] K. Vynck, R. Pierrat, R. Carminati, L.S. Froufe-Pérez, F. Scheffold, R. Sapienza, S. Vignolini, J.J. Sáenz, Light in correlated disordered media, Rev. Mod. Phys. 95 (2023) 045003. https://doi.org/10.1103/RevModPhys.95.045003.
[53] Matsuyama T., Derivation of Mie Theory of Light Scattering, J. Soc. Powder Technolo, Japan 43 (2006) 115–124. https://doi.org/10.4164/sptj.43.115.
[54] N. Li, Y. Zhu, Z. Wang, A Discussion on the Applicable Condition of Rayleigh Scattering, International Journal of Remote Sensing Applications 5 (2015) 62. https://doi.org/10.14355/ijrsa.2015.05.007.
[55] A. Müller, M.C. Wapler, U. Wallrabe, A quick and accurate method to determine the Poisson's ratio and the coefficient of thermal expansion of PDMS, Soft Matter 15 (2019) 779–784. https://doi.org/10.1039/C8SM02105H.
[56] J.H. Kim, J.B. Kim, Y.H. Choi, S. Park, S. Kim, Photonic Microbeads Templated by Oil-in-Oil Emulsion Droplets for High Saturation of Structural Colors, Small 18 (2022) 2105225. https://doi.org/10.1002/smll.202105225.
[57] J.H. Kim, K.H. Kim, G.H. Lee, J.-W. Kim, S.H. Han, C.-S. Lee, S.-H. Kim, Microfluidic Production of Mechanochromic Photonic Fibers Containing Nonclose-Packed Colloidal Arrays, Small Science 1 (2021) 2000058. https://doi.org/10.1002/smsc.202000058.
[58] T. Rouxel, Elastic Properties and Short-to Medium-Range Order in Glasses, Journal of the American Ceramic Society 90 (2007) 3019–3039. https://doi.org/10.1111/j.1551-2916.2007.01945.x.
[59] L.D. Mello, L.T. Kubota, Review of the use of biosensors as analytical tools in the food and drink industries, Food Chemistry 77 (2002) 237–256. https://doi.org/10.1016/S0308-8146(02)00104-8.
[60] M. Gholizadeh, A. Melesse, L. Reddi, A Comprehensive Review on Water Quality Parameters Estimation Using Remote Sensing Techniques, Sensors 16 (2016) 1298. https://doi.org/10.3390/s16081298.
[61] D. Wu, D.-W. Sun, Colour measurements by computer vision for food quality control – A review, Trends in Food Science & Technology 29 (2013) 5–20. https://doi.org/10.1016/j.tifs.2012.08.004.
[62] J. Claßen, F. Aupert, K.F. Reardon, D. Solle, T. Scheper, Spectroscopic sensors for in-line bioprocess monitoring in research and pharmaceutical industrial application, Anal Bioanal Chem 409 (2017) 651–666. https://doi.org/10.1007/s00216-016-0068-x.
[63] J. Toledo, V. Ruiz-Díez, G. Pfusterschmied, U. Schmid, J.L. Sánchez-Rojas, Flow-through sensor based on piezoelectric MEMS resonator for the in-line monitoring of wine fermentation, Sensors and Actuators B: Chemical 254 (2018) 291–298. https://doi.org/10.1016/j.snb.2017.07.096.
[64] T.S. Awad, H.A. Moharram, O.E. Shaltout, D. Asker, M.M. Youssef, Applications of ultrasound in analysis, processing and quality control of food: A review, Food Research International 48 (2012) 410–427. https://doi.org/10.1016/j.foodres.2012.05.004.
[65] S.R. Wylie, A. Shaw, A.I. Al-Shamma'a, RF sensor for multiphase flow measurement through an oil pipeline, Meas. Sci. Technol. 17 (2006) 2141–2149. https://doi.org/10.1088/0957-0233/17/8/013.
[66] P. Yeh, N. Yeh, C.-H. Lee, T.-J. Ding, Applications of LEDs in optical sensors and chemical sensing device for detection of biochemicals, heavy metals, and environmental nutrients, Renewable and Sustainable Energy Reviews 75 (2017) 461–468. https://doi.org/10.1016/j.rser.2016.11.011.
[67] Z. Ding, D. Zhang, G. Wang, M. Tang, Y. Dong, Y. Zhang, H. Ho, X. Zhang, An in-line spectrophotometer on a centrifugal microfluidic platform for real-time protein determination and calibration, Lab Chip 16 (2016) 3604–3614. https://doi.org/10.1039/C6LC00542J.
[68] M.K. Sharma, R. Gostl, A.J.H. Frijns, F.P. Wieringa, J.P. Kooman, R.P. Sijbesma, D.M.J. Smeulders, A Fluorescent Micro-Optofluidic Sensor for In-Line Ion Selective Electrolyte Monitoring, IEEE Sensors J. 18 (2018) 3946–3951. https://doi.org/10.1109/JSEN.2018.2816986.
[69] J.J. Creelman, E.A. Luy, G.C.H. Beland, C. Sonnichsen, V.J. Sieben, Simultaneous Absorbance and Fluorescence Measurements Using an Inlaid Microfluidic Approach, Sensors 21 (2021) 6250.

https://doi.org/10.3390/s21186250.
[70] X. Hu, Y. Zhao, Y. Peng, R. Tong, H. Zheng, J. Zhao, S. Hu, In-fiber optofluidic michelson interferometer for detecting small volume and low concentration chemicals with a fiber ring cavity laser, Sensors and Actuators B: Chemical 370 (2022) 132467. https://doi.org/10.1016/j.snb.2022.132467.
[71] A. Koh, D. Kang, Y. Xue, S. Lee, R.M. Pielak, J. Kim, T. Hwang, S. Min, A. Banks, P. Bastien, M.C. Manco, L. Wang, K.R. Ammann, K.-I. Jang, P. Won, S. Han, R. Ghaffari, U. Paik, M.J. Slepian, G. Balooch, Y. Huang, J.A. Rogers, A soft, wearable microfluidic device for the capture, storage, and colorimetric sensing of sweat, Sci. Transl. Med. 8 (2016). https://doi.org/10.1126/scitranslmed.aaf2593.
[72] C. Zhang, D.P. Bailey, K.S. Suslick, Colorimetric Sensor Arrays for the Analysis of Beers: A Feasibility Study, J. Agric. Food Chem. 54 (2006) 4925–4931. https://doi.org/10.1021/jf060110a.
[73] Z. Yang, T. Albrow-Owen, W. Cai, T. Hasan, Miniaturization of optical spectrometers, Science 371 (2021) eabe0722. https://doi.org/10.1126/science.abe0722.
[74] D.C.J. Neo, M.M.X. Ong, Y.Y. Lee, E.J. Teo, Q. Ong, H. Tanoto, J. Xu, K.S. Ong, V. Suresh, Shaping and Tuning Lighting Conditions in Controlled Environment Agriculture: A Review, ACS Agric. Sci. Technol. 2 (2022) 3–16. https://doi.org/10.1021/acsagscitech.1c00241.
[75] X. Xu, S. Smith, J. Urban, Z. Cui, An in line non-invasive optical system to monitor pH in cell and tissue culture, Medical Engineering & Physics 28 (2006) 468–474. https://doi.org/10.1016/j.medengphy.2005.07.016.
[76] E. Dervisevic, N.H. Voelcker, G. Risbridger, K.L. Tuck, V.J. Cadarso, High-Aspect-Ratio SU-8-Based Optofluidic Device for Ammonia Detection in Cell Culture Media, ACS Sens. 5 (2020) 2523–2529. https://doi.org/10.1021/acssensors.0c00821.
[77] S.M.S.U. Eskander, S. Fankhauser, Reduction in greenhouse gas emissions from national climate legislation, Nat. Clim. Chang. 10 (2020) 750–756. https://doi.org/10.1038/s41558-020-0831-z.
[78] M. Jafari, A. Botterud, A. Sakti, Decarbonizing power systems: A critical review of the role of energy storage, Renewable and Sustainable Energy Reviews 158 (2022) 112077. https://doi.org/10.1016/j.rser.2022.112077.
[79] O. Toprakci, H.A.K. Toprakci, L. Ji, X. Zhang, Fabrication and Electrochemical Characteristics of $LiFePO_4$ Powders for Lithium-Ion Batteries, KONA 28 (2010) 50–73. https://doi.org/10.14356/kona.2010008.
[80] P. Yao, H. Yu, Z. Ding, Y. Liu, J. Lu, M. Lavorgna, J. Wu, X. Liu, Review on Polymer-Based Composite Electrolytes for Lithium Batteries, Front. Chem. 7 (2019) 522. https://doi.org/10.3389/fchem.2019.00522.
[81] C. Hendricks, N. Williard, S. Mathew, M. Pecht, A failure modes, mechanisms, and effects analysis (FMMEA) of lithium-ion batteries, Journal of Power Sources 297 (2015) 113–120. https://doi.org/10.1016/j.jpowsour.2015.07.100.
[82] Z. Chen, X. Wu, B. Li, X. Lin, R. Xiao, G. Feng, Y. Wang, A novel voltage protection method for multi-cell lithium-ion battery protection IC, J. Phys.: Conf. Ser. 2313 (2022) 012014. https://doi.org/10.1088/1742-6596/2313/1/012014.
[83] C. Zheng, Z. Chen, D. Huang, Fault diagnosis of voltage sensor and current sensor for lithium-ion battery pack using hybrid system modeling and unscented particle filter, Energy 191 (2020) 116504. https://doi.org/10.1016/j.energy.2019.116504.
[84] Z. Wei, J. Zhao, H. He, G. Ding, H. Cui, L. Liu, Future smart battery and management: Advanced sensing from external to embedded multi-dimensional measurement, Journal of Power Sources 489 (2021) 229462. https://doi.org/10.1016/j.jpowsour.2021.229462.
[85] B. Sun, G. Xu, X. Ji, Z. Yang, C. Guan, S. Chen, X. Chen, Y. Ma, Y. Yu, J. Feng, A strain-resistant flexible thermistor sensor array based on CNT/MXene hybrid materials for lithium-ion battery and human temperature monitoring, Sensors and Actuators A: Physical 368 (2024) 115059. https://doi.org/10.1016/j.sna.2024.115059.
[86] Z. Wei, J. Hu, H. He, Y. Yu, J. Marco, Embedded Distributed Temperature Sensing Enabled

Multistate Joint Observation of Smart Lithium-Ion Battery, IEEE Trans. Ind. Electron. 70 (2023) 555–565. https://doi.org/10.1109/TIE.2022.3146503.
[87] J.H. Lee, H.M. Lee, S. Ahn, Battery dimensional changes occurring during charge/discharge cycles—thin rectangular lithium ion and polymer cells, Journal of Power Sources 119–121 (2003) 833–837. https://doi.org/10.1016/S0378-7753(03)00281-7.
[88] Y. Zhao, F.B. Spingler, Y. Patel, G.J. Offer, A. Jossen, Localized Swelling Inhomogeneity Detection in Lithium Ion Cells Using Multi-Dimensional Laser Scanning, J. Electrochem. Soc. 166 (2019) A27–A34. https://doi.org/10.1149/2.0011902jes.
[89] J.B. Siegel, A.G. Stefanopoulou, P. Hagans, Y. Ding, D. Gorsich, Expansion of Lithium Ion Pouch Cell Batteries: Observations from Neutron Imaging, J. Electrochem. Soc. 160 (2013) A1031–A1038. https://doi.org/10.1149/2.011308jes.
[90] A. Raghavan, P. Kiesel, L.W. Sommer, J. Schwartz, A. Lochbaum, A. Hegyi, A. Schuh, K. Arakaki, B. Saha, A. Ganguli, K.H. Kim, C. Kim, H.J. Hah, S. Kim, G.-O. Hwang, G.-C. Chung, B. Choi, M. Alamgir, Embedded fiber-optic sensing for accurate internal monitoring of cell state in advanced battery management systems part 1: Cell embedding method and performance, Journal of Power Sources 341 (2017) 466–473. https://doi.org/10.1016/j.jpowsour.2016.11.104.
[91] W. Wu, X. Xiao, X. Huang, S. Yan, A multiphysics model for the in situ stress analysis of the separator in a lithium-ion battery cell, Computational Materials Science 83 (2014) 127–136. https://doi.org/10.1016/j.commatsci.2013.10.002.
[92] X. Xu, S. Wang, H. Wang, C. Hu, Y. Jin, J. Liu, H. Yan, Recent progresses in the suppression method based on the growth mechanism of lithium dendrite, Journal of Energy Chemistry 27 (2018) 513–527. https://doi.org/10.1016/j.jechem.2017.11.010.
[93] M. Dollé, L. Sannier, B. Beaudoin, M. Trentin, J.-M. Tarascon, Live Scanning Electron Microscope Observations of Dendritic Growth in Lithium/Polymer Cells, Electrochem. Solid-State Lett. 5 (2002) A286. https://doi.org/10.1149/1.1519970.
[94] C. Niu, M. Zhang, G. Chen, B. Cao, J. Shi, J. Du, Y. Chen, An effectively inhibiting lithium dendrite growth in-situ-polymerized gel polymer electrolyte, Electrochimica Acta 283 (2018) 349–356. https://doi.org/10.1016/j.electacta.2018.06.169.
[95] J. Self, C.P. Aiken, R. Petibon, J.R. Dahn, Survey of Gas Expansion in Li-Ion NMC Pouch Cells, J. Electrochem. Soc. 162 (2015) A796–A802. https://doi.org/10.1149/2.0081506jes.
[96] C. Niu, J. Liu, G. Chen, C. Liu, T. Qian, J. Zhang, B. Cao, W. Shang, Y. Chen, J. Han, J. Du, Y. Chen, Anion-regulated solid polymer electrolyte enhances the stable deposition of lithium ion for lithium metal batteries, Journal of Power Sources 417 (2019) 70–75. https://doi.org/10.1016/j.jpowsour.2019.02.004.
[97] Q. Lyu, S. Wang, B. Peng, X. Chen, S. Du, M. Li, L. Zhang, J. Zhu, Bioinspired Photonic Ionogels as Interactively Visual Ionic Skin with Optical and Electrical Synergy, Small 17 (2021) 2103271. https://doi.org/10.1002/smll.202103271.
[98] H. Goto, S. Nishita, H. Takahashi, H. Onoe, Core-shell Structural Color Voxels with Controllable Elasticity for Acoustically Levitated Displays, in: Montreal, μTAS 2024, 2024.

Appendix A License permissions

Figure number	License permissions/numbers
Figure 1.1	(a) 5947540058312 (b) 5947540321855 (c) Reprinted with permission from NANO Letters. Copyright 2010 American Chemical Society. (d) Open access (©2010 Optical Society of America) (e) Reprinted with permission from Langmuir. Copyright 2006 American Chemical Society.
Figure 1.2	(a) 5947560276115 (b) 5947560448317 (c) Reprinted (adapted) with permission from ACS Nano. Copyright 2017 American Chemical Society. (d) Open access (© 2016 The Authors. Published by WILEY-VCH Verlag GmbH & Co. KGaA, Weinheim) (e) Reprinted with permission from Langmuir. Copyright 2003 American Chemical Society.
Figure 1.3	(a) 5947611037456 (b) 1566543-1 (c) Reprinted with permission from Applied Materials. Copyright 2017 American Chemical Society. (d) 1566555-1 (e) Reprinted (adapted) with permission from Journal of the American Chemical Society. Copyright 2003 American Chemical Society.
Figure 2.3	(a)-(b) RNP/25/JAN/087208
Figure 2.4	(a)-(b) Reprinted (adapted) with permission from ACS Nano. Copyright 2017 American Chemical Society.

Figure B.1	RNP/25/JAN/087208

Appendix B Theory of Light Scattering

In this section, theory of light scattering is explained [52]. The wave equation of the electric field **E** in a vacuum is expressed as

$$\nabla \times \nabla \times \mathbf{E}(\mathbf{r}) - k_0^2 \mathbf{E}(\mathbf{r}) = 0 \tag{B. 1}$$

where **r** denotes the position vector in space and $k_0 = \omega/c$ (ω: frequency, c: light speed). In contrast, the wave equation in a nonmagnetic and isotropic material is expressed as

$$\nabla \times \nabla \times \mathbf{E}(\mathbf{r}) - k_0^2 \epsilon_\mathrm{h} \mathbf{E}(\mathbf{r}) = \frac{k_0^2 \mathbf{P}(\mathbf{r})}{\epsilon_0} \tag{B. 2}$$

where ε_h denotes relative permittivity of a uniform host medium, **P**(**r**) is the polarization density expressed as $\mathbf{P}(\mathbf{r}) = \varepsilon_0[\varepsilon(\mathbf{r}) - \varepsilon_\mathrm{h}]\mathbf{E}(\mathbf{r})$, and ε_0 is a permittivity in a vacuum. To solve this equation, the electromagnetic Green's tensor $\mathbf{G}_\mathrm{b}(\mathbf{r}, \mathbf{r'})$ expressed as

$$\nabla \times \nabla \times \mathbf{G}_\mathrm{b}(\mathbf{r}, \mathbf{r}') - k_b^2 \mathbf{G}_\mathrm{b}(\mathbf{r}, \mathbf{r}') = \delta(\mathbf{r} - \mathbf{r}')\mathbf{1} \tag{B. 3}$$

is used. Here, δ is delta function and **1** is the unit tensor. Then, (B. 2) is rewritten as

$$\mathbf{E}(\mathbf{r}) = \mathbf{E}_\mathrm{b}(\mathbf{r}) + \int \mathbf{G}_\mathrm{b}(\boldsymbol{r}, \boldsymbol{r}')\mathbf{X}(\mathbf{r}')\mathbf{E}(\mathbf{r}')d\mathbf{r}' \tag{B. 4}$$

$$\mathbf{X}(\mathbf{r}) = k_0^2[\epsilon(\boldsymbol{r}) - \epsilon_b]\mathbf{1} \tag{B. 5}$$

where **X** is called an effective scattering potential. Here, ε_b is a constant background permittivity that can differ from ε_h. Equation (B. 4) is known as the Lippmann-Schwinger equation. Equation (B. 4) is rewritten with an integral operator $\boldsymbol{\mathcal{G}}_\mathrm{b}$,

$$\mathbf{E} = \mathbf{E}_\mathrm{b} + \boldsymbol{\mathcal{G}}_\mathrm{b}\mathbf{X}\mathbf{E}. \tag{B. 6}$$

When statistical average of Equation (B. 6) is applied, the equation known as the Dyson equation expressed as

$$\langle \mathbf{E} \rangle = \mathbf{E}_\mathrm{b} + \boldsymbol{\mathcal{G}}_\mathrm{b}\boldsymbol{\Sigma}\langle \mathbf{E} \rangle \tag{B. 7}$$

$$\boldsymbol{\Sigma} = \langle \mathbf{T} \rangle [\mathbf{1} + \boldsymbol{\mathcal{G}}_\mathrm{b}\langle \mathbf{T} \rangle]^{-1} \tag{B. 8}$$

$$\mathbf{T} = [\mathbf{1} + \mathbf{X}\boldsymbol{\mathcal{G}}_\mathrm{b}]^{-1}\mathbf{X} \tag{B. 9}$$

where $\langle \ldots \rangle$ means average, $\boldsymbol{\Sigma}$ is called the self-energy operator, and **T** is called the transition operator. The disordered medium has fluctuating permittivity around the background

permittivity ε_b under the scattering potential **X**. The scattering light is propagated in the disordered medium, following Equation (B. 7).

The correlation function of the electric field **C**(**r**, **r'**) is expressed as

$$\mathbf{C}(\mathbf{r},\mathbf{r}') = \langle \mathbf{E}(\mathbf{r})\rangle \otimes \langle \mathbf{E}^*(\mathbf{r})\rangle + \int \langle \mathbf{G}(\mathbf{r},\mathbf{r_1})\rangle \otimes \langle \mathbf{G}^*(\mathbf{r}',\mathbf{r_1'})\rangle \cdot \mathbf{\Gamma}(\mathbf{r_1},\mathbf{r_2},\mathbf{r_1'},\mathbf{r_2'}) \cdot \mathbf{C}(\mathbf{r_2},\mathbf{r_2'}) d\mathbf{r_1} d\mathbf{r_1'} d\mathbf{r_2} d\mathbf{r_2'} \quad \text{(B. 10)}$$

where the asterisk denotes the complex conjugate and the dot means tensor contraction. **Γ** is known as the four-point irreducible vertex (intensity vertex). This equation can be approximated on a large scale, expressed as

$$\left[\mathbf{u}\cdot\nabla_{\mathbf{r}} + \frac{1}{l_e}\right] I(\mathbf{r},\mathbf{u}) = \frac{1}{l_s}\int p(\mathbf{u},\mathbf{u}') I(\mathbf{r},\mathbf{u}') d\mathbf{u}' \quad \text{(B. 11)}$$

where **r** is position, **u** is direction, l_e is the extinction mean free path, l_s is the scattering mean free path, I is the specific intensity, and p is the phase function. This equation is known as the radiative transfer equation (RTE). In non-absorbing dielectric materials, it is known that the extinction is driven only by scattering ($l_e = l_s$). With the intensity vertex, l_s and p have a relation expressed as

$$\frac{1}{l_s} p(\mathbf{u},\mathbf{u}') = \frac{1}{32\pi^2}\mathrm{Tr}[\mathbf{P}(\mathbf{u})\otimes\mathbf{P}(\mathbf{u})\cdot\bar{\mathbf{\Gamma}}(k_r\mathbf{u},k_r\mathbf{u}',k_r\mathbf{u},k_r\mathbf{u}')\cdot\mathbf{P}(\mathbf{u}')\otimes\mathbf{P}(\mathbf{u}')\cdot\mathbf{1}] \quad \text{(B. 12)}$$

$$\int p(\mathbf{u},\mathbf{u}')d\mathbf{u}' = 1 \quad \text{(B. 13)}$$

$$\mathbf{P}(\mathbf{u}) = \mathbf{1} - \mathbf{u}\otimes\mathbf{u} \quad \text{(B.14)}$$

where $\bar{\mathbf{\Gamma}}$ is the average of intensity vertex, and k_r is defined as $k_r = k_0\ \mathrm{Re}[n_{eff}]$ with the effective refractive index n_{eff} in a homogeneous medium. Tr() in Equation (B.12) is the trace of the tensor. Equation (B. 13) means that the probability of the scattering angle is equal to 1. Equation (40) means the assumption of a depolarized field. The RTE (Equation (B.11) means an energy balance of the light in a local space.

Moreover, the RTE can be simplified to a diffusion equation in the deep multiple

scattering regime as follows:

$$\int [\mathbf{u} \cdot \nabla_{\mathbf{r}} I(\mathbf{r}, \mathbf{u})] \mathbf{u} d\mathbf{u} + \frac{1}{l_t} \mathbf{j}(\mathbf{r}) = 0 \quad \text{(B. 15)}$$

$$\mathbf{j}(\mathbf{r}) = \int I(\mathbf{r}, \mathbf{u}) \mathbf{u} d\mathbf{u} \quad \text{(B. 16)}$$

$$l_t = \frac{l_s}{1 - g} \quad \text{(B. 17)}$$

$$g = \int p(\mathbf{u}, \mathbf{u}') \mathbf{u} \cdot \mathbf{u}' d\mathbf{u}. \quad \text{(B. 18)}$$

Here, l_t denotes the transport mean free path, $\mathbf{j}(\mathbf{r})$ denotes the radiative flux vector, and g is the average cosine of the scattering angle. Equation (B.15) describes a diffusion equation. The structural correlation expressed by l_t affects l_s and g. The scattering anisotropy is described by g.

To rewrite Equation (B.12), the static structure factor $S(\mathbf{k})$ is introduced that is defined as

$$S(\mathbf{k}) \equiv 1 + \rho h_2(\mathbf{k}) \quad \text{(B. 19)}$$

$$h_2(\mathbf{r}) \equiv g_2(\mathbf{r}) - 1 \quad \text{(B. 20)}$$

$$g_2(\mathbf{r}_1, \mathbf{r}_2) = \frac{1}{\rho^2} \rho_2(\mathbf{r}_1, \mathbf{r}_2) \quad \text{(B. 21)}$$

$$\rho_2(\mathbf{r}_1, \mathbf{r}_2) = \langle \sum_{j_1 \neq j_2} \delta(\mathbf{r}_1 - \mathbf{R}_{j_1}) \delta(\mathbf{r}_2 - \mathbf{R}_{j_2}) \rangle. \quad \text{(B. 22)}$$

Here, h_2 is the total pair-correlation function, g_2 is the 2-particle correlation function, ρ_2 is the 2-particle probability density function, and ρ is the constant particle number density. $\mathbf{R} = [\mathbf{R}_1, \mathbf{R}_2, \ldots \mathbf{R}_N]$ is the center position of the particles.

In addition, the form factor is also introduced that is defined as

$$F(q) \equiv k_r^2 \frac{d\sigma}{d\Omega}(q) \quad \text{(B. 23)}$$

$$q = k_r |\mathbf{u} - \mathbf{u}'| \quad \text{(B. 24)}$$

$$\frac{d\sigma}{d\Omega}(k) = k_h^4 \frac{\alpha_p^2}{(4\pi)^2} P(k) \quad \text{(B. 25)}$$

$$P(k) = 1 - 2k^2 + 2k^4. \quad \text{(B. 26)}$$

where k_h is the wave number of the host medium and α_p is the particle polarizability. Equation (B.21) is called the Rayleigh differential scattering cross section.

Eventually, l_s and l_t described in Equation (B.12) and (B.15) are rewritten as

$$\frac{1}{l_s} = \frac{2\pi\rho}{k_r^4}\int_0^{2k_r} F(q)S(q)qdq \quad \text{(B. 27)}$$

$$\frac{1}{l_t} = \frac{\pi\rho}{k_r^6}\int_0^{2k_r} F(q)S(q)q^3dq. \quad \text{(B. 28)}$$

These two equations are widely used to express light scattering and transport in the correlated and disordered media. The graph shapes of $S(q) - qa$ were shown in Fig. 2.3 (a) where a means radius in a spherical region.

The structure of correlated disordered media can be expressed in another way. In a window Ω whose volume is V, the number N of dots (or particles) are distributed. When the window is spherical with radius R, the variance of N is expressed as

$$\frac{\langle N^2(R)\rangle - \langle N(R)\rangle^2}{\langle N(R)\rangle} = 1 + \rho\int h_2(\mathbf{r})\Lambda(\mathbf{r},R)d\mathbf{r} \quad \text{(B. 29)}$$

$$\Lambda(\mathbf{r},R) = \frac{v_2^{int}(\mathbf{r},R)}{V} \quad \text{(B. 30)}$$

where (B. 30) means that the two-window intersection volume v_2^{int} is divided by the window volume $V = (4/3)\pi r^3$ for normalization. Equation (B. 29) is rewritten with the limit of R,

$$\lim_{R\to\infty}\frac{\langle N^2(R)\rangle - \langle N(R)\rangle^2}{\langle N(R)\rangle} = \lim_{|\mathbf{q}|\to\infty} S(\mathbf{q}) = 1 + \rho\int h_2(\mathbf{r})d\mathbf{r} \quad \text{(B. 31)}$$

is shown. This Equation (B. 31) describes the spatial fluctuations of the particles (Fig. B.1). When $\rho\int h_2(\mathbf{r})d\mathbf{r} < 0$, the particles have negative correlation (repulsion). In contrast, the particles have positive correlation (attraction) when $\rho\int h_2(\mathbf{r})d\mathbf{r} > 0$. If $\rho\int h_2(\mathbf{r})d\mathbf{r} = 0$, the particles have uncorrelated structure.

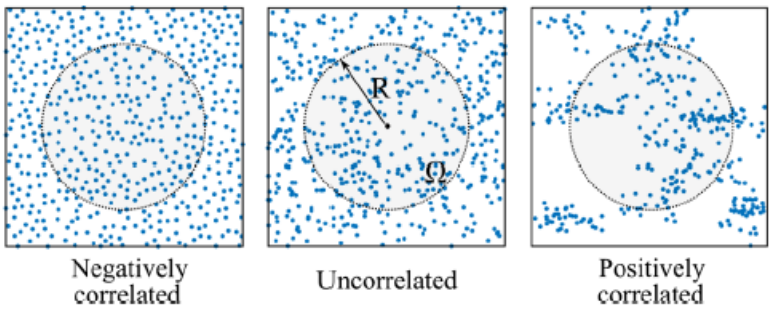

Figure B.1 Illustration of the fluctuation and correlation with three conditions [52].

Appendix C　Three-point method

The add-in for the three-point method to measure the circle diameter is shown as follows:

```
// 必要な変数の初期化
var circleData = [];  // 測定した円のデータを格納
var scaleUnit = ''; // スケールの単位（設定されていれば使用）
var scaleFactor = 1.0;  // ピクセル → 実寸変換用スケール係数
var imp = IJ.getImage();  // 現在開いている画像を取得

// 画像が開かれているかを確認
if (imp == null) {
    IJ.showMessage("Error", "No image is opened");
} else {
    var cal = imp.getCalibration();
    scaleUnit = cal.getUnit();
    scaleFactor = cal.pixelWidth;  // X と Y が同じ前提（通常の画像では OK）
    run();
}

function run() {
    IJ.showMessage("Choose 3 points");

    imp.setOverlay(null); // 既存の Overlay を削除して初期化

    // ResultsTable を作成
    var rt = new ResultsTable();
    rt.reset(); //初期化

    // ヘッダーの追加（列名）
    rt.setHeading(0, "No.");
    rt.setHeading(1, "Center X");
    rt.setHeading(2, "Center Y");
    rt.setHeading(3, "Radius(" + scaleUnit +")");
    rt.setHeading(4, "Diameter(" + scaleUnit +")");

    // 円の測定を開始
    var continueMeasurement = true;
    var data_num = 1;
    while (continueMeasurement) {
        IJ.wait(50); // 少し待機してから再度確認
        IJ.run("Select None");

        // 3 点の座標を選択
        var points = selectThreePoints();

        // 3 点選択後、円の計算
        var circleInfo = calculateCircle(points);
```

```
            // 円の情報をログに表示
            rt.incrementCounter(); // 新しい行を追加
            rt.addValue("No.", data_num);
            rt.addValue("Center X", circleInfo.centerX.toFixed(4));
            rt.addValue("Center Y", circleInfo.centerY.toFixed(4));
            rt.addValue("Radius(" + scaleUnit +")", (circleInfo.radius * scaleFactor).toFixed(4));
            rt.addValue("Diameter(" + scaleUnit +")", (circleInfo.diameter * scaleFactor).toFixed(4));
            rt.show("Result");

            // 測定データを格納
            circleData.push(circleInfo);

            // 次の測定を行うことを確認する
            var gd = new GenericDialog("Confirmation");
            gd.addMessage("Are you ready to next measurement?");
            gd.showDialog();
            if (gd.wasCanceled()) {
                continueMeasurement = false;
            }
            data_num = data_num + 1;
        }

        // 測定結果の平均と分散を計算
        var statisticInfo = calculateStats(circleData);
        rt.incrementCounter(); // 新しい行を追加
        rt.addValue("No.", "Ave.");
        rt.addValue("Center X", null);
        rt.addValue("Center Y", null);
        rt.addValue("Radius(" + scaleUnit +")", (statisticInfo.meanR * scaleFactor).toFixed(4));
        rt.addValue("Diameter(" + scaleUnit +")", (statisticInfo.meanD * scaleFactor).toFixed(4));
        rt.incrementCounter(); // 新しい行を追加
        rt.addValue("No.", "S.D.");
        rt.addValue("Center X", null);
        rt.addValue("Center Y", null);
        rt.addValue("Radius(" + scaleUnit +")", (statisticInfo.varianceR * scaleFactor).toFixed(4));
        rt.addValue("Diameter(" + scaleUnit +")", (statisticInfo.varianceD * scaleFactor).toFixed(4));
        rt.show("Result");

        return;
}

// 画像のスケール単位を取得する関数
function getScaleUnit() {
        var cal = imp.getCalibration();
        return cal.getUnit();
}

// 3 点を選択する関数
function selectThreePoints() {
        var pointslist = [];
        while (pointslist.length < 3) {       //3 点とるまで
            var roi = imp.getRoi();   // 現在の ROI を取得 (選択された点)
            if (roi != null && roi.getType() == Roi.POINT) {       //multi-point tool チェック
                pointslist = roi.getContainedPoints();   // 点のリストを取得
            }
            IJ.wait(50); // 少し待機してから再度確認
```

```
        }
        return pointslist;
}

// 3 点を通る円の情報を計算する関数
function calculateCircle(points) {
    var p1 = [points[0].x, points[0].y];
    var p2 = [points[1].x, points[1].y];
    var p3 = [points[2].x, points[2].y];

    // 円の中心と半径を計算
    var a = p2[0] - p1[0];
    var b = p2[1] - p1[1];
    var c = p3[0] - p1[0];
    var d = p3[1] - p1[1];

    var e = a * (p1[0] + p2[0]) + b * (p1[1] + p2[1]);
    var f = c * (p1[0] + p3[0]) + d * (p1[1] + p3[1]);

    var g = 2.0 * (a * (p3[1] - p2[1]) - b * (p3[0] - p2[0]));

    if (g === 0) {
        return {centerX: 0, centerY: 0, radius: -1, diameter: -1};
    }

    var centerX = (d * e - b * f) / g;
    var centerY = (a * f - c * e) / g;
    var radius = Math.sqrt(Math.pow((p1[0] - centerX), 2) + Math.pow((p1[1] - centerY), 2));
    var diameter = radius * 2;


    // 円の描画（Overlay に追加）
    var overlay = imp.getOverlay();
    if (overlay == null) {
        overlay = new Overlay();
    }
    var oval = new OvalRoi(centerX - radius, centerY - radius, radius * 2, radius * 2);
    oval.setStrokeColor(java.awt.Color.RED); // 色は好みで変更可
    overlay.add(oval);
    imp.setOverlay(overlay);


    return {centerX: centerX, centerY: centerY, radius: radius, diameter: diameter};
}

// 測定結果の統計（平均と分散）を計算する関数
function calculateStats(data) {
    var n = data.length;
    var sumR = 0, sumD = 0;

    for (var i = 0; i < n; i++) {
        sumR += data[i].radius;
        sumD += data[i].diameter;
    }

    var meanR = sumR / n;
    var meanD = sumD / n;
```

```
    var varianceR = 0, varianceD = 0;

    for (var i = 0; i < n; i++) {
        varianceR += Math.pow(data[i].radius - meanR, 2);
        varianceD += Math.pow(data[i].diameter - meanD, 2);
    }

    varianceR /= n;
    varianceD /= n;

    return {meanR: meanR, meanD: meanD, varianceR: varianceR, varianceD: varianceD};
}
```